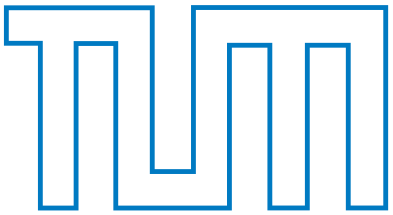

Technische Universität München

Physic Department

Chair of Physics of Synthetic Biological Systems - E14

Characterization and Application of Membrane Spanning Synthetic and Biological Nanopores

Vera Arnaut

Vollständiger Abdruck der von der Fakultät für Physik der Technischen Universität München zur Erlangung des akademischen Grades eines
Doktors der Naturwissenschaften (Dr. rer. nat.) genehmigten Dissertation.

Vorsitzender: Univ.-Prof. Dr. Ulrich Gerland

Prüfer der Dissertation:
Univ.-Prof. Dr. Friedrich C. Simmel
Univ.-Prof. Dr. Hendrik Dietz

Die Dissertation wurde am 25.07.2017 bei der Technischen Universität München eingereicht und durch die Fakultät für Physik am 20.09.2017 angenommen.

Publications

Some ideas and figures have appeared previously in the following publications:

Quantitative analysis of the nanopore translocation dynamics of simple structured polynucleotides. S. Schink, S. Renner, K. Alim, V. Arnaut, F. C. Simmel, and U. Gerland. *Biophys J, 102(1):85-95, Jan 2012.*

Synthetic lipid membrane channels formed by designed DNA nanostructures. M. Langecker, V. Arnaut, T. G. Martin, J. List, S. Renner, M. Mayer, H. Dietz, and F. C. Simmel. *Science, 338(6109):932-6, Nov 2012.*

Nanopore force spectroscopy of aptamer-ligand complexes. V. Arnaut, M. Langecker, and F. C. Simmel. *Biophys J, 105(5):1199-207, Sep 2013.*

DNA nanostructures interacting with lipid bilayer membranes. M. Langecker, V. Arnaut, J. List, and F. C. Simmel. *Acc Chem Res, 47(6):1807-15, Jun 2014.*

Molecular transport through large diameter DNA nanopores. S. Krishnan, D. Ziegler, V. Arnaut, T. G. Martin, K. Kapsner, K. Henneberg, A. R. Bausch, H. Dietz, and F. C. Simmel. *Nat Commun, 7:12787, Sep 2016.*

Contents

List of Figures

List of Tables

Abstract

Nanopores have evolved into powerful devices for the characterization of DNA conformation at the single molecule level. Nanopores spontaneously incorporate into a lipid membrane, which separates two compartments filled with aqueous solution. Electrodes placed on each side of the membrane can be used to generate an ion current through the incorporated nanopore. When a DNA molecule is driven through a nanopore by an externally applied electric field, it causes a characteristic temporary change in the trans-pore current. In particular, nanopore force spectroscopy is a versatile tool for the investigation of single molecule interactions with high throughput, sensitivity and accuracy. Nanopore force spectroscopy (NFS) experiments allow determination of the dissociation constant of molecular complexes and their voltage-dependent unbinding or unfolding rates. In our experiments, we apply the NFS technique to aptamers, which are short single-stranded nucleic acids that can adopt a conformation in which they can bind to a molecule with high specificity and affinity. Specifically, we study binding of the ATP and thrombin aptamers to their target molecules in terms of complex stability as well as binding affinity. Further experiments are performed on RNA secondary structures and also RNA aptamer-ligand complexes. Previous NFS studies were based on naturally occurring membrane channels such as α-hemolysin or on solid-state nanopores. Tailoring these systems to specific applications remains a challenging task, when altering the channel geometry or chemical modification becomes necessary. We report a new type of synthetic lipid bilayer membrane channel with user-defined geometric specifications that is constructed entirely from DNA. Scaffolded DNA origami is used to create a stem that penetrates and spans a lipid membrane, and a cap that adheres to the membrane in part via hydrophobic moieties. Synthetic channels spontaneously insert in lipid bilayer membranes as demonstrated in fluorescent dye influx assay experiments on giant unilamellar vesicles. The electrical conductivity of the membrane pores is studied by means of single-channel electrophysiological experiments. We find remarkable similarities to the behavior of biological ion channels such as "gating" caused by molecular fluctuations within the channel structure. More pronounced gating is seen for mutations in which a single DNA strand of the stem protrudes into the channel. Geometry and chemical properties of synthetic DNA channels can be tailored for custom nanopore sensing applications. We show that synthetic DNA channels can be used for single molecule studies on DNA structures. Synthetic DNA channels introduced here open up the perspective for further applications as antimicrobial agents and for interference with cellular homeostasis.

Zusammenfassung

Die Nanopore-Kraftspektroskopie ist ein vielseitiges Werkzeug für die Untersuchung von Einzelmolekül-Wechselwirkungen mit hohem Durchsatz, hoher Sensitivität und Genauigkeit. Nanopore-Kraftspektroskopie (NFS)-Experimente erlauben die Bestimmung der Dissoziationskonstante von molekularen Komplexen und deren spannungsabhängigen Entfaltungsraten. In unseren Experimenten wenden wir die NFS-Technik auf Aptamere an, die kurze einzelsträngige Nukleinsäuren sind, die eine Konformation annehmen können, in der sie an ein Molekül mit hoher Spezifität und Affinität binden können.

In dieser Arbeit berichten wir über eine neue Art von synthetischem Lipid-Doppelschicht-Membran-Kanal mit benutzerdefinierten geometrischen Spezifikationen, die vollständig aus DNA aufgebaut ist. Synthetische Kanäle treten spontan in Lipid-Doppelschicht-Membranen ein, wie in Fluoreszenz-Farbstoff-Einström-Assay und elektrophysiologischen Experimenten gezeigt wurde. Wir finden bemerkenswerte Ähnlichkeiten mit dem Verhalten von biologischen Ionenkanälen wie "Gating", die durch molekulare Fluktuationen innerhalb der Kanalstruktur verursacht werden. Geometrie und chemische Eigenschaften von synthetischen DNA-Kanälen können für spezifische Nanopore-Sensing-Anwendungen angepasst werden.

1 Introduction

Nanopore experiments are typically performed using peptide pores embedded within lipid bilayer membranes - most often utilizing the α-hemolysin (α-HL) membrane channel [81, 17] -, or "solid state" nanopores [72]. In nanopore experiments, the molecules are transported electrophoretically through a nanoscale pore. The translocation event generates a change in the pore's electrical conductance, which can be detected using electrophysiological measurement techniques. Observables such as the translocation time and the conductance change can then be used to derive kinetic and structural information about the analytes on a single molecule level. Both types of nanopores have their advantages - while solid state nanopores are typically more stable and allow application of higher voltages, biomolecular pores are usually smaller - suitable for smaller analytes - and structurally well-defined down to the molecular level. In the past a large number of studies on the translocation of small molecules or DNA has been performed in the context of "stochastic biosensing" [17] . Furthermore, using specialized measurement protocols, nanopore experiments can be modified to a "nanopore force spectroscopy" technique (NFS), which is closely analogous to other types of dynamic force spectroscopy such as atomic force microscope (AFM) or optical tweezer. One of the most attractive features of nanopore experiments is the straightforward exertion of forces to single charged molecules, as the force is simply proportional to the voltage drop across the nanopore. Dynamic force spectroscopy using nanopores was first developed by the Meller group for the study of the stability of DNA hairpins [107]. Nanopore force spectroscopic studies were performed on DNA secondary structures [131, 129, 136], DNA aptamers [7], and RNA structures using α-HL nanopores.

Nanopore force spectroscopy here utilizes the fact that a DNA duplex or a DNA molecule with a secondary structure cannot translocate through the ≈ 1.4 nm wide central constriction of the α-HL pore. The molecules first have to be "unzipped" - their secondary structure has to be broken - before they can pass through the pore. This unzipping process is force dependent, which in the context of nanopore experiments means that the rate of the unfolding process depends on the voltage. In a typical experiment, a (structured) molecule is initially captured in the pore at an elevated transmembrane voltage, causing a reduction of pore conductance. Electrophoretic capture of DNA (or RNA) structures into the pore is considerably enhanced by an unstructured "capture tail" sequence. In order to avoid immediate translocation of the molecule after capture, the voltage is then reduced and slowly ramped to higher voltages again. The secondary structure of the captured molecule may unfold at any time during the ramp, resulting in a complete translocation accompanied by an increase in conductance after the pore has been cleared. A statistical analysis of the unfolding voltages for varying voltage ramp speeds allows for the determination of folding and unfolding rates and the stability of the secondary structure. Specifically, we investigated DNA aptamers for the ATP and for the thrombin protein, unfolding of RNA secondary structures and the RNA malachite green aptamer. Binding of ATP to the aptamer resulted in the emergence of a stable population of aptamer-target complexes, which could be detected by a change in the critical unfolding voltage. NFS was applied to detect differential binding to AMP, ADP, and ATP and to extract kinetic information about the aptamer unfolding process. It is found that the stability of the thrombin aptamer is exponentially increasing with the concentration of potassium ions, which is caused by the formation of intramolecular G quadruplex structures. In order

to be able to perform unzipping experiments with the thrombin-aptamer at experimentally accessible voltages, the stability of its quadruplex structure was therefore reduced by lowering the potassium concentration and increase in the temperature.

Nanopores are a sensitive tool to study DNA secondary structure and DNA-ligand interaction. Beyond the study of DNA, nanopores hold great promise as a tool to acquire information about RNA. Despite their biological importance, much less work has been reported on the study of RNA molecules. Proof-of-principle experiments were performed and we showed that nanopores are an effective platform for studying RNA molecules and RNA-ligand interactions. Studies of RNA structures are performed replacing the repetitive capture sequences (such as poly(A)) with a non-repetitive, non-interfering sequence. The resulting RNA hairpin was considerably more stable than DNA hairpins, although, chosen DNA structure were thermodynamic more stable. Furthermore, a different production route was engaged by adding a poly(A) tail post-transcriptionaly using a *E. Coli* Poly(A) polymerase. Under this condition more complex structures as the malachite green aptamer and the flavin mononucleotide aptamer were studied.

Novel types of synthetic nanopores [95, 91] roughly analogous in shape to naturally occurring pore forming proteins were developed using the "DNA origami" self-assembly technique, which have advantages over previously studied peptide or solid state pores. For instance, origami-based channels can be custom-designed in shape, size and chemical functionality with precision on the molecular level. Synthetic membrane channels consist of an extramembranal cap structure, from which a hollow membrane spanning cylindrical stem protrudes. By using hydrophobically-modified DNA anchor strands, the cap structure can be attached to lipid bilayer membranes, while the stem penetrates the lipid membrane.

Experiments were performed at high salt concentration in order to avoid unspecific electrostatic interactions between the lipid membrane and DNA channels. The correct formation of the DNA channel and its incorporation into lipid bilayers could be proven in a range of experiments, including Transmission Electron Microscope (TEM), vesicles dye influx, electrophysiological experiments, and also single-molecule translocation experiments.

Our experiments suggested that channel insertion is dependent on the membrane composition and curvature, supporting the view that the stem can penetrate a more disordered, highly fluctuating membrane more easily. By increasing amount of cholesterol attachment sites, incorporation was facilitated into giant unilamellar vesicles (GUVs), which can be considered as a flat membrane. In electrical measurements channel insertion was supported by electrical pulses, leading to a transient membrane destabilization. The insertion of the channel structure can be stabilized by hydrophobic modifications and binding energies overcompensate the energy cost of channel formation. Experiments were performed using different lipids such as 1,2-diphytanoyl-sn-glycero-3-phosphocholine (DPhPC), 1-palmitoyl-2-oleoyl-sn-glycero-3-phosphocholine (POPC) and L-α-phosphatidylcholine EggPC forming liquid crystalline membranes, mixtures of POPC and sphingolipids which formed patches of disordered and solid ordered membranes. Two hydrophobic modifications were used, cholesterol preferring liquid ordered membranes and tocopherolol incorporating preferentially in liquid disordered membranes. Several designes of origami synthetic channels were created, starting with an initial design (lipid bundle) with scaffold loops on the top of the structure, with staple brakes right at the channel area and with 26 hydrophobic modifications. Channels have evolved to designs with scaffold loops integrated in the structure, with reduced breaks inside the channel region and with an increased number (57) of hydrophobic modifications. Conductance measurements on the DNA channels showed that the electrical characteristics are Ohmic with a conductance that correlates to the designed length and diameter of the channel. It is clear, however, that the assumption of an homogeneous electrical field within the channel is probably too simple. Most probably the origami structure itself is not

electrically insulating, allowing ionic current to leak through the side-walls of the channel - concentrating the electrical field and thus causing a current density in the region of the lipid membrane. Furthermore, as the channel supposedly creates a hydrophilic rather than a hydrophobic pore, additional leak current may flow between the membrane and the channel stem.

A highly interesting effect observed with DNA channels is the occurrence of spontaneous gating events. Channel gating is a discrete change in conductance that results from a spontaneous structural change or molecular rearrangement within the channels. For the synthetic channels gating is likely to correlate with stochastic unzipping and rezipping of short DNA double-helical domains in the channel. This effect was systematically studied, it was found that the gating varies with different channels and set-ups. The gating behavior was correlated to the applied voltage similar to the voltage-gated channels. More pronounced gating was seen for channels containing a mutation where a single DNA strand of the stem protruded into the channel. Gating is influenced by the position of the mutation but it is independent of the mutations sequence. Similar to the ion channels occurring in nature it was possible to create ligand-gated synthetic channels by adding a DNA aptamer at the entrance of the channel. It was expected current modulations due to ligand-induced conformation change of the aptamer. The time-series were analyzed with hidden Markov modeling tools which were adapted to our case.

We perform "unzipping" experiments with DNA hairpins and G-quadruplexes with DNA origami channels which contain a 2 nm diameter stem. Furthermore, the large DNA channel with a ≈4 nm diameter pore allows an electrically driven passage of double-stranded DNA molecules.

1.1 Lipids

Lipids are defined as hydrophobic or amphiphilic small organic molecules that are soluble in nonpolar solvents. Lipids are a major class of biological molecules, they are key components of the plasma membrane and other cellular compartments.

1.1.1 Lipid types

The lipids can be categorized into glycerophospholipids, sphingophospholipids and sterols. Glycerophospholipids consist of the triol glycerol connected to a phosphate headgroup on one of its hydroxyl positions and to fatty acids on the other two (see Figure 1.1 a). The fatty acid chains may be saturated, unsaturated (e.g., POPC) or branched (e.g., DPhPC) and their length typically varies between 16 and 20 carbon atoms. In contrast to glycerophospholipids, sphingolipids (e.g., sphingomyelin, SM) do not have a glycerol backbone, but consist of sphingosine - an 18 carbon amino alcohol with an unsaturated hydrocarbon chain, which is connected to a phosphate headgroup and to one either saturated or unsaturated fatty acid chain (see Figure 1.1 b). Under standar buffer conditions, the headgroups of glycerophospholipds or sphingolipids carry charges. Negatively charged headgroups (such as in PS or PG lipids) can mediate the interaction with cationic regions of membrane proteins. Positively charged lipids do not occur in nature, but synthetic cationic lipids such as TAP or DAB can promote the adhesion of cells [1] or can be used as transfection vectors [49]. Zwitterionic lipids, as phosphatidylcholines (PC), sphingomyelin (SM) and phosphatidylethanolamines (PE), carry both charges.

Sterols are non-polar lipids comprised of four hydrocarbon rings and a slightly hydrophilic OH group. The most important sterol in nature is cholesterol, which has a hydrocarbon chain

attached to its C5 ring (see Figure 1.1 c). Cholesterol alone does not form membranes, but interacts strongly with other lipids and lipid structures. Several models have been developed to describe these interactions [4]. Among those, the so-called "umbrella model" yields the best agreement with experimental data. It describes cholesterol-lipid interactions as non-specific and dictated by hydrophobic interactions [4, 70]. Experimentally, it is found that cholesterol preferentially interacts with sphingolipids [152]. Another example of an aromatic lipophilic molecule is tocopherol. It is one of the Vitamine E structures mainly found within the membrane of sub-cellular organelles, such a endoplasmatic reticulum and mitocondria rather than in the plasma membrane. Tocopherol posses a saturated phytol side chain, three methyl groups and a hydroxyl group attached to the benzene ring (see Figure 1.1 d).

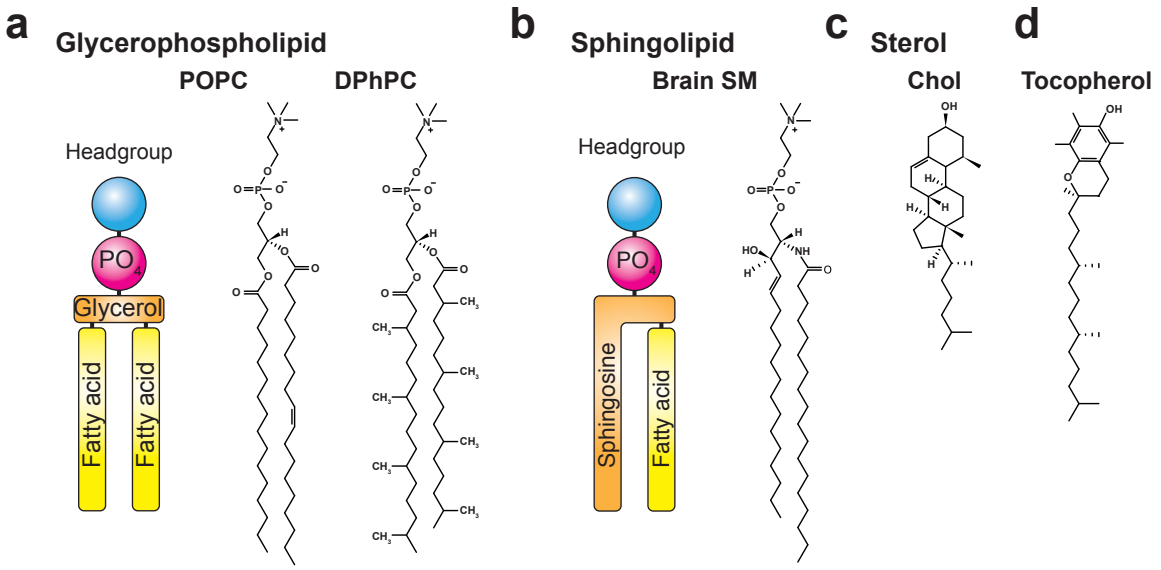

Figure 1.1: Structures of lipid types. a) Glycerophospholipids are composed of glycerol which connects a polar headgroup (a phosphate esterized with an alcohol) and two fatty acid chains. b) Sphingolipids are based on sphingosine, exemplified here by octadecanoyl (18:0) SM. c) Cholesterol d) α-Tocopherol

1.1.2 Lipid assemblies

The structural organization of lipids in water is determined by their concentration and the compromise between hydrophobic association, steric hindrance and ionic repulsive forces. Molecules that have an overall inverted conical shape such as detergents, lysophospholipids and phospholipids with short alkyl chains, self-associate and form micelles (see Figure 1.2 a). Lipid molecules with a conical geometry caused by a small polar headgroup form inverted micelles, as for example phosphatidylethanolamines (PE). Cylindrical phospholipids with long alkyl chains such as phosphatidylcholines (PC) and sphingomyelin (SM) preferentially form bilayer structures, which allow tight packing. Supported lipid bilayers are stable and easily accessible model systems that can be fabricated on solid substrates (see Figure 1.2 b). Re-hydration of dried lipid films leads to the formation of small and large unilamellar vesicles (SUVs and LUVs) with typical sizes of 10-100 nm and 0.1-1 µm. The additional application of an electrical fields [5] results in the formation of cell-sized giant unilamellar vesicles (GUV, Figure 1.2 c). Other techniques as inverted emulsion technique [36] or so called continuous

droplet interface crossing encapsulation technique (cDICE) [21] can be employed for creation of GUV's.

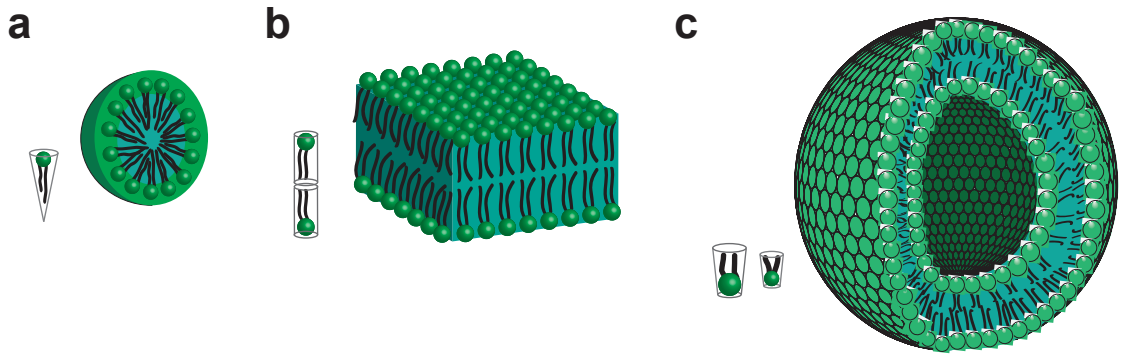

Figure 1.2: Lipid assemblies. a) Micelles, preferentially formed by lipids with an inverted conical shape. b) Planar lipid bilayers, formed by lipids with a more cylindrical shape. c) Vesicles are spherical lipid bilayers with a water core.

1.1.3 Phase behavior

Lipid bilayer membranes display a rich thermodynamic phase behavior. At low temperatures, membranes are in a solid-ordered phase (L_β), whereas at higher temperatures lateral order is lost and a liquid-disordered phase (L_α) is adopted. The phase transition temperature for the solid-liquid transition depends on the hydrocarbon chain length and on the lipid headgroup. Mixtures of lipids have a more complicated phase behavior and several phases may exist simultaneously. For instance, mixtures of cholesterol and phospholipids may obtain a liquid-ordered phase (L_o)where there is less thermal motion in the acyl chains of the lipid bilayer, bilateral movement in the plane of the bilayer still takes place. L_o phase has not been found in the absence of cholesterol. In this context, extensively studied model systems are three-lipid mixtures containing cholesterol, PC-lipids and SM. Their phase diagrams can be categorized into type-I and type-II diagrams. Type-I diagrams are characterized as not having a macroscopic L_o phase region and a L_α phase that coexists with the solid-ordered phase at lower cholesterol concentrations. Mixtures of DPPC/POPC/chol and brain-SM/POPC/chol [152, 151] are two typical examples showing type-I characteristics. Type-II phase diagrams have more regions of macroscopic immiscibility than the type-I mixtures, with at least three regions of two-phase coexistence and one region of three-phase coexistence. Examples of such mixtures are DPPC/DOPC/chol [151] or brain-SM/DOPC/chol [152]. It was found that in these mixtures, cholesterol is predominantly found in the L_o phase, which is rich in DPPC or SM, respectively. Segregated domains in the L_o phase are also called "lipid rafts". So far, raft domains were identified in model membranes but not in biological membranes of living cells, possibly due to technical limitations [125, 123]. The phase properties of membranes are assumed to play a key role in membrane functionality. For instance, it is known that membrane-associated proteins show clear preferences for particular phases. The majority of proteins prefers liquid over solid phases, with the exception of proteins that have a precise hydrophobic matching with the solid phase. For coexistent liquid-ordered and liquid-disordered states, most membrane proteins partition into the disordered phase.

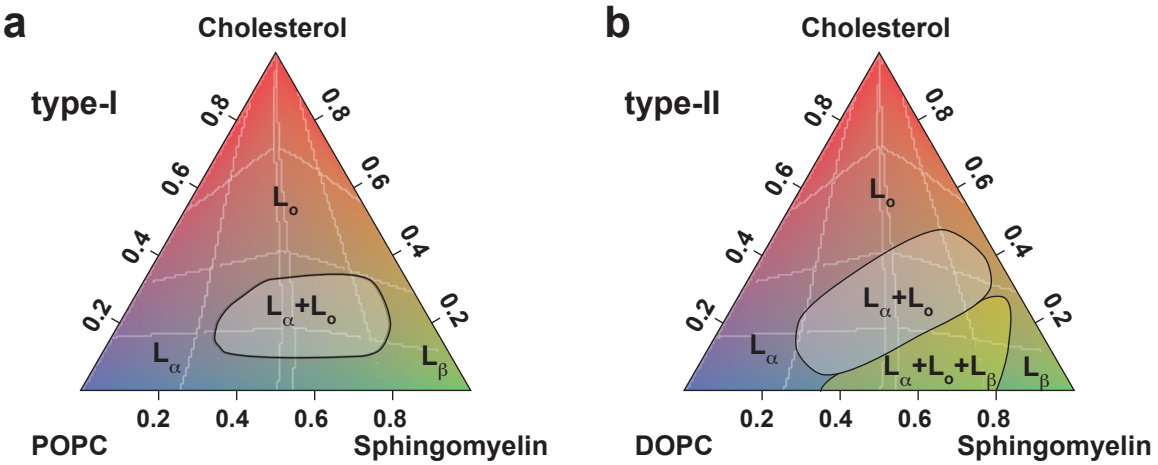

Figure 1.3: Phase diagrams. a) Lipid mixture of POPC, sphingomyelin, and cholesterol have nanoscopic domain dimensions for the coexistence regions (liquid ordered L_o and liquid crystalline L_α) b) Lipid mixture of DOPC, sphingomyelin, and cholesterol as for the type-I diagram for the type-II two phases (L_o and L_α) coexist. Additionally, for the type-II diagram, at low cholesterol concentrations, a third phase (solid-ordered L_β) is also found.

1.1.4 Membrane curvature

Membrane curvature is an important property of lipid bilayers. Higher curvature facilitates the incorporation of biological pores into membranes. Therefore pores incorporate better in SUVs than in LUVs [84]. The membrane curvature results from combined effects of lipids, proteins and their interactions. This effect is used for budding, fission and fusion, which involve changes of the membrane topology [106]. Large deformations of a lipid membrane cannot only be created by spontaneous curvature but also demand substantial forces that could be generated by specialized membrane proteins.

1.2 DNA-lipid interaction

Interactions between DNA and lipid bilayers are in general based on electrostatic forces between lipid molecules and the DNA backbone. However, binding of DNA to lipid membranes can also be achieved by hydrophobic modification of DNA molecules [139] or by conjugation to molecules interacting with membrane-bound proteins [74]. As a negatively charged polyelectrolyte, DNA strongly interacts electrostatically with cationic lipids such as DOTAP, DMTAP, DMDAP or DOTMA (see Figure 1.4 a). In the presence of cationic vesicles, DNA is compacted and spontaneously forms spherical complexes [49]. Fluorescence studies of DNA on cationic membranes show a strong coupling to the membrane, where the DNA molecules diffuse in two dimensions [66]. The interaction strength depends on the ionic environment and is highest at low ionic strength, where electrostatic screening effects are small [126]. In the presence of divalent cations such as Ca^{2+}, Mg^{2+} or Mn^{2+}, DNA also strongly binds to zwitterionic lipids [109, 58, 52], but the mechanism of the interaction is not fully understood. While for anionic lipids divalent cations are thought to bridge negatively charged lipid headgroups and the DNA backbone, for zwitterionic lipids the cations are thought to incorporate into the membrane and thereby bridge neighboring lipid molecules through their phosphate

groups. This neutralizes the negative charge on each lipid, resulting in a net positive charge (see Figure 1.4 b) [109, 58]. Some studies also report binding of DNA to zwitterionic lipids in the absence of divalent cations (see Figure 1.4 c) [2, 100]. Theoretical studies also suggest a mechanism based on ion-dipole interaction, with an expected binding strength reduced by a factor of four compared to that in cationic lipid - DNA complexes [86]. Again, monovalent ions are presumed to weaken DNA-lipid association. Electrostatic binding is also affected by lipid composition and phase behavior. Experimentally, dsDNA was observed to preferentially bind to the L_o phase [103, 82], which may be explained by the increased surface charge density caused by the higher packing density of the lipid headgroups. In the presence of Mg^{2+} a stronger interaction has been observed for PE membranes compared to PC membranes, which may be due to the smaller PE headgroups interacting more favorably with the cations.

For many applications, it is desirable to attach DNA-based nanostructures to lipid membranes more directly, which may be achieved using conjugates with lipids or other hydrophobic molecules (see Figure 1.4 d-e). An important property of lipophilic DNA conjugates is their domain partitioning behavior. As for many membrane proteins, distinct lipid modifications may be used to target specific sites on the cell membrane [99, 132, 141]. Due to its commercial availability, cholesterol (see Figure 1.4 d) is one of the most commonly used lipids for DNA conjugation, although its association with membranes is rather weak compared to other lipids [124]. This can be compensated, however, by the use of multiple cholesterol functionalizations. Already a combination of two cholesterol anchors was observed to significantly increase the binding affinity and leads to almost irreversible binding, with an unbinding rate at least one order of magnitude lower than for a single cholesterol anchor. The nature of the linker through which cholesterol is attached to DNA is of importance. Cholesterol itself influences lipid membrane packing, condenses the membrane and increases its order [25]. It was observed that cholesterol linked to tetraethylene glycol (TEG) does not alter membrane packing or structure. The phase behavior of cholesterol-DNA conjugates is more intricate than for other lipid-DNA conjugates. In DLPC:DPPC:chol mixtures with coexistent solid and fluid phases, chol(-TEG)-DNA conjugates were observed to partition into the fluid phase (L_α) only [18]. In mixtures containing two fluid phases (L_α, L_o) such as DOPC:DPPC:chol, chol(-TEG)-DNA conjugates distributed almost evenly into both phases, while cholesterol alone is known to strongly prefer the L_o-phase. Bivalent conjugates, however, were observed to prefer the L_o over the L_α phase for this lipid mixture. In contrast to cholesterol, tocopherol conjugates (see Figure 1.4 e) were observed to specifically partition into the liquid-disordered domains for lipid mixtures containing two fluid phases (POPC:SM:chol) [93]. The specific attachment of DNA nanostructures via hydrophobic modifications is possible only if electrostatic interactions are comparably weak.

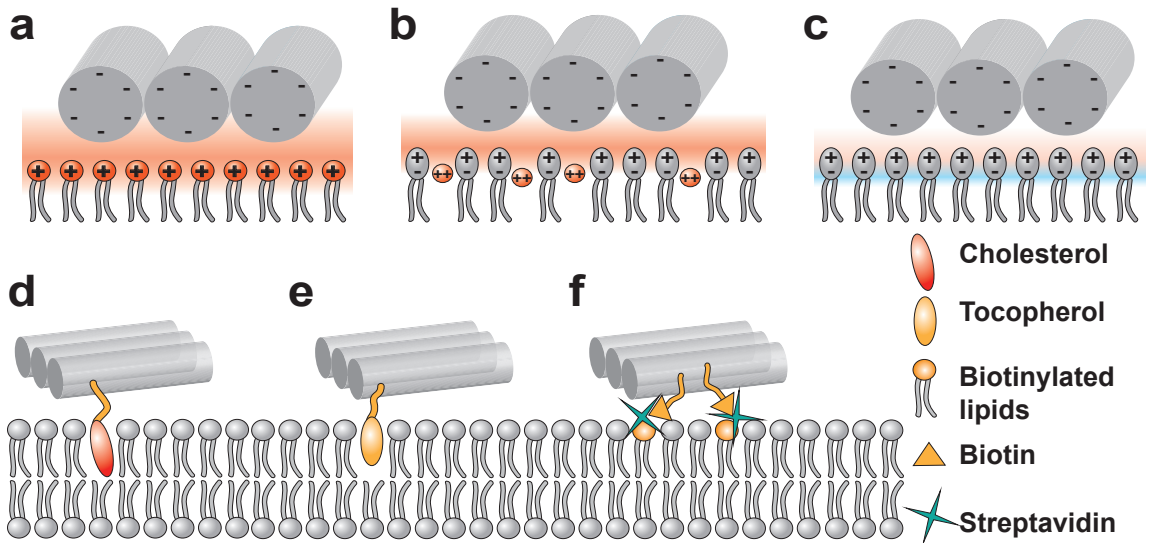

Figure 1.4: DNA-lipid interactions. Electrostatic binding to a) cationic lipids, b) zwitterionic lipids in the presence and c) in the absence of divalent cations. Amphiphilic DNA conjugates with d) cholesterol or e) tocopherol. f) Interactions involving streptavidin linkages between biotinylated staple strands at the bottom of the origami and biotinylated lipids.

While hydrophobic nucleic acid modifications are the most commonly chosen method to label lipid bilayers, receptor mediated interactions have also been reported. Biotinylated DNA has been attached to biotinylated lipids (see Figure 1.4 f) within liposomes using streptavidin cross-linkers [60].

1.3 Nanopores

The cell membrane acts as a selective barrier with low permeability to ions and large molecules. Channels and transporters, which comprise of proteins and peptides, control exchange of solutes across the hydrophobic barrier of cellular membranes. In nature, these nanopores have diverse and essential functions that range from maintaining cell homeostasis and participating in cell signaling to activating or killing cells.

1.3.1 Biological nanopores in molecular sensing applications

In the past, nanoscale membrane pores have shown great potential as single molecule biosensors [81, 17, 72, 39, 61, 24, 102, 104] and for sequencing of long strands of DNA [104, 35] or RNA [8]. In nanopore experiments, channels are incorporated into lipid membranes and, which change the permeability of ions. The application of a transmembrane voltage therefore causes a measurable current. Changes in the current resolved by an amplifier could be used to identify molecules that are electrophoretically captured in and potentially translocated through the pore. In a way, this method is a molecular-scaled version of the resistive-pulse sensing technique suggested by William Coulter to count particles suspended in a fluid. The type of sensing task that can be accomplished with such nanopores depends on their size and their chemical structure. αHL is a water-soluble toxin secreted by the pathogenic bacterium *Staphylococcus aureus*. The pore heptamer has a hollow mushroom-like shape consisting of a stem ($\approx$2.6 nm in diameter; $\approx$5 nm in length), a cap (3.6 nm in diameter; $\approx$5 nm in length), and a rim domains. The pore is narrowest at the vestibule - transmembrane domain junction with a diameter of $\approx$1.4 nm (see Figure 1.5 a). The interior of the β-barrel is primarily hydrophilic while the exterior has a hydrophobic surface. The incorporation of the toxin is voltage dependent and consist of two steps, first the water soluble monomers attaching to the lipid membrane, when the critical concentration is reached seven absorbed monomers associate and form the nanopore [130]. The first αHL channel reconstitution in the model bilayers membranes was performed by Krasilnikov and co-workers [89]. Large pore dimensions and structural robustness of the αHL heptamer permit the wide usage of this bacterial toxin in a variety of developing biotechnological applications. For example as a stochastic sensing of various analytes including metal ions [23], small organic molecules [59], DNA [81], RNA [81], proteins [112].

DNA unzipping experiments exploit the limitations of the αHL pore size that allow passage of only ssDNA and not double-stranded DNA (dsDNA) [81, 153]. Thus, in order to translocate dsDNA or ssDNA with secondary structure, the molecules first have to be unfolded. The unfolding process can be facilitated by the application of a transmembrane voltage and, hence, the lifetime of the translocating molecule in the pore becomes voltage-dependent. Another widely used nanopore is MspA (*Mycobacterium smegmatis* porin A) a octameric channel pore which allows the transport of water soluble molecules across bacterial cell membranes. It contains a single constriction $\approx$1.2 nm wide and 0.6 nm long which could offer improved spatial resolution [48], compared to αHL (see Figure 1.5 b). Wild type MspA was engineered to remove the negative charges at the constriction and allows DNA translocation [31].

Futhermore, measurements of changes in the current through αHL and MSPA pores can now be decoded into a DNA sequence. In order to be able to read nucleotide-specific current levels phi29 DNA polymerase was attached to the DNA template leading to a controlled sequential movement [104, 35]. However, nanopore devices lack the spacial resolution required for single base recognition, instead several nucleobases in a strand of DNA contribute to each of the measured current levels. In order to improve nanopore sequencing accuracy, a new

nanopore should be designed that allows only 1-2 nucleobases to contribute to the current levels and a complex algorithms for deciphering sequence [35, 104].

A biological nanopore that can allow translocation of dsDNA is the phi29 connector channel [163]. The length of the connector is ≈7 nm, while the cross-sectional area of the channel is 10 nm^2 (3.6 nm in diameter) at the narrow end and 28 nm^2 (6 nm in diameter) at its wider end (see Figure 1.5 c). The most significant advantage of the phi29 system, different from other well-studied systems, is that the phi29 connector has a larger channel allowing for the passage of ssDNA, dsDNA, peptides and possibly small proteins. The larger pore size is also advantageous in that it makes it easier for channel modifications to either create a sharper detection region for attaining single nucleotide resolution or for the insertion or conjugation of chemical groups for sensing and diagnostic applications [63].

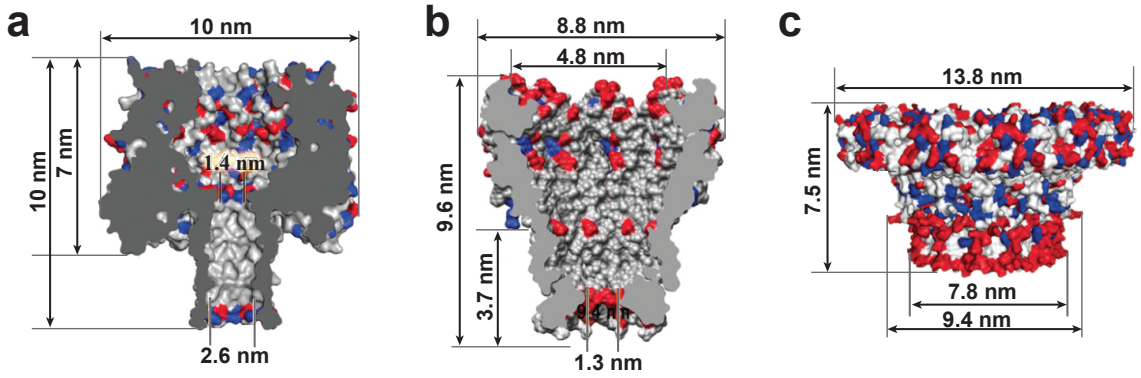

Figure 1.5: Structure of biological nanopores. a) Heptameric αHL toxin b) Octameric MspA porin c) phi29 connector channel

1.3.2 Synthetic Nanopores

There is much interest in developing synthetic analogues of biological membrane channels with high efficiency and exquisite selectivity for transporting ions and molecules. Solid-state nanopores have emerged as a alternative to biological nanopores because of their properties including well-defined geometries and dimensions, mechanical robustness. The diameter of the solid-state nanopores can be controlled ranging from sub-nanometers to hundreds of nanometers according to the experimental requirements [39]. Functionalization of solid-states appears to be difficult [161, 169], in this context αHL was inserted in SiN pores [61]. In contrast to solid-states nanopores αHL possesses an atomically precise structure and the potential for site specific genetic engineering or chemical modifications. Another approach was to replace the αHL with a DNA origami structures, that allow easy functionalization and size variation using methods of DNA technology [162].

Membrane-bound synthetic channels could be used for the study of processes in membrane biology, they could constitute components of cell-scale bioreactors, or they could be utilized as membrane-bound biosensors. It was shown that short carbon nanotubes (CNTs) spontaneously insert into lipid membrane allowing the passage of water, protons, small ions and DNA [53]. However, their use in large-scale applications has been hampered by difficulties in producing CNTs with subnanometer pore diameters and fabricating membranes in which the CNTs are vertically aligned. With the recent advances in DNA nanotechnology it has become possible to realize DNA nanostructures that mimic the functions of proteins, and the imitation of membrane-associated proteins is particularly promising in this context. In contrast to solid-state nanopores, DNA-based pores can be produced with molecular precision

and chemically functionalized via incorporation of appropriate DNA bioconjugates. Protein or peptide membrane pores also offer molecularly defined dimensions, but their geometry cannot be modified as easily as for DNA nanostructures, and their chemical functionalization typically is more cumbersome. The realization of artificial membrane-penetrating pores is challenging, however. The energetic cost associated with the insertion of DNA into the hydrophobic core of a lipid membrane is prohibitively high. Considering the difference in electrostatic energy in water and in the membrane, already the insertion of a single monovalent ion would cost several 100 kJ/mol. However, by appropriate hydrophobic functionalization it is in fact possible to achieve stable incorporation of DNA nanostructures into lipid bilayer membranes. Electrical single channel recordings demonstrate the correlation between channel geometry and electrical conductance [95, 94, 91].

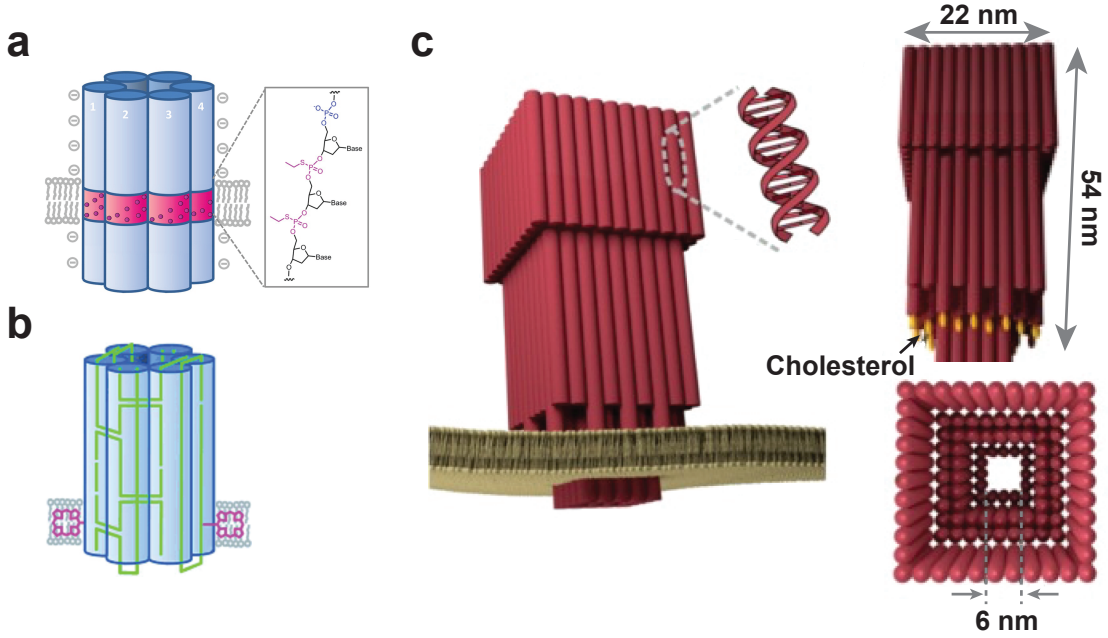

Figure 1.6: Structure of synthetic nanopores. a) Schematic representation of a DNA nanopore composed of six interconnected duplexes represented as cylinders. On the external face, the barrel features a membrane-spanning hydrophobic belt (magenta) where conventional phosphates of the DNA backbone are substituted by charge-neutral phosphorothioate-ethyl groups (inset). b) Small DNA pore anchored in the lipid membrane with the magenta porphyrin tags. c) Design (side and top views) and dimensions of the large DNA porin with 19 cholesterol tags (orange).

Recently, independent from our work, small-pores assembled from few oligonucleotides were realized, membrane incorporation was facilitated by a hydrophobic ring made from either ethyl-thiophosphate (see Figure 1.6 a) [28] or porphyrin groups (see Figure 1.6 b) [30], and was also shown to successfully penetrate lipid bilayer membranes in electrical recordings. They also demonstrated voltage-induced conductance switching [138]. In contrast to these pores, our structures are typically more rigid, they support larger currents and the transport of large molecules. Evidence for cytotoxic effect of small DNA pores was provided [27] and also demonstrated small molecule transport in the context of SUVs [29]. Similar with our large synthetic pore Göpfrich et al [56] presented a large DNA channel (see Figure 1.6 c)

with a very high conductance (40 nS). Notably, over the past years the group of Aleksei Aksimentiev performed various molecular dynamics simulations of DNA membrane pores. His simulations suggest strong ionic conduction and electroosmosis along the DNA helices of the channel structures [168].

1.4 Single channel recordings

Electrophysiological recording of single-channel currents is a direct method for obtaining detailed and precise information about the kinetic behavior of pore-forming membrane channels. In order to detect fast opening and closing of the channel a sensitive amplifiers with minimal filter frequency is required.

1.4.1 Channel gating

Gating - the property of opening and closing of a transmembrane pore - originates from the temporary establishment or removing of a permeation barrier. There are several classes of gated ion channels: ligand gated ion channels which are triggered by the binding of a ligand to a channel [69, 96], voltage gated ion channels [69, 171], pressure sensitive channels (mechanosensitive channels [145]) or temperature sensitive channels (transient receptor potential channels [37]). But the gating mechanism is yet not fully understood.

Voltage gating behavior was intensively studied for selective ion channels and is characteristic for large diameter beta barrel pores isolated from the outer membrane of gram negative bacteria. It was considered that the constriction area formed by a surface loop dangling in the pore lumen can induce gating. Two possible origins of voltage gating were hypothesized. The gating can be caused by steric occlusion of the channel by the loop or transient fluctuations in the intrinsic electric field created due to the charges present on the loop. These hypotehesis could not be confirmed, it was found that the loop movement can affect the gating but is not the primary gating mechanism.

The latest hypothesis considers that voltage-dependent conformational changes of extracellular loops could lead to decreased ion flow [15]. An example of voltage gated pores is MspA, which shows gating behavior at high voltages, the initial hypothesis was that the L6 persimatic loop is responsible for the closing of the pore [76]. Gating of the MspA was reduced by mutating the negative charges at the constriction region to neutral or positive charges [31]. Another kind of porin-like voltage gated pores are pore-forming toxins [88]. They form a smooth, open cylinder and thereby in comparison to porins they do not have a loop or an eyelet. Here, voltage gating was found to be a general property of β-barrel structures rather than of any particular sub-structure. However it is unlikely that the β-barrel undergoes large structural changes that could lead to pore closure due to the large number of hydrogen bonds between adjacent strands [12]. Other factors that might influence the critical gating voltage are the lipid surface charge and the membrane thickness.

Voltage gated pores such as OmpF and OmpC present spontaneous current flickering events of different depth. These less deep transitions are called sub-conductance states or substates. The sub-conductances show neglegible voltage dependence and from a critical voltage on an interplay might exist [14] between gating and sub-conductance gating. The authors hypothesize that sub-conductance levels are governed by short-lived, repeated conformational changes of the pore and not by electrostatics. Furthermore, fluctuations of certain residues and the thereby caused conformational changes are suspected to be the main cause for the appearance of sub-conductance states. However other influcences as the plasticity of the pore, other external loops or the presence of lipopolysaccarides were not excluded as cause. Note also that loop L3, located in the porin loomen, is believed to be involved [19].

It was found that the appearance of sub-conductance events are set-up dependent. These sub-conductance states appear rather in patch clamp experiments [40] than in classical BLM experiments, but also exist in BLMs under certain conditions [115]. An explanation of such behavior is the size of the BLM. The bilayer has a typical diameter of a few hundred microns,

which makes the bilayer more adaptive to mechanical stress, as any stress can be distributed across a large surface area. In contrast, the planar lipid bilayers on patch clamp pipettes, glass chips [90] as well as nano-BLMs [137] are very small. Hence, they are more rigid and any mechanical stress posed on the bilayer can act more directly on any reconstituted protein, which could be the reason for the increased sub-conductance activity. An explanation for the absence of documantation of fast transitions in BLM studies proposed by Delcour et al. [40] is that it doesn't originate from different porin behavior but from the high filtering of the data, which is often used in BLM experiments [14].

Some carbon nanotubes incorporated into lipid membrane present conductance signal oscillations. They exclude the rapid removal and re-insertion of the CNT porins from the bilayer, or wetting/dewetting transitions in the channel as causes of sub-conductance events. One possibility is that these sub-states represent a spontaneous transition between ionic-penetration and ionic-exclusion states, as predicted for weakly charged or neutral nanopores.

1.4.2 Nucleic acids-translocation experiments

Nanopores can be utilized as stochastic single molecule sensors. Here, a voltage is applied across a pore-containing membrane, and the current due to ion flow through the pore is measured. Electrophoretic translocation of analyte molecules leads to a reduction in channel current, whose duration and depth depend on the charge and size of the analytes (see Figure 1.7).

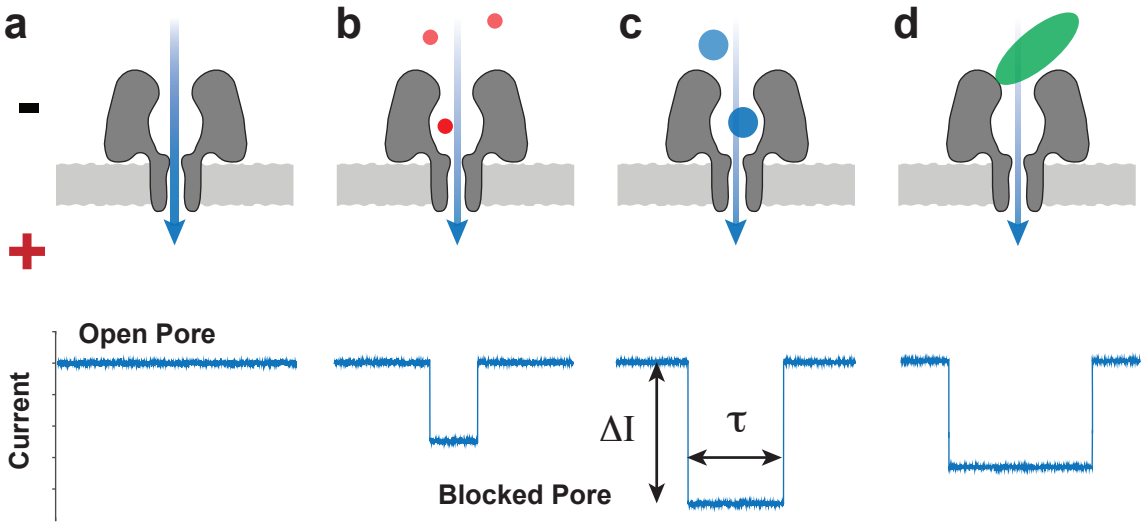

Figure 1.7: Translocation experiments. a) Open channel current b) Open current reduction due to the passage of small analytes. c) Current blockades when larger molecules are trans locating. The current blockade amplitude and the dwell-time are recorded. d) Current blockades are detected for larger molecule that binds to the channel but can not translocate.

1.4.3 Nanopore Force Spectroscopy

Mechanical force at the molecular level are involved in the action of enzyme binding, artificial manipulation, or strand separation during cell division. In these contexts, results provided by nanopore force spectroscopy are crucial for understanding mechanical deformation that

DNA and RNA may experience. *Nanopore Force Spectroscopy* (NFS) is a technique similar to related techniques based on optical tweezers or AFM. In contrast to other force spectroscopy techniques, NFS experiments do not require any labeling of the molecules under study to facilitate binding to either AFM tips, surfaces, or silica beads. Instead of the long linker molecules required for optical tweezers studies, a relatively short sequence extension is sufficient to facilitate the electrophoretic capture of the molecules in the pores. In addition, nanopore-based measurements have a considerably higher throughput than other single-molecule techniques. Nanopore force spectroscopy experiments can be performed at constant force or at constant loading rate (force ramps) where the force increases over time. After capturing a DNA molecule (or other molecular complex) inside a nanopore, the voltage applied across the membrane is ramped from low to higher values. When the electric force acting on the charged molecule is sufficient to break its secondary structure, it unfolds and is pulled electrophoretically through the pore. In order to reconcile experimental results with theoretical predictions based on standard thermodynamic parameters for DNA base-pairing, we utilized a measurement strategy, in which the molecules under study are pulled through the nanopores in reverse direction (from the *trans* to the *cis*-side of the membrane), as the αHL pore interacts less with the analytes on the *trans* side (see Figure 1.8). For simple DNA hairpin molecules, this measurement strategy resulted in a very good agreement between experimental and theoretical unfolding rates [136].

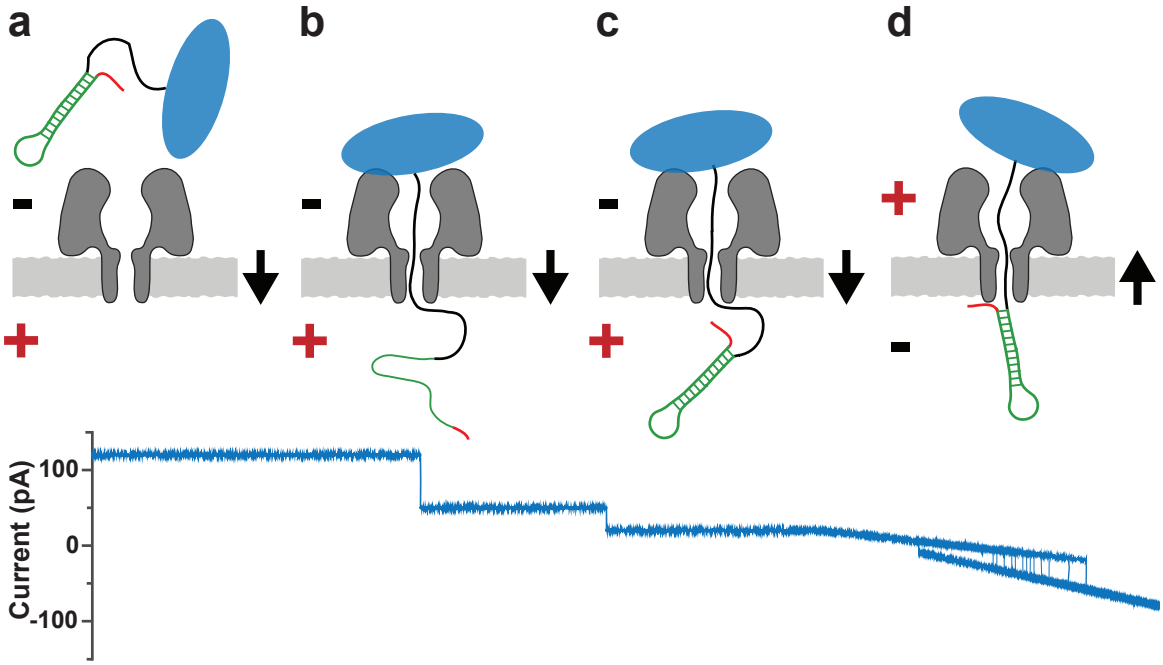

Figure 1.8: Dynamic force spectroscopy. a) The hairpin first translocated through an αHL nanopore b) Catching event is detected and the voltage is reduced to lower values c) The molecule is allowed to refold for a specified time d) After reversal of the voltage polarity, the hairpin is pulled back.

Nanopore experiments can be utilized to study the interaction of DNA and RNA with molecules if this interaction results in a detectable change in pore residence time or conductance. This has been used to study the interaction of DNA with DNA-binding proteins such as exonuclease I [71], RecA [142] or small molecules like intercalating dyes [160]. In this thesis NFS was utilized to study DNA and RNA aptamers with their target molecules.

1.5 Aptamers

Aptamers are DNA or RNA structures that bind strongly and specifically to small molecules or proteins. They can be extracted from pools of DNA or RNA molecules containing randomized sequence regions using a selection procedure known as SELEX (Systematic Evolution of Ligands by EXponential Enrichment) [150, 47]. Aptamers often bind their molecular targets as strongly as protein antibodies, with dissociation constants K_d, typically in the nanomolar to micromolar range. In fact, due to the simplicity of the selection procedure and the ease of production and modification of known structures, aptamers have become promising alternatives to antibodies in many applications. For instance, a wide range of aptamer-based sensors has been reported in the past decade [13, 144] and the first aptamer-based drugs (acting as inhibitors of their enzymatic targets) are in the market [83]. Furthermore, aptamer-like motifs have been found to play an important role in gene regulatory processes in bacteria, where they act as ligand-recognition regions of riboswitches [149].

In spite of their growing importance, the molecular structure of only a few aptamers have been characterized so far. In many cases it is not clear, which of potentially several conformations of an aptamer is the active, binding form, and which molecular contacts are responsible for the binding interaction itself. Depending on experimental conditions and characterization method, reported aptamer-ligand dissociation constants often vary widely, and conformational kinetics are typically not studied.

Aptamer-ligand interactions are usually investigated using bulk methods such as surface plasmon resonance [147, 158, 144], quartz crystal microbalance experiments [147, 68, 144], or electrophoretic band shift assays [13]. Kinetic experiments were performed using various spectroscopic titration methods like stopped flow [80, 51], NMR [118, 117], EPR [34], fluorescence anisotropy [55] or FRET [114].

Single molecule studies yield additional and complementary information on molecular recognition interactions. They allow a more direct analysis of kinetics of systems with multiple states, the determination of molecular distributions, and the detection of rare events [41]. Only few single molecule experiments have been concerned with the characterization of aptamer folding and ligand binding so far. For instance, the aptamer domain of several riboswitches was studied using single molecule force spectroscopy with optical tweezers [57, 6, 116] or single molecule FRET [62, 50]. In other studies, the well-known thrombin aptamer was investigated using optical tweezers [87] and AFM [101, 170]. An alternative single molecule characterization method is based on nanopore conductance studies.

This thesis focuses on two model DNA-aptamers, ATP and thrombin binding aptamer. The ATP binding aptamer (see Figure 1.9 a) contains two highly conserved guanine-rich regions, two invariant adenine residues and two regions of predominant Watson-Crick covariation. Huizenga and Szostak [77] proposed that the ATP-binding pocket was centered about two bulges containing adenine residues, which flank a G-tetrad and helical stems that emanate from this G-quadruplex platform. A new model was proposed after NMR studies in contrast with the previous model it was found that two AMP target the aptamer through identical G-A mismatch formation as they intercalate. The recognition G-A mismatch stacks with a reversed Hoogsteen G-G mismatch in one direction and with an adenine base in the other direction [98].

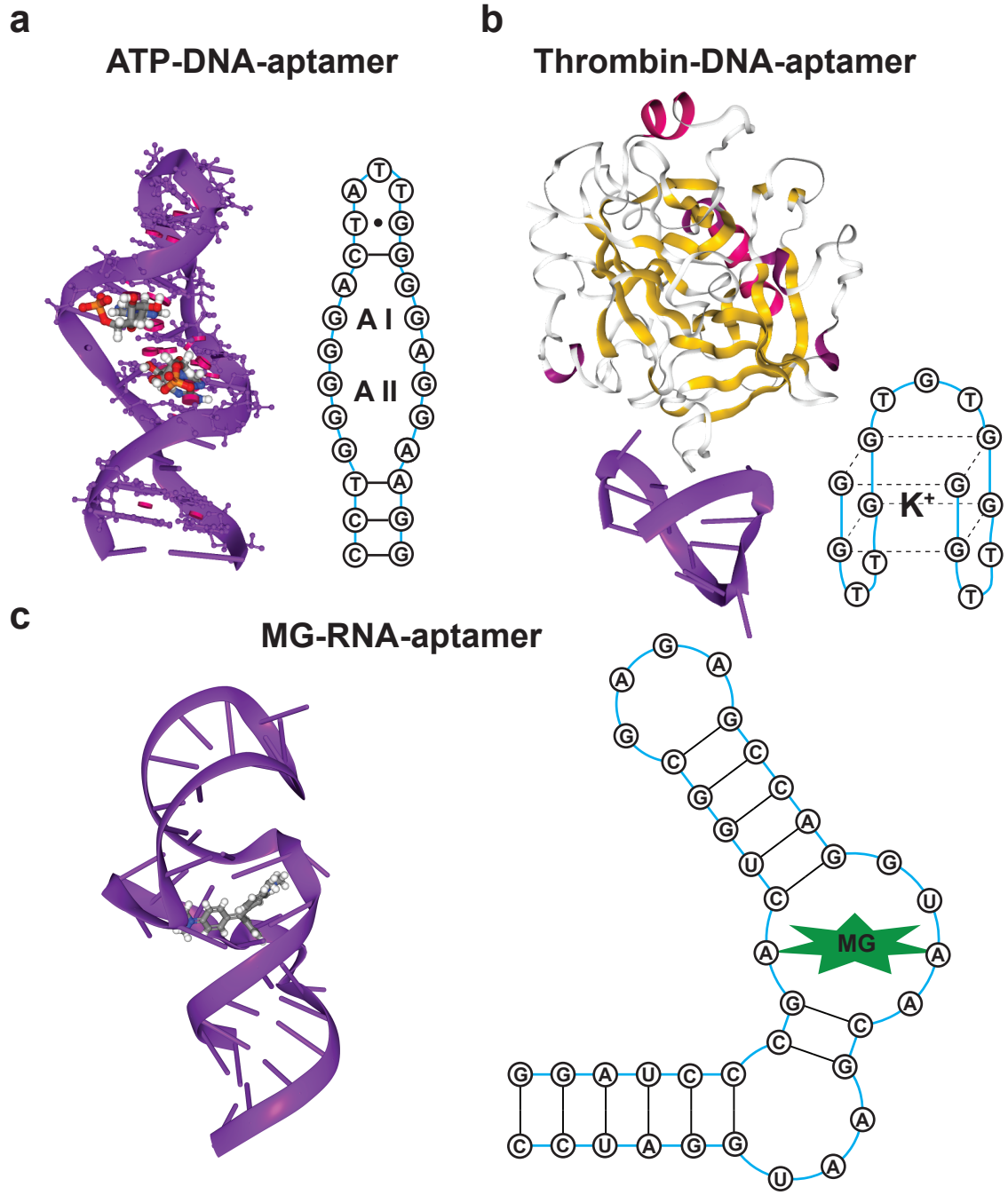

Figure 1.9: DNA and RNA aptamer structure. a) ATP-DNA aptamer with two AMPs bound. b) DNA-G-quadruplex bound to a α-thrombin protein c) Malachite green RNA-aptamer. The binding pocket consist of a base quadruple a Watson-Crick base pair flanked by two helices

The thrombin binding aptamer (see Figure 1.9 b) structure is known to form a G-quadruplex in solution, which is stabilized by monovalent cations localized between the two G-quartets of the structure [121]. This aptamer differs from the ATP aptamer in several aspects: i) the K_d of the aptamer target complex is several orders of magnitude lower, and ii) the secondary structure of the aptamer is comprised of two stacked G quadruplexes,

which themselves are extremely stable structures, even in the absence of the target. The quadruplex stability was found to be strongly dependent on the cation type [92]. In the presence of 100 mM KCl and NaCl, melting temperatures of $51 \pm 1°C$ and $23 \pm 1°C$ were found, respectively. In another study, the quadruplex stability was characterized as a function of overall ionic strength in KCl solution using AFM force spectroscopy and a strong dependence was found [101].

In contrast to the DNA-aptamers, RNA aptamers are more commonly found in the nature, in general they are a part of riboswitches. A proof-of-principle experiment was presented showing a malachite green (see Figure 1.9 c) binding to its RNA-aptamer. The malachite green aptamer is known to activate the fluorescence of the ligand molecule upon binding. Affinity studies of the RNA to its target were previously done using nanopore experiments [159], in our case we used nanopores to determine the binding strength. The binding pocket of the aptamer is formed by an asymmetric loop flanked by RNA helices [16]. The dissocitaion constant was found to vary between 2.7 µM [38] and 100 nM [11, 16] depending of the used buffer.

2 Materials and Methods

2.1 Electrophysiology

A principle common to all currently available variants of ion current recording through either cell membranes or artificial lipid bilayers is that the measurement takes place across a small aperture in an electrically insulating material separating two electrolyte-filled compartments which are connected to a potentiostat (or: voltage clamp) circuit.

αHL from *Staphylococcus aureus* was purchased from List Biological Laboratories (Campbell, CA). HPLC purified oligonucleotides (biomers, Ulm, Germany) were dissolved in 10 mM Tris, 1 mM EDTA solution at pH 8. The DNA sequences used in this study were (complementary regions are underlined):

- ATP aptamer (`ATPapt`):
  5´-GGCGCCGCGGCCTTTTGGCCGCGGCGCC-$(dT)_{50}$-
  CCTGGGGGAGTATTGCGGAGGAAGG-$(dT)_{30}$-3´
- Modified ATP aptamer (`ATPapt-mod`):
  5´-GGCGCCGCGGCCTTTTGGCCGCGGCGCC-$(dT)_{50}$-
  AACCTGGGGGAGTATTGCGGAGGAAGGTT-$(dT)_{28}$-3´
- Thrombin aptamer (`Thapt`):
  5´-$(dT)_{50}$-GGTTGGTGTGGTTGG-3´

Adenosine triphosphate (ATP), adenosine diphosphate (ADP) and adenosine monophosphate (AMP) were purchased from Sigma Aldrich, Munich, Germany. Human-α-thrombin was supplied by Hematologic Technologies (Vermont, USA).

2.1.1 Droplet set-up

Emulsion droplet based lipid bilayer set-up as previously described in Ref. [131]. Briefly, two Ag/AgCl electrodes reside in a lipid-oil mixture (10 mg/ml DPhPC (Avanti Polar Lipids, Alabaster, AL, USA) in hexadecane (Sigma Aldrich, Munich, Germany)). Onto both electrodes an aqueous droplet is added, causing monolayer formation. When the droplets are brought into contact, the oil between the monolayers is displaced and a droplet-interface bilayer (DIB) forms (Figure 2.1 a). Droplets can be created either by hand-pipetting aqueous solutions into the oil (in volumes reliably as low as 100 nl), or by using microfluidic junctions that combine oil/lipid and aqueous streams.

Positioning the droplets in close proximity allows a stable bilayer formation. A micropipette was used to inject αHL locally, close to the bilayer. In contrast, the DNA nanopores are added to one of the droplets, defining the *cis* side of the membrane. Incorporation of a single pore is facilitated by applying negative voltage pulses.

The ionic current through the pore was measured using a patch clamp amplifier (EPC9, HEKA Elektronik GmbH, Lambrecht, Germany). Temperature can be varied in our set-up, for the cases presented here, experiments were performed at 23 °C or 37 °C

2.1.2 Orbit 16

A 16 channel microelectrode cavity arrays (MECA) developed by Baaken et al. [9] were interfaced using an Orbit 16 device, provided by Nanion Technologies GmbH, Munich, Germany. MECA allowed us to work with small sample volumes (pl) and increase the throughput of our measurements. The set-up has 16 array of cylindrical cavities with diameters 3 µm to 10 µm connected to 16 amplifiers (Tecella Inc., Costa Mesa, CA, USA) with relatively low temporal resolution via a gold conductor line. Depending on the type of experiment, measurements on a single spot were performed with a dedicated low noise patch clamp amplifier (EPC9, Heka). To form a lipid bilayer 100 µL of electrolyte solution were added to the measurement chamber, the ground Ag/AgCl electrode resides in the *cis* (upper) compartment. 1 µL to 2 µL of lipid solution were pipetted in the vicinity of the cavities followed by painting the lipid bilayer on top of the cavities using a magnetic stir bar. Several lipid types were used to paint the membrane. The most common used is the DPhPC, some experiments were made with POPC and POPC-SM mixtures. Notably, conduction events for ions were observed in the lipid membranes in the absence of nanopores. Similar events were previous described by Heimburg [65, 111].

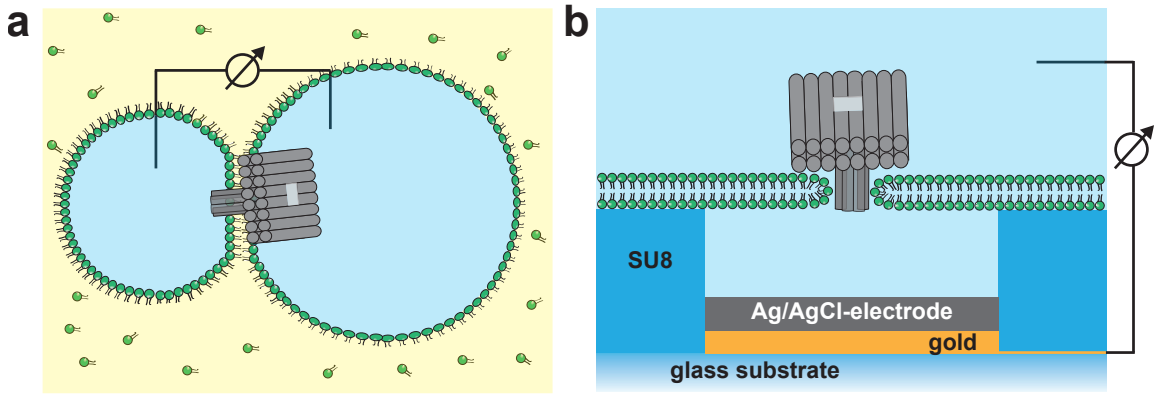

Figure 2.1: a) Schematic representation of two emulsion droplets in a lipid/oil bath electrically connected to a patch clamp amplifier with Ag/AgCl electrodes. A lipid bilayer containing a single nanopore is formed by the monolayers at the oil-water interface. b) Schematic depiction of a cavity, fabricated onto a glass substrate by lithographic structuring of an 8 µm thick layer of SU-8 photoresist. On the bottom of the cavity an Ag/AgCl electrode is created by evaporation of gold followed by electrochemical deposition of a silver layer and subsequent chlorination. After forming a lipid bilayer across the cavities, membrane channels can be incorporated and current recordings can be performed.

2.1.3 "Fast Electronic Trigger Technique"

In case of the Fast Electronic Trigger Technique, experiments were performed using a capture sequence (poly(A) for RNA and $(dT)_{50}$ for the DNA). After catching the nucleic acid molecule at 120 mV bias voltage, a fast electronic trigger circuit immediately reduced the voltage, followed by a voltage ramp that unfolded the secondary structure (Figure 2.2). Experiments can be performed in forward (from *cis* → *trans*) or backward (*trans* → *cis*) direction.

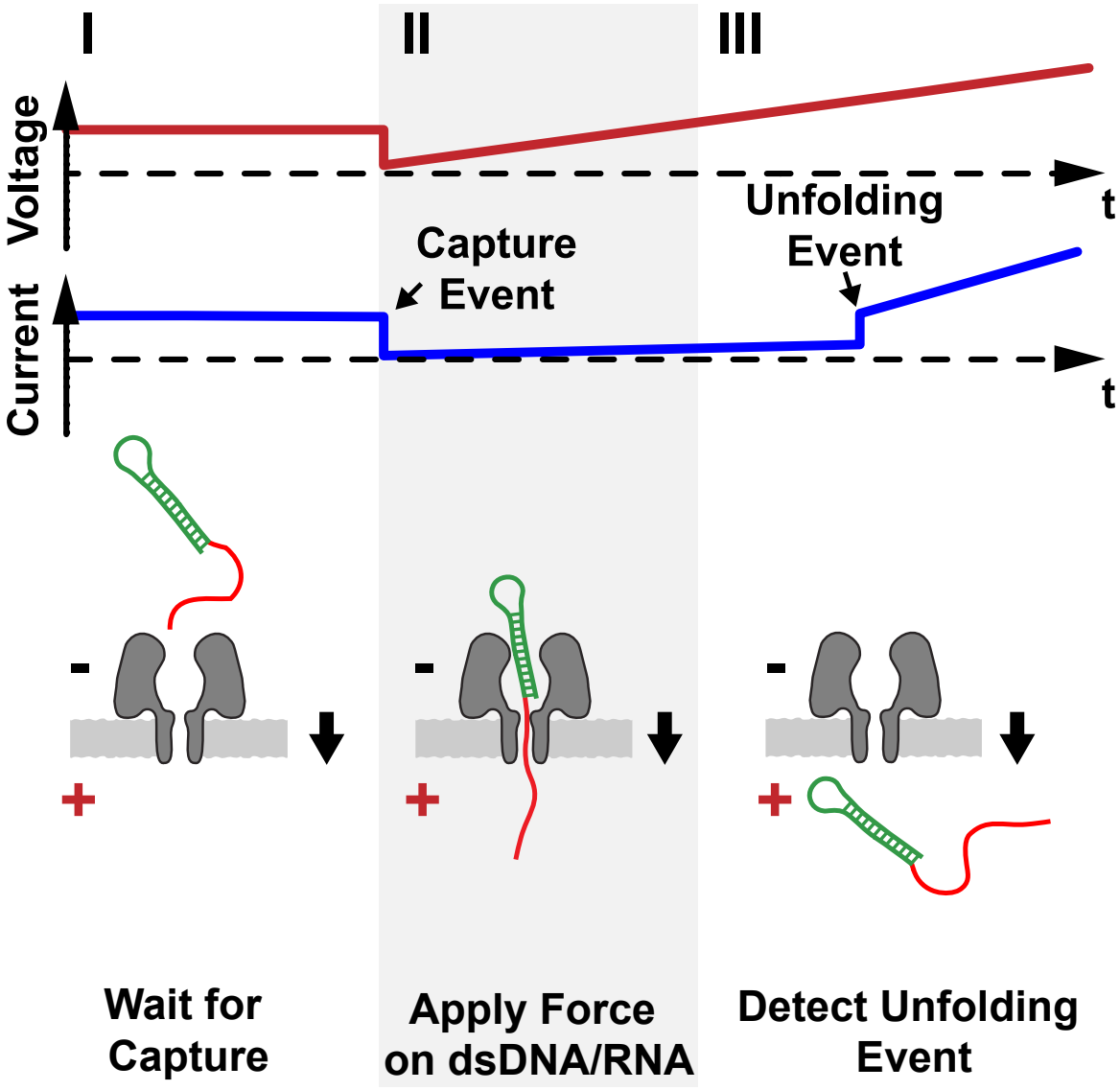

Figure 2.2: Measurement principle for fast electronic trigger in forward direction. I) A potential of 120 mV is applied to capture a DNA/RNA molecule. Upon detection of a capture event, the potential immediately is switched to 50 mV to hold the nucleic acid structure inside the pore and II) A voltage ramp to 250 mV is started to exert an increasing force on the complex. III) When the secondary structure unfolds, the DNA/RNA molecule escapes from the pore and a sudden increase in the current signal is observed.

To minimize the geometrical and interaction effects due to the vestibule of αHL experiments are preferentially performed in backward direction. Because the capture rate is much lower for backward than for forward direction an anchor technique was introduced.

2.1.4 "Anchor technique"

The measurement principle for anchor technique performed on the ATP aptamer is depicted in Figure 2.3. Translocation experiments were performed with DNA constructs of the general structure $5' -$ stopper $-$ spacer $-$ aptamer $-$ thread $- 3'$. By applying a bias voltage of $+120\,\mathrm{mV}$, DNA molecules were initially electrophoretically captured in the pore from the *cis* side with the help of an unstructured $(\mathrm{dT})_{30}$ threading sequence. At this voltage, the ATP aptamer sequence is immediately unfolded and translocated through the pore to the *trans* side (I). To prevent a complete translocation of the DNA construct, a stable hairpin sequence containing 12 G-C basepairs was included at the $5'$ end as a "stopper" sequence, separated from the aptamer by a $(\mathrm{dT})_{50}$ spacer. After detection of a successful capture event by a reduction in the trans-pore current, the DNA construct was held inside the pore at a low voltage (50 mV) to allow reformation of the aptamer structure and target binding on the *trans* side (II). Subsequently, the voltage was ramped linearly from 50 mV to -200 mV (III). Unfolding and escape of the aptamer structure to the *cis* side was then observed as an abrupt increase in trans-pore current, and the corresponding unfolding voltage was recorded. As in this direction the stability of the aptamer structure is not influenced by the vestibule on the *cis*-side of the nanopore, kinetic and stability data can be obtained that are better comparable to those determined in free-solution studies. This is exemplified by the fact that our experiments with the ATP aptamer yield a K_d value in the same range as obtained with other methods.

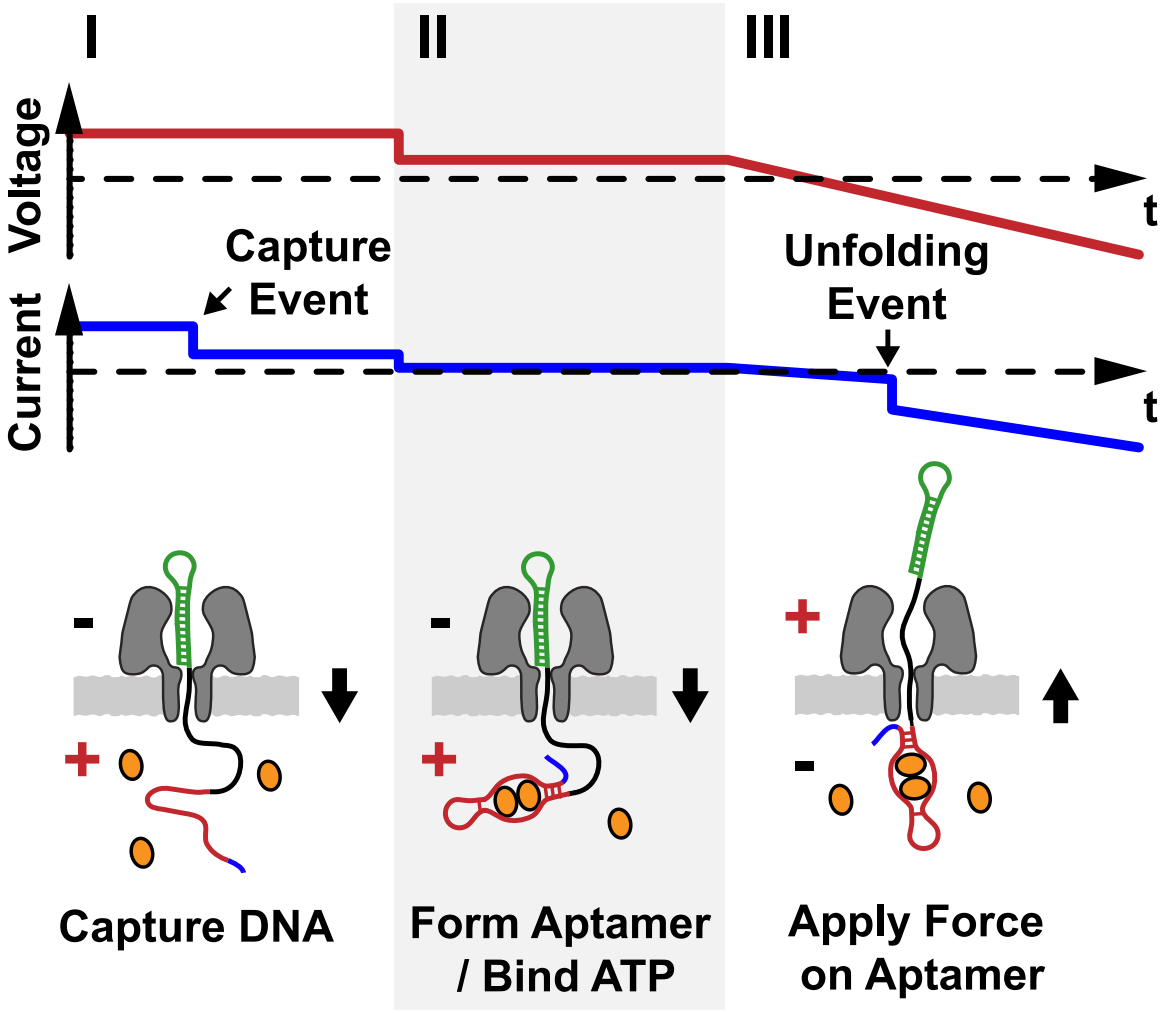

Figure 2.3: Measurement principle for anchor technique. I) A potential of 120 mV is applied to capture a DNA molecule with an aptamer structure on its 3′ end. While the aptamer structure is unfolded upon capture, a stable hairpin at the 5′ end prevents the DNA from traversing the pore. II) The DNA is held inside the pore at low bias voltage (50 mV) to allow reforming of the aptamer and target binding on the *trans* side. III) A voltage ramp to -200 mV is applied. When the aptamer structure unfolds, the DNA molecule escapes from the pore and a sudden increase in the current signal is observed. The corresponding unfolding voltage is recorded.

2.1.5 Synthetic nanopores-electrical measurements

Synthetic DNA channels are characterized using DIB and Orbit 16 set-ups. Solvent conditions used for translocation experiments through synthetic nanopores were:

- 1 M KCl, 10 mM Tris and 1 mM EDTA pH 8 for LB experiments
- 1 M KCl, 5 mM $MgCl_2$, for pin, wheel and T pores dsDNA (527) experiments
- 2 M KCl, 5 mM $MgCl_2$, 10 mM Tris and 1 mM EDTA pH 8 for T pore dsDNA (115) and ssDNA (140)

HPLC purified oligonucleotides for translocation studies (biomers, Ulm, Germany) were dissolved in 10 mM Tris, 1 mM EDTA solution at pH 8. The DNA solution was introduced to the *cis* side of the pore. DNA sequences:

- Hairpin: 5′-$(dT)_6$-ATCTACATATTTTTTTTTTATGTAGAT-$(dT)_{50}$-3′
- Q-T60: 5′-GGTTGGTGTGGTTGG-$(dT)_{60}$-3′
- Q-T125: 5′-GGTTGGTGTGGTTGG-$(dT)_{125}$-3′
- dsDNA (527 bp): 5′-ATACCATGGATATGGGCGGCCACGGCGTGGGTGTACCAGGAGTAGGAGTA
  CAGGAGTAGGAGTACCAGGAGTAGGAGTACCAGGAGTAGGAGTAGCAGGAGTGCCGGGCGTGGGTGTAC
  CAGGAGTAGGAGTACCAGGAGTAGGAGTACCAGGAGTAGGAGTACCAGGAGTAGGAGTAGCAGGAGTGC
  CGGGCGTGGGTGTACCAGGAGTAGGAGTACCAGGAGTAGGAGTACCAGGAGTAGGAGTACCAGGAGTAG
  GAGTAGCAGGAGTGCCGGGCGTGGGTGTACCAGGAGTAGGAGTACCAGGAGTAGGAGTACCAGGAGTAG
  GAGTACCAGGAGTAGGAGTAGCAGGAGTGCCGGGCGTGGGTGTACCAGGAGTAGGAGTACCAGGAGTAG
  GAGTACCAGGAGTAGGAGTACCAGGAGTAGGAGTAGCAGGAGTGCCGGGCGTGGGTGTACCAGGAGTAG
  GAGTACCAGGAGTAGGAGTACCAGGAGTAGGAGTACCAGGAGTAGGAGTAGCAGGAGTGCCG-3′
- ssDNA (140 nt): 5′-$(dT)_{68}$-CCGG-$(dT)_{68}$-3′
- dsDNA (115 bp): 5′-ATAATACGACTCACTATAGGGCGCCGCGAAAACGCGGCGCCCAAAAAAAA
  AAAAAAAAAAAAAAAAAAAAAAGGATCCCGACTGGCGAGAGCCAGGTAACGAATGGATCCAAAAA-3′

A cut-off frequency of 3 kHz was used for the built-in Bessel filter of the Tecella amplifier (Orbit set-up), but in fact the slow frequency response of the 16 channel amplifier board limited the bandwidth considerably (0.5 - 1.7 kHz) in our experiments. For some experiments a single cavity was attached to a HEKA amplifier were the electrical current was digitalized at 200 kHz and a 10 kHz Bessel filter was applied. Before current blockade analysis an additional median filter was applied, averaging over the previous 20 points.

2.2 Self-assembly and purification of DNA-based membrane channels

Structures were designed using caDNAno v.02 [43]. DNA scaffold strands derived from the genome of bacteriophage M13 were prepared recombinantly as previously described [42]. Staple oligonucleotide strands were prepared by solid-phase chemical synthesis (Eurofins MWG, Ebersberg, Germany, HPSF purification). Cholesterol and tocopherol modified oligonucleotides were synthesized using standard phosphoramidite chemistry, HPLC purified, and quality checked by mass spectrometry by biomers (Ulm, Germany). For anchoring the DNA nanopores into lipid membranes, the pores are designed to have DNA handles (all having the same sequence, 5′-TAACAGGATTAGCAGAGCGAGG-3′) at specific positions, which are sequence-complementary to appropriately functionalized adaptor molecules (5′-CCTCGCTCT-GCTAATCCTGTTA-3′). The positions are distributed across the structure to avoid hydrophobic interactions between neighboring anchors (see Figure4.2). Production of DNA channel structures was accomplished in one-pot reactions by mixing 50 nM scaffold strands with 100 nM to 150 nM of oligonucleotide staple strands in a buffer including 5 mM TRIS, 1 mM EDTA, 20 mM $MgCl_2$, 5 mM NaCl (pH 8) [42, 33]. The reaction mixtures were annealed in a TEDRAD (MJ Research, now Biorad) thermal cyling device starting with 65 °C for 15 min, followed by a thermal ramp from 60 °C to 46 °C, decreasing temperature 1 °C per 60 min. Hydrophobic modified DNA pores were produced by incubating the fully folded pores with hydrophobic- modified strands. Tocopherol and cholesterol-modified oligonucleotides were heated to 60 °C for 45 minutes to avoid aggregation. Functionalized pores were created by incubation of the pores with modified DNA strands for 45 minutes. After hybridization with the adaptor sequence, unbound staples are removed by filter purification as described. 50 µL of the reaction products were mixed with 450 µL of buffer containing 5 mM Tris, 1 mM EDTA, 5 mM $MgCl_2$, 5 mM NaCl and spin filtered with a 100 kDa Amicon filter (Millipore) at 2000 rcf for 30 min. The filtration was repeated 5 additional times. After purification the origami structures were stored at room temperature.

2.3 Lipid vesicles

2.3.1 Small and large unilamellar vesicles

POPC lipids were dissolved in chloroform to a concentration of 5 mg/ml. A lipid film was formed by evaporating 1 ml of POPC solution in a 5 ml round bottom flask, using a rotational evaporator. The solvent traces are totally removed by placing the lipid film overnight under vacuum.

2 ml of a 1 M aqueous KCl solution was added on the film, the suspension is vortex, at room temperature or at a temperature higher than the transition state of the used lipids. After this step MLV (multi lamellar vesicles) are formed, in order to form small unilamellar vesicles the solution was sonicated with a tip sonicator (Bandelin Sonoplus mini20) that was introduced directly in the sample. The sample is sonicated for ca. 5 minutes at 8 W, until the solution starts to become transparent. The mean diameter of such vesicles is below 50 nm. The metallic contaminations from the tip are removed by centrifuging the sample 1500 rcf for 5 min. Another approach is taken for the formation of LUVs, the sample is going through several freeze-thawing cycles, between a liquid nitrogen bath and a room temperature bath. The resulting solution should contain a large distribution of unilamellar vesicles. In order to obtained a homogenical size distribution the sample is extruded through a membrane. Depending on the pore size, vesicles between 50 and 200 nm are formed. The solution was shock frozen with liquid nitrogen and kept at -80 °C until usage.

2.3.2 Giant unilamellar vesicles

Giant liposomes can spontaneously form by a swelling process where a dried lipid film is rehydrated. In order to have a better control over the size, shape and time of swelling other strategies were developed. Electroformation or electroswelling starts from a dry lipid film on Indium-Tin-Oxide (ITO) coated glass slides or platinum wires that are used as electrodes for an oscillating elecrtic field. This technique is restricted to salt free solutions, therefore cannot be used for encapsulation of DNA origami structures inside vesicles.

An alternative technique is the inverted emulsion method [36]. The advantage of this technique over the electroswelling is that the inner and outer solution and the lipid composition of the inner and outer leaflet can be controlled independently. Vesicles can be formed at physiological conditions. An uniform lipid film containing 90% Egg PC (L-α-lysophosphatidylcholine) or POPC lipids and 10% biotinylated DOPE (1,2-dioleoyl-sn-glycero-3-phosphoethanolamine-N-(biotinyl)) was created using a rotary evaporator.

The lipid film was dissolved in mineral oil by sonication and vortexing at 80 °C to the final concentration of 5 mg/ml, this step was repeated until the film dissolves completely. In order to disperse the lipids completely the mixture is sonicated for 90 min at 60 °C and a power of 30 W. Directly after sonication the solution was vortexed cooled at room temperature and kept overnight. In order to form the GUVs, 20 µL of the solution to be encapsulated inside the vesicles (the internal solution (IS), containing 400 mM sucrose) was vortexed for 30 s with 200 µl lipid-oil mixture that was preliminary cooled on ice for 15 min, which resulted in the formation of droplets surrounded by a lipid monolayer. Next, 150 µl of the emulsion was carefully layered on top of 1 ml external solution and incubated on ice for 2 h to 3 h. The external solution (ES) had the same osmolarity as the internal solution to ensure stable GUV formation, but contained 400 mM glucose. The compositions of the solutions are chosen in such a way that the vesicles are heavier than their surroundings, which assists in sinking of the GUVs in the ibidi observation chambers. Subsequently, the monolayer droplets are pushed through the IS-ES interface by centrifugating the tube at 12 000 rcf for 30 min at 4 °C.

After this step the liquid from the surface is removed till 500 µL of liposome solution remain at the bottom. When origami pores were added externally to the vesicles, the external and internal solution were adjusted to a final salt concentration of 500 mM KCl to preserve the structure of the origami pores. Encapsulation of DNA origami structures was carried out by replacing the IS containing only sucrose to a mixture of DNA origami and sucrose, while the final salt concentration of the internal solution was maintained at 500 mM KCl. The external solution was supplemented with salt and glucose to equalize the osmolarity on both sides of the vesicle membrane. Encapsulation of a dextran (MW 500000)-fluorescein conjugate (Sigma Aldrich) was carried out similarly.

2.4 Dye influx assay for probing spontaneous channels membrane-incorporation

The dye influx assay was carried out by immobilizing GUVs containing 10% biotinylated lipids on a BSA-biotin-streptavidin coated ibidi chamber. This ensures easier observation of the vesicles using the confocal microscope without compromising the stability of the vesicles. Stable giant unilamellar vesicles are made using the inverted emulsion techniquecite [36]. The advantage of these techniques is that a wide range of solutions can be used. One criterion is that the encapsulated and external have the same osmolarity in order to minimize the osmotic pressure imbalance across the membrane. By contrast, electroformation of GUV's has limitations on the salt conditions used for the internal solutions and cannot be used for encapsulation of DNA origami structures inside of vesicles.

High monovalent salt concentrations were used to maintain the stability of the DNA origami structures, but divalent ions were avoided as they strongly reduced the stability of the GUVs. Origami structures were added externally (see Figure2.4 a) or encapsulated (see Figure2.4 b) in the vesicles. The modifications on the origami structure enabling enhanced interaction with the lipid bilayer were added to the origami structure during purification. Alternatively, to avoid aggregation of the DNA channels in solution, DNA lipid conjugates were first incorporated in the lipid membranes, followed by the addition of unmodified DNA channels to the vesicle suspension. The dye influx assay was carried out at room temperature. Influx of dye was observed using a confocal microscope (Leica SP5 II).

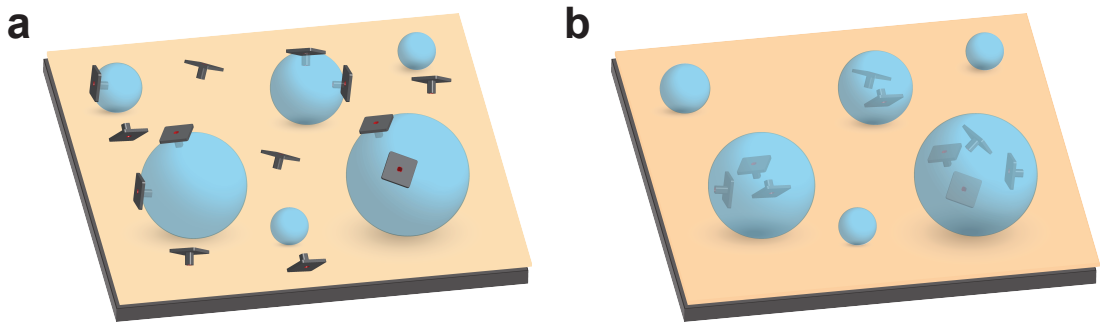

Figure 2.4: Dye influx experiments. Biotinylated GUV's are immobilized on biotin-streptavidin coated surface a) Channel solution is added externally. b) Channels are encapsulated into vesicles

2.5 TEM evidence for DNA channels membrane interaction

Small unilamellar vesicles (SUVs) were used in Transmission Electron Microscope (TEM) imaging to confirm membrane interaction of the pores. Images of DNA nanostructures were recorded using a standard negative staining protocol. Vesicles and nanostructures were incubated in solution and this mixture was applied to the TEM grids, followed by negative staining. Fully intact SUVs are not filled with stain and appear white against the background, whereas DNA pores generate higher contrast.

2.6 Data analysis

2.6.1 Dwell-time analysis of closing events

The detection of translocation events is performed using a custom-written Matlab routine (peak fit analysis). The data acquired using the Heka amplifier were median-filtered to further reduce noise. Each point of a filtered trace equals the median over the 20 previous points of the original trace, hence the maximum resolution is reduced to values higher than 50 µs. The median filter affects the heights of the peaks, but conserves the durations of the events.

The program allowed for a moving baseline calculating the actual value of the baseline at a user defined data point window (1000 points= 5 ms) before the event. This helped in taking into account the fluctuations in the baseline arising during the experiment. The data in form of traces was first sorted into domains. Each domain was assigned a sign indicating, if it was recorded at positive or negative external voltages, further analysis was done on positive sign domains only. The baseline value was determined using a moving window filter for which the window size was user defined (100 data points) and within this window a median value was determined. The start of the event was identified when the difference of the baseline (700 points ahead of the event) and the trace reaches a value lower than the user defined threshold ($\text{threshold}_{on} = 10 \cdot \text{stdev}$). The end point of the event was determined as the point where the difference between the baseline and the trace was more than the user defined off threshold ($\text{threshold}_{off} = 2 \cdot \text{stdev}$)). The manually chosen standard deviation increases with voltage. As measurements of the background signal indicate a roughly linear increase of noise with increasing voltage, the standard deviation is also increased with voltage. The difference between upper and lower baseline defines the depth of the event ΔI. The lower baseline or the baseline of the event was calculated using the minimum value of either a user defined quantile or a mean of the entire event. A user defined ratio between the upper and the lower baseline was then used to determine the last data point below this ratio to mark the real end of the event, providing the right dwell-time. Some DNA translocation experiments performed on DNA channels were recorded on the Tecella amplifier. To determine the amplitude of measured current blockades reliably, rising edge and falling edge of all peaks were fitted with single exponentials as described in Ref. [9].

The translocation times and velocities were extracted by regression analysis of the dwell-time histograms based on a 1D drift diffusion model [61], which has been previously applied to the nanopore translocation [32]. According to the model the probability $P(t)$ that a translocation event has length t is given by:

$$P(t) = (b/(4\pi D t^3)^{1/2}) \times exp\left(-\frac{(b-vt)^2}{4Dt}\right), \tag{2.1}$$

Here, the parameter b is the sum of the length of the pore and the contour length of the translocating DNA molecules, D is the diffusion coefficient for 1D diffusion of DNA through the pore (or the pore along the molecule) and v is the drift velocity. Diffusion coefficient D and velocity v are obtained from regression analysis of our data. The time for which this translocation time distribution reaches its maximum (the mode) is defined as the translocation time. The dwell-time histogram feature logarithmically spaced bin widths and were fitted with a single exponential ($p(t) = exp(-t/\tau)$) with the time constant τ being the only fit parameter. For measurements on hairpin translocation, it was necessary to introduce an amplitude scaling factor to obtain satisfying fits.

2.6.2 Peak analysis using Hidden Markov model

Hidden Markov modeling (HMM) can be applied to extract single channel kinetics at signal-to-noise ratios that are too low for conventional analysis. The model contains two terms: an amplitude term that is used to estimate the probability that a given data point belongs to a given current level (emission probabilities $E_i(x)$), and a transition probability term that is used to estimate the probability for a transition (T_{ij}) from a state i to a state j. In our case the model optimizes the emission probabilities itself. At start the emission probabilities are initialized with Gaussian distributions centered about each current level. The transition probability matrix T_{ij} is chosen as probability per time step and normalized such that $\sum_{j=0}^{N-1} T_{ij} = 1$. For the analysis of current blockades, T_{ij} can be assumed as time-independent. Hidden Markov classification of states is done using the Viterbi algorithm. Which calculates the most likely sequence of states that produces the current trace, given the model parameters T_{ij} and $E_i(x)$.

The current traces were median-filtered, each point of a filtered trace equals the median over the 100 previous points. In our traces a three-state system with states I, II and III are detected. Where, there is a fast exchange between states I and II, and III and II. States I and III are short-lived. There are no transitions between the states I and and III (see Figure 2.5).

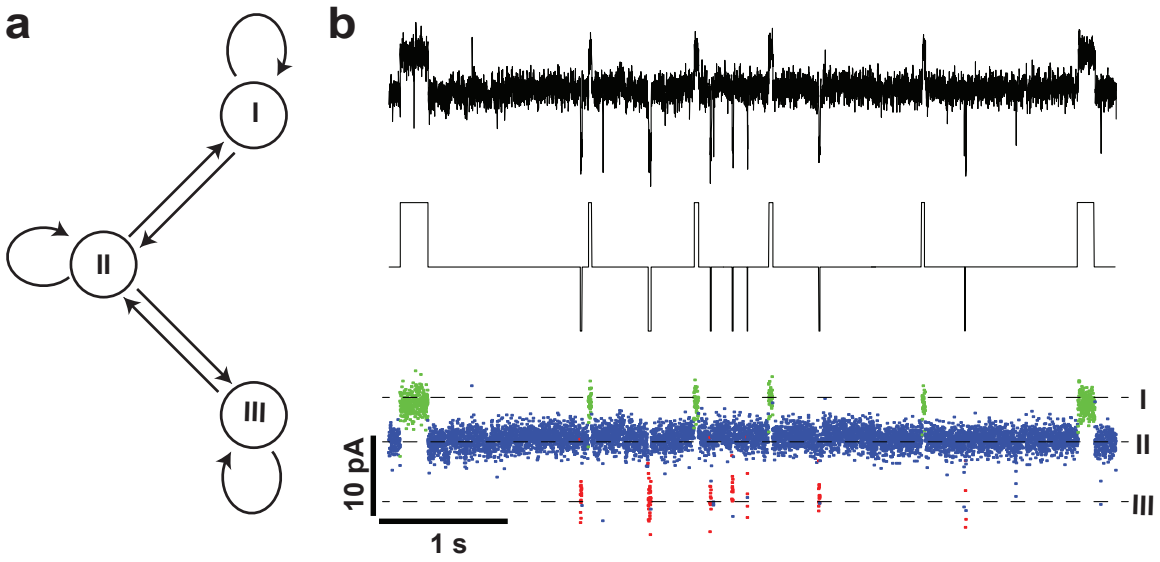

Figure 2.5: Hidden Markov model on current traces with three levels. a) Connectivity and kinetics of the three states model. Transitions between state I and state III were not allowed. b) Example current traces. c) Detected events. d) Classified data points.

To account for missed and wrongly detected events the normalized integrated histogram of the dwell times was calculated and fitted with a single exponential function.

$$f(t) = \frac{exp(-t/\tau) - exp(t_{min}/\tau)}{exp(-t_{max}/\tau) - exp(t_{min}/\tau)} \tag{2.2}$$

where t_{min} and t_{max} are the time of the shortest and longest detected events, respectively.

2.6.3 Nanopore force spectrosopy

Hairpin unfolding experiments was considered as two step process, the DNA molecule is folded inside the nanopore and the DNA escapes the nanopore (see Figure2.6 a). During the transition the molecule should cross an energy barrier ΔG_0, under the application of external forces the barrier height decreases ΔG, $G(x) = G_0(x) - Fx$ (see Figure2.6 b).

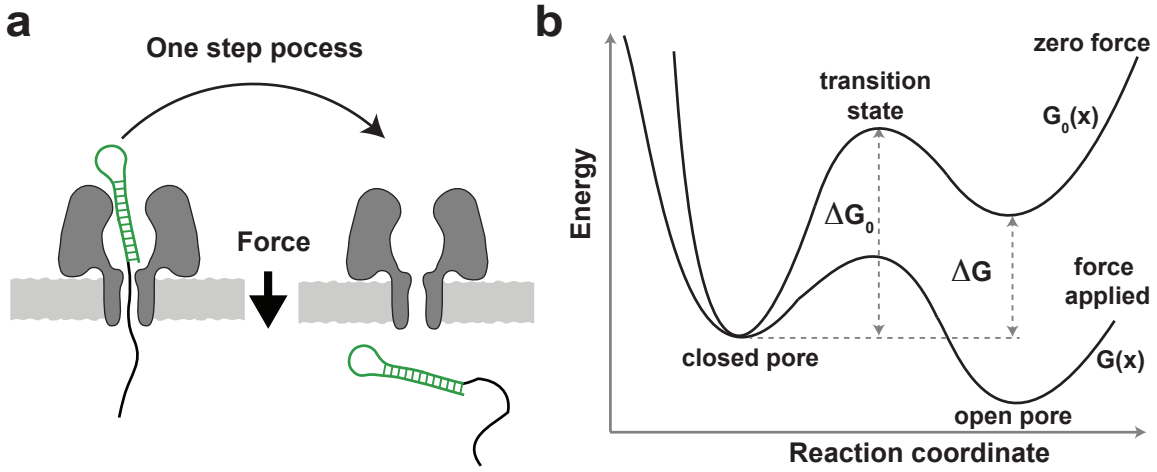

Figure 2.6: Energy landscape for a hairpin unzipping and translocation. a) Two steps process of a DNA molecule catching and translocation, schematic representation. b) Energy barrier (ΔG_0) that a hairpin should cross for translocating through a nanopore. Decreased energy barrier height, ΔG, under external force. Figure inspired by Ref. [44].

The escape rate for a single-well free energy surface is $k_{off} = A \times exp(-\frac{G_0}{k_B T})$ in this case the molecule can escape due to thermal fluctuations. Under external force the escape rate is:

$$k_{off} = A \times exp(-\frac{G_0 - Fx}{k_B T}) \tag{2.3}$$

The force for nanopore experiments is proportional to the applied voltage:

$$k_{off} = A \times exp(-\frac{G_0 - Q_{eff} V}{k_B T}) = k_0 \times exp(-\frac{V}{V_\beta}) \tag{2.4}$$

where $k_0 = A \times exp(-\frac{G_0}{k_B T})$, $V_\beta = k_B T / Q_{eff}$ and Q_{eff} is the effective charge. The translocation dwell-time is given by

$$\tau(V) = \frac{1}{k_{off}(V)} = \tau_0 \cdot e^{-V/V_\beta} \tag{2.5}$$

where τ_0 is the intrinsic (zero voltage) lifetime of the structure. The parameter V_β characterizes the voltage dependence of the unfolding process and depends on the effective charge of the molecule on which the electric can exert a force, but also on details of the unfolding landscape [107, 46].

The distribution of the unfolding voltages for constant loading ramp experiments given by:

$$p_i(V) = \frac{1}{\tau_{0i}\dot{V}} \exp\left[\frac{V}{V_{\beta i}} - \frac{V_{\beta i}}{\tau_{0i}\dot{V}}\left(e^{V/V_{\beta i}} - 1\right)\right] \tag{2.6}$$

The critical unzipping voltage, V_C, is defined by the maximum of this distribution, which is:

$$V_C = V_\beta ln(\frac{\tau_0 \dot{V}}{V_\beta}) \tag{2.7}$$

This expression was derived by Mathe et al. [107] for unfolding of DNA structures in voltage ramp experiments with a constant ramp speed $\dot{V}$.

We also analyzed the data in a different way by calculating the lifetime as a function of voltage $\tau(V)$ using the conversion formula [128, 45]

$$\langle\tau\rangle(V) = \frac{\int_V^\infty p(V'|\dot{V})dV'}{\dot{V}p(V|\dot{V})} \tag{2.8}$$

This expression essentially is the result of a variable transformation and does not rely on a specific assumption for the functional form of $\tau(V)$. Hence, in contrast to fits by Eq. 2.6, this procedure results in model-independent estimates of $\tau(V)$ from the data.

Eq. 2.8 predicts that data obtained at different loading rates must collapse onto a single master curve that yields the voltage dependence of $\tau(V)$ over a range of voltages that may be wider than the range accessible in constant-force measurements. Voltage dependent lifetime curves (see Figure 2.7) recorded at different voltage ramps for the aptamer-ATP complex confirmed that the experiments were performed in the quasi-adiabatic limit.

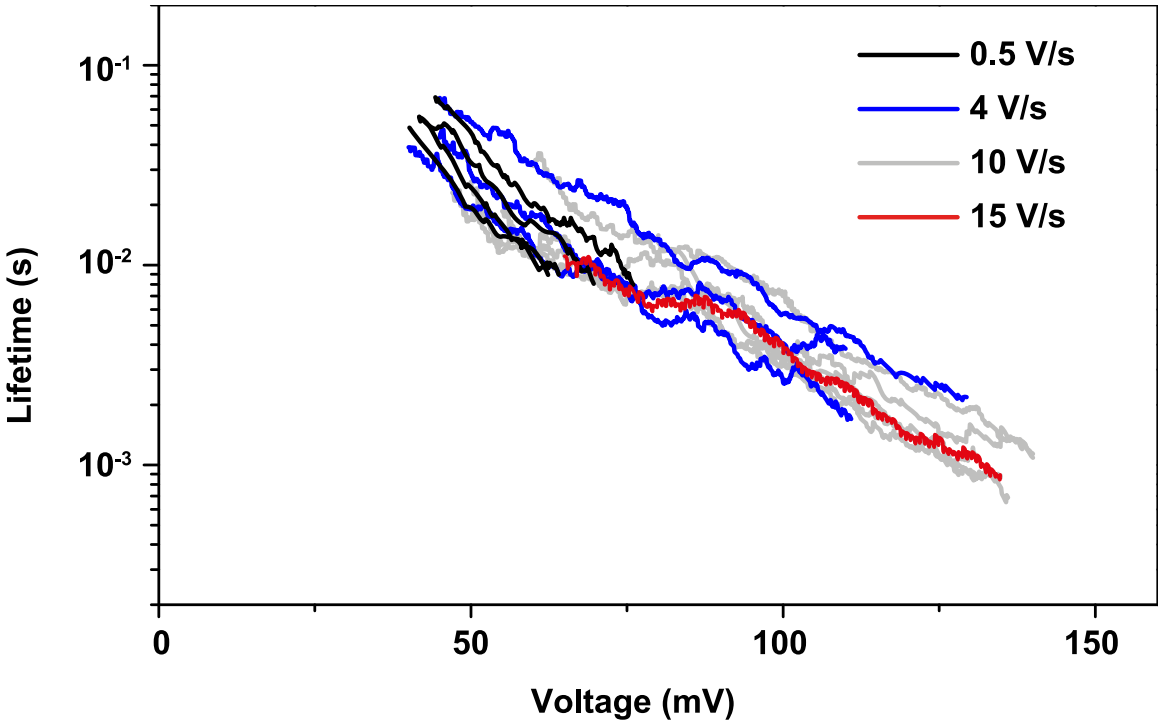

Figure 2.7: Voltage dependent lifetime of ATP aptamer - ligand complexes obtained at different loading rates. Each line represents one individual measurement. An ATP concentration of 1 mM was used.

2.6.4 Dissociation constant determination of aptamer - target complex

In order to determine the fraction of bound aptamer - target complexes

$$\theta = \frac{[\text{aptamer complexes}]}{[\text{total amount of aptamers}]}$$

the distribution of unfolding voltages were fitted:

$$p(V) = (1-\theta)p_0(V) + \theta p_1(V), \tag{2.9}$$

where $p_0(V)$ represents the unfolding voltage distribution for the free aptamers, and $p_1(V)$ is the distribution for the bound complexes.

The bound fraction θ is accurately fit by a simple binding curve of the form and the K_d is determined.

$$\theta = \frac{[\text{ATP}]}{[\text{ATP}] + K_d} \tag{2.10}$$

2.6.5 Electrical field mapping using Comsol simulation

A qualitative study of how the origami structure's intrinsic electrical conductivity impacts the distribution of the potential and the channel conductance was performed by means of a finite element simulation using Comsol Multiphysics to solve Poisson's equation. To this end the DNA channel was approximated by two cylinders with an outer diameter of 6.6 nm and a length of 20 nm, which contains a cylindrical channel with a diameter of 2.2 nm in the inside (Figure 4.35 a). The lipid bilayer was modelled as a 4 nm thick layer with zero conductivity. The symmetry axis of the channel was defined as the z axis of the coordinate system. z=0 corresponds to the boundary of the lipid bilayer facing the stem side of the structure. The channel interior and adjacent solution compartments were simulated with KCl solution bulk conductivity (11 S/m). To screen the influence of origami leakiness, the conductivity of the origami structure was varied in the simulation from 10^{-4} S/m (insulating) to 10 S/m. The mesh density ranged from 18 elements/nm^3 (channel interior and surrounding) to 10^{-2} elements/nm^3 (solution compartments).

2.6.6 Dye influx kinetics

In order to quantitate the kinetics of dye influx, we assume that the flux j through a single channel is given by

$$j = D\frac{n_0 - n_i}{L} \tag{2.11}$$

where D is the diffusion coefficient of the dye, L is the effective length of the channel, and n_0, n_i are the dye concentrations outside and inside of the liposome (in units of $1/m^3$). Thus the number of dye molecules N_i inside of the liposome increases as:

$$\dot{N}_i = j\dot{A} = \frac{DA}{L}(n_0 - n_i) \tag{2.12}$$

and therefore the concentration changes according to:

$$\dot{n}_i = \frac{DA}{LV}(n_0 - n_i) =: Mk(n_0 - n_i) \tag{2.13}$$

where V is the volume of the vesicle, M is the number of incorporated pores and we introduced the abbreviation $k := DA/LV$, with a unit of 1/s. Now, assuming that the dye concentration in the solution surrounding the vesicle stays constant, we can solve for the concentration inside:

$$n_i(t) = n_0 - (n_0 - n_i(0)) \times exp(-Mkt) \tag{2.14}$$

If the initial concentration inside is zero, $n_i(0) = 0$, this simplifies to:

$$n_i(t) = n_0(1 - exp(-Mkt)) \tag{2.15}$$

Experimentally obtained time traces typically followed this monoexponential behavior (see Figure 4.10). Using an exponential model for dye influx, we estimated the number of incorporated pores per vesicle. The observed number of incorporated pores for each vesicle is plotted as a function of the surface area, A, of the corresponding vesicles.

3 Force Spectroscopy

3.1 Nanopore force spectroscopy for aptamer-target complex

3.1.1 Aptamer-ATP complexes

Previously the ATP-binding aptamer [77] and the thrombin aptamer [22] were studied using constant voltage nanopore experiments [140, 166, 133]. For the ATP aptamer, ligand-bound and unbound states could be distinguished by their current traces [166]. For the thrombin aptamer, on- and off-rates of the complex as well as its dissociation constant were determined by attaching the aptamer to the vestibule of a mutated αHL channel and detecting current enhancement upon ligand binding [133]. Nanopore dynamic force spectroscopy was employed to analyze aptamer-ligand complex for two DNA aptamers [7] and one RNA aptamer.

The results obtained from nanopore force spectroscopy experiments on the ATP aptamer structure (using strand `ATPapt`) are shown in Figure 3.1. The ATP aptamer is known to bind two ATP molecules in a non-canonical, but stable helix comprised of G:G and G:A base pairs flanked by short Watson-Crick duplexes (**B**) [98]. In the absence of ATP, the secondary structure containing aptamer binding sites (**U**) - with a folding free energy of merely -0.84 kcal/mol as calculated by mfold [172] - is *not* the most stable structure. Alternative structures (**U'**) with other base-pairing patterns - not containing the ATP binding site - are considerably more stable, having a folding free energy of $\Delta G_{fold} = -3.31$ kcal/mol (see Figure 3.1 a). As indicated in Figure 3.1 a, in order to bind ATP, the aptamer has to either unfold and rearrange from more stable structures ("conformational selection") in order to adopt a binding-competent state, or somehow change conformation upon ATP binding, corresponding to an induced fit mechanism.

In the absence of ATP, a single peak in the unfolding voltage histogram is observed (see Figure 3.1 b) centered around a critical unfolding voltage of $V_c = 27$ mV. This is consistent with the unfolding of a very weak DNA secondary structure containing only few base pairs [136]. In the presence of ATP, a second, broader and more stable population appears in the histograms.

At an ATP concentration of 100 µM, 48 ± 10 % (maximum error estimated from repeated experiments) of all detected events belong to the more stable population. With increasing ligand concentration, this population further grows to a fraction of 85 ± 10 % at 1 mM ATP. This population can be attributed to the unfolding of aptamer-ligand complexes. Its relative size consequently corresponds to the fraction θ of bound aptamers. In order to check whether the time after unzipping and translocation of the aptamer (phase II in Figure 2.3) was sufficient to allow for re-folding of the structure and ATP binding, waiting time was varied in a range from 30 ms to 1 s. Our results were identical for these times, suggesting that the structures had sufficiently equilibrated within milliseconds. For our experiments, we typically used a waiting time of 200 ms, which should be sufficient for the lowest ATP concentrations measured here.

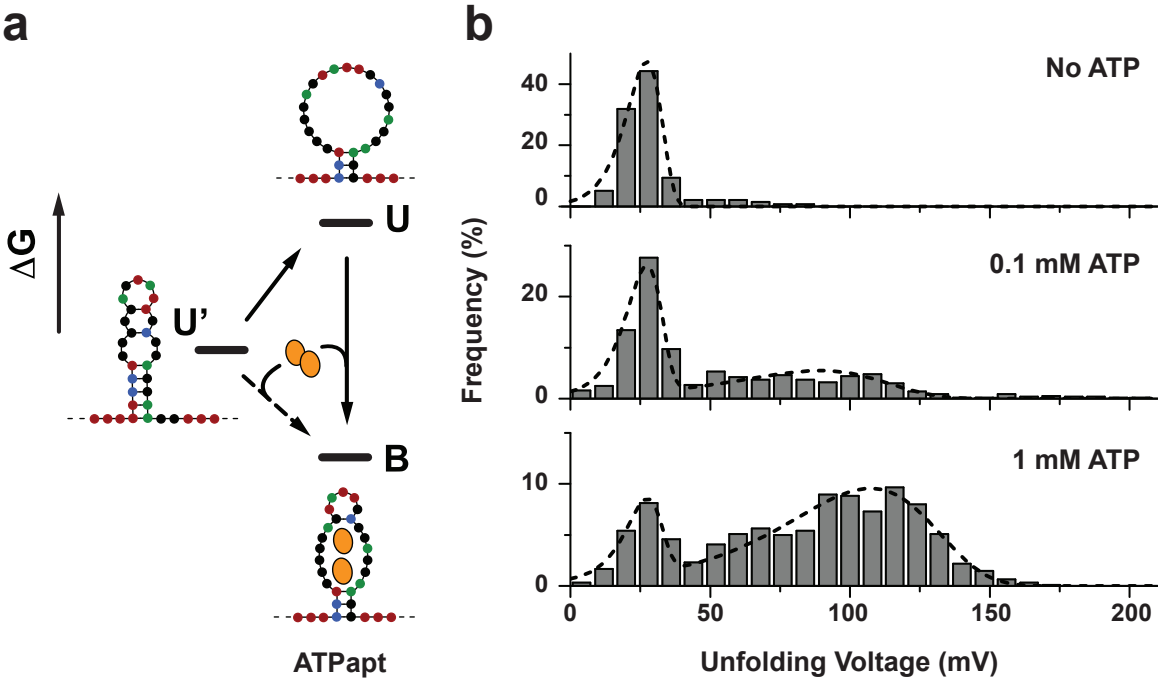

Figure 3.1: ATP aptamer `ATPapt` unfolding at various ATP concentrations a) Binding pathways for the ATP aptamers `ATPapt`. Bases are depicted as circles (A: green, T: red, G: black, C: blue). Black bars indicate free energies of the structures. For `ATPapt`, in order to bind ATP the secondary structure with lowest mean free energy U' either has to unfold and rearrange to form the structure with the ATP-binding pocket U ('conformational selection'), or adopt its conformation upon ATP binding ('induced fit'). b) Unfolding voltage distributions at different ATP concentrations, obtained at a loading rate of 10 V/s with no ATP present, a single population at 27 mV is observed. Upon addition of ATP a second, more stable population appears, which increases with increasing ATP concentration. This population is assigned to aptamer structures with bound ATP targets. Histograms are fitted to Eq. 2.6 (dashed lines) in order to determine the fraction of bound structures.

The parameters $\tau_{0,0}$ and $V_{\beta,0}$ for the unbound population were determined in experiments without aptamer targets and then fixed for the analysis of experiments with added targets. From an average over all measurements with aptamer-target complexes, $V_{\beta,1}$ was then determined to be 26.5 mV. This left $\tau_{0,1}$ and θ as the only remaining fit parameters in Eqns. 2.9 & 2.6 for the evaluation of the various histograms constructed from experiments with aptamer-target complexes. For [ATP]= 25 µM, the bound population was too weak to be fitted accurately with the least squares method, and in this case a maximum likelihood approach was used instead. At [ATP]=5 µM, no bound population was observed.

In the context of subpopulations contained within the unfolding histograms, one has to consider that the aptamer sequence can fold into an ensemble of many different, relatively weak secondary structures.

We therefore sought to deliberately stabilize the aptamer's binding-competent conformation with a minimal modification in sequence: insertion of two adenine bases at the 5′ end

of the aptamer sequence (cf. sequence `ATPapt-mod`) leads to the formation of additional two base-pairs at the bottom of the flanking stem (together with two thymines from the threading sequence). The corresponding secondary structure then is the minimum free energy structure of the sequence with a $\Delta G_{fold} = -3.63$ kcal/mol (see Figure 3.2 a).

For experiments performed at [ATP]= 1 mM and with a waiting time of 200 ms (phase II in Figure 2.3), it was found that the binding fractions θ are very similar for `ATPapt` (85%) and `ATPapt-mod` (89%) (see Figure 3.2 b)

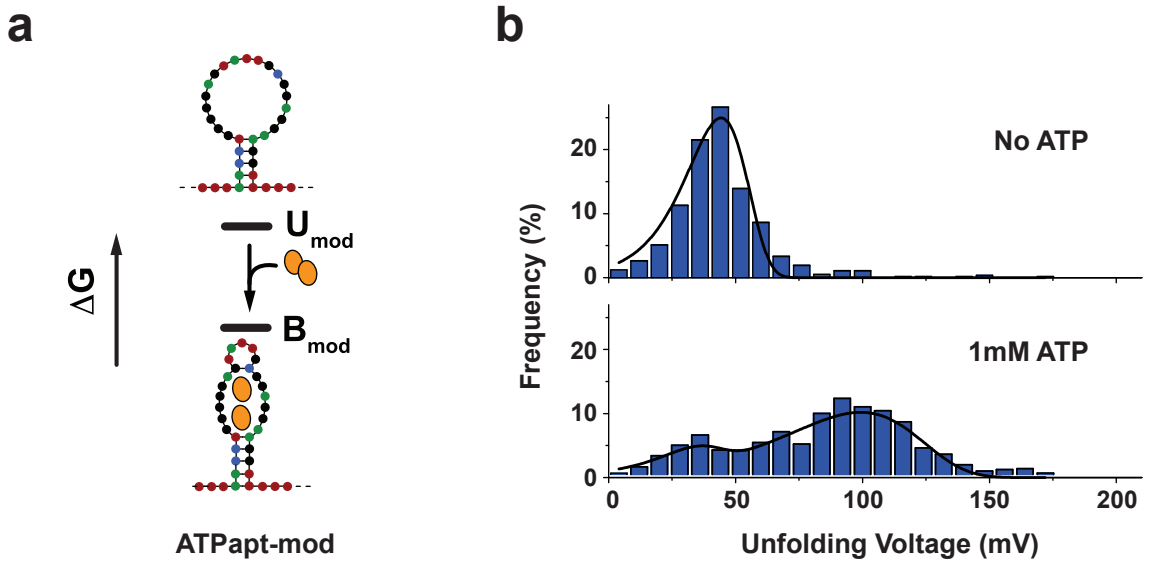

Figure 3.2: Aptamer Tailoring. a) Binding pathway for `ATPapt-mod`, for which the binding-competent state is stabilized with two additional A-T basepairs at its end. b) Unfolding voltage distributions for the modified aptamer structure `ATPapt-mod` with and without addition of ATP at a loading rate of 10 V/s.

As shown in Figure 3.3 a, as a function of ATP concentration, the bound fraction θ is accurately fit by a simple binding curve of the form 2.10. The fit yields a dissociation constant of $K_d = 119 \pm 12$ µM for `ATPapt` and $K_d = 116 \pm 16$ µM for `ATPapt-mod`. The obtained dissociation constants are virtually identical values for both aptamer structures. We tentatively also fitted a Hill curve. The fit resulted in a $K_{0.5}$ equaling the K_d obtained from the "simple fit" with Eq. 2.10, and a Hill coefficient only slightly above 1 indicating only weak cooperativity in binding. In fact, a more detailed binding model with two *independent* binding sites with the same K_d yields Eq. 2.10 as the sum of the fractions of complexes with one *or* two ATP molecules bound. In previous studies, a broad range of K_d values from 6 µM to 2000 µM was found [77, 79, 119, 120, 155, 156, 114, 73, 10, 148], strongly depending on buffer conditions, the labeling strategy used, and other factors such as the presence of competitive binders.

In recent work by Baaske et al. [10], using aptamers labeled with Cy5 a K_d of 60 µM was found in the presence of 0.3 M Na^+ and 5 mM Mg^{2+}, roughly a factor of two lower than our value determined at 1 M monovalent salt. One limiting factor is the diffusive flux j_D of ATP molecules to the aptamer's binding site with size $a \approx 1$nm. This may be estimated as $j_D = 2\pi D a c_{ATP}$, where $D \approx 300$ µm^2/s is the diffusion coefficient of ATP [75], and c_{ATP} is its concentration. For $c_{ATP} = 1$ µM this results in $j_D \approx 1.1 \times 10^3$(molecules)/s or $j_D \approx 1$/ms. This also indicates, however, that for considerably lower target concentrations (e.g., for

experiments with aptamers with lower K_d), waiting times have to be chosen correspondingly longer.

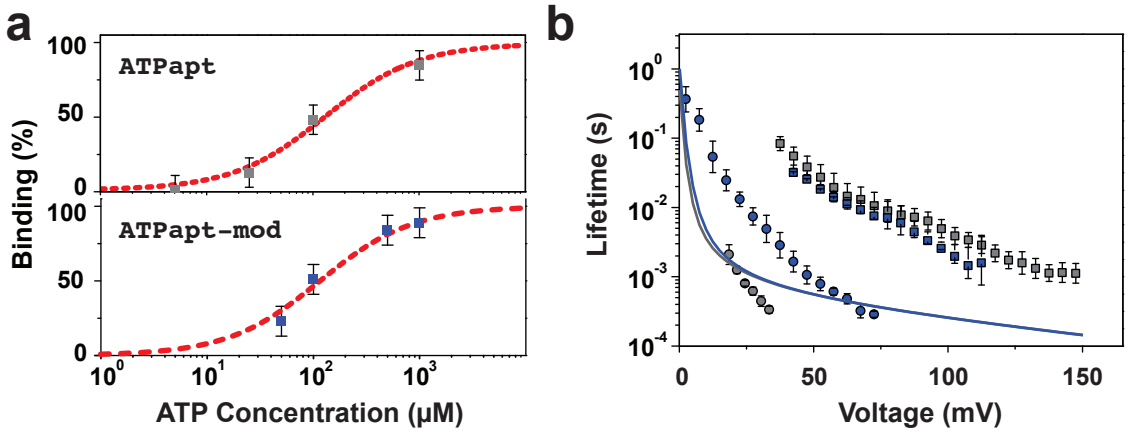

Figure 3.3: Dissociation constant and lifetime comparison for `ATPapt` and `ATPapt-mod`. a) Fraction of bound aptamer structures vs. ATP concentration for `ATPapt` and `ATPapt-mod`. The dashed line represents a fit to the hill equation. The fit yields a dissociation constant of 119 ± 12 µM and 116 ± 16 µM respectively b) Lifetime vs. voltage for modified (blue) and unmodified (grey) aptamers (circles) and aptamer target - structures (squares) determined from measurement data according to Eq. 2.8. Error bars are standard deviations from 2-12 independent measurements.

The voltage dependent unfolding time $\tau(V)$ of the ATP-aptamer complexes is almost identical for both structures over the whole voltage range investigated. This indicates that for unfolding, breaking of the additional two (weak) A-T basepairs of the modified structure is not rate-determining, but rather the unstacking and destabilization of the whole structure accompanied by a release of the ATP molecules.

As expected, this also results in a considerably increased stability of the unbound `ATPapt-mod` in the NFS experiments (cf. Figure 3.3 b).

As the free energy differences of unbound and bound conformations (**U'** and **B** for `ATPapt` and $\mathbf{U}_{mod}$ and $\mathbf{B}_{mod}$ for `ATPapt-mod`) are expected to be quite similar, this finding is consistent with the assumption that the aptamers have equilibrated before the start of the unzipping ramp. Even though `ATPapt` has to change conformation for ATP binding, this step is not rate-limiting under our experimental conditions, which indicates that the relatively weak ATP aptamer structures rapidly change their conformation in the absence of ATP. Using the mesoscopic model previous described in Ref. [136], the lifetime vs voltage behavior is predicted. As observed in Figure 3.3 b the experimental data are not following the estimated data. The less stable structure described in Ref [136] has $\Delta G_{fold} = -1.97$ kcal/-mol two times more stable than the free ATP aptamer. No predictions could be made for the aptamer -ATP-complex.

3.1.2 Binding to ATP vs. ADP and AMP

The ATP aptamer is known to bind different adenosine phosphates with similar affinity [119]. This can be understood by considering the NMR structure of the aptamer-ligand complex determined by Lin et al. [98], where the adenine stacks into the aptamer's binding site,

while the phosphate groups are oriented outwards and do not seem to directly participate in binding.

We therefore performed NFS experiments also in the presence of ADP and AMP to further assess the specificity of the ligand-aptamer interaction (see Figure 3.4). While binding was observed for all three ligand molecules, there was a tendency towards higher affinity for ADP and AMP ligands, as indicated by the higher binding fractions θ at 1 mM. As expected, no binding was observed in a control experiment in the presence of 1 mM CTP (see Figure 3.4 a).

For ADP we determined a θ of 93 ± 10 %, while for AMP no unbound population was observed, suggesting a bound fraction of nearly 100 %. We found dissociation constants of 92 ± 10 μM and 85 ± 14 μM for ADP and AMP, respectively (see Figure 3.4 c).

At the same time, the stability of the bound complexes - as measured by the critical unfolding voltage - seemed to be slightly higher for ATP than for ADP or AMP, respectively (see Figure 3.4 a). As described in the Methods Sec. 2.6.3, the voltage-dependent lifetime of all three aptamer-target complexes was calculated from the distribution of unfolding voltages according to Eq. 2.8, taking into account only events assigned to the bound aptamer population. We observe slightly lower lifetimes for AMP and ADP complexes compared to those with ATP. We speculate that for the smaller and less charged AMP and ADP (with a nominal charge of $-2e$ and $-3e$ vs. $-4e$ for ATP), the electrostatic energy barrier for binding to the aptamer is lower and hence their binding on-rate k_{on} is higher than for ATP, resulting in an overall smaller K_d of the corresponding aptamer-ligand complexes. The electrostatic barrier is expected to be affected by the presence of Mg^{2+}, which is known to strongly interact with ATP. This is consistent with the fact that Baaske et al. [10] found a lower value for the K_d of ATP in a Mg^{2+} containing buffer, while their value for the less charged AMP coincides almost exactly with ours. It is interesting to note that the voltage dependence of the lifetime of aptamer-ligand complexes is much weaker than for ordinary DNA secondary structures such as DNA hairpins [136]. In the simple model with an exponential voltage dependence of $\tau(V)$ one would expect $\ln \tau(V) = \ln \tau_0 - V/V_\beta$. Hence, in this model the slope of the $\tau(V)$ graphs in Figure 3.4 d represents the parameter $1/V_\beta$. This may indicate that the effective charge and/or unfolding landscape of aptamer ligand complexes considerably differs from those of hairpin structures.

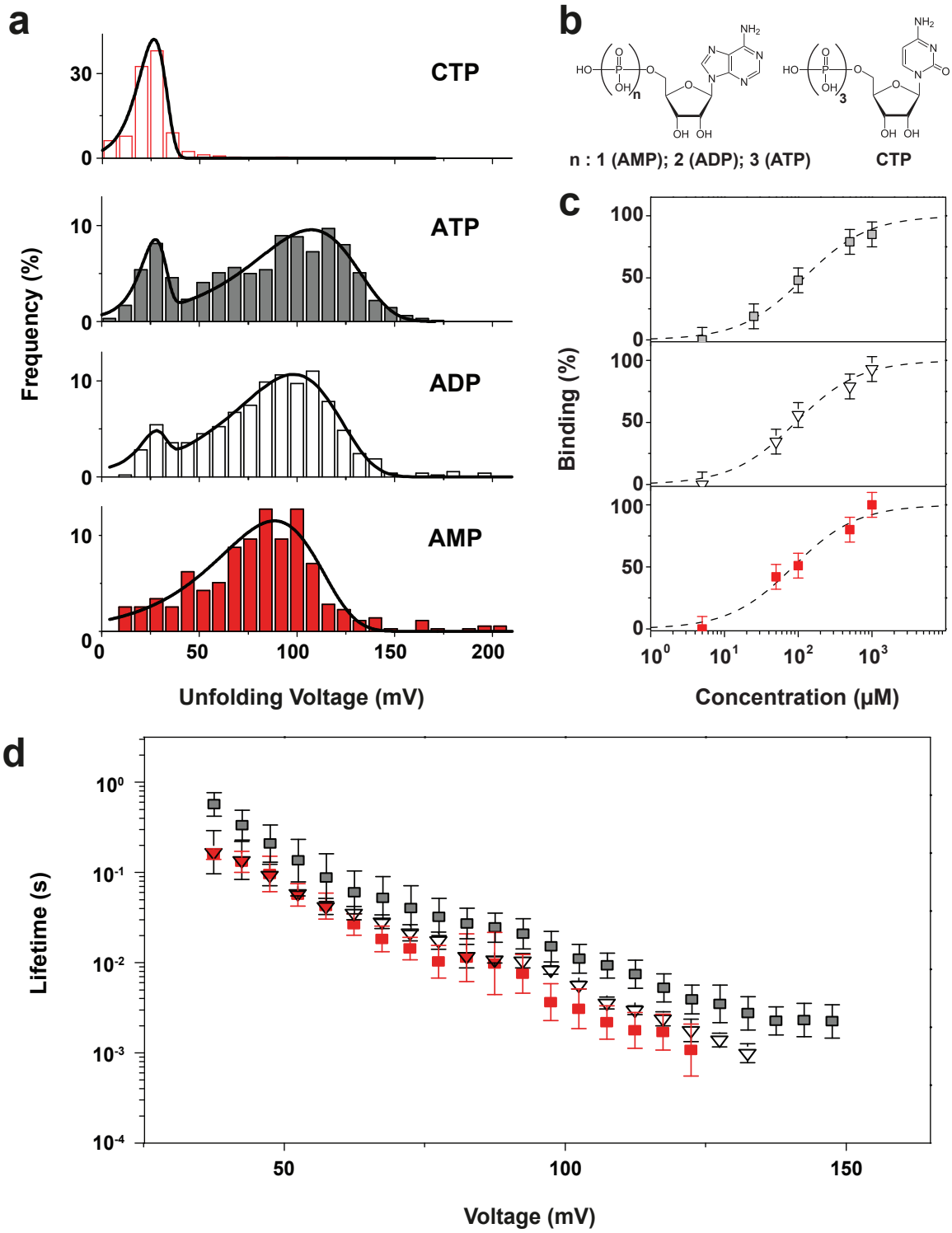

Figure 3.4: Aptamer Target Specificity. a) Unfolding voltage distributions for 1mM cytosine triphosphate(red) and adenosine mono- (red filled), di- (white) and tri-phosphate (grey) at a loading rate of 10 V/s. Solid lines correspond to fits using Eq. 2.6. b) AMP, ADP, ATP and CTP structures. c) Fraction of bound aptamer structures vs. target concentration for ATP (grey squares), ADP (open triangles) and AMP (red squares). The dashed lines show fits to Eq. 2.10. d) Voltage dependent lifetime of aptamer - target complexes. Error bars are standard deviations from 12, 4 and 6 independent measurements for ATP, ADP and AMP, respectively.

An alternative interpretation is that the unfolding histograms contain unresolved subpopulations. In fact, the derivation of the conversion formula (Eq. 2.8) rests on the basic assumption that the unfolding events studied are caused by only a single molecular population and can be described as a first order process [44, 46]. In the case of the ATP aptamer, it is likely that the unfolding histograms contain contributions from aptamers with only one of the two binding sites occupied as well as from the fully bound complex. A superposition of these contributions can result in an artificial flattening of the $\tau(V)$ dependence.

3.1.3 Nanopore force spectroscopy with the thrombin aptamer

Nanopore force spectroscopy was also employ to investigate the binding of the aptamer for human α-thrombin [22]. The stability of the thrombin binding aptamer leads to a variety of experimental problems, the hairpin stopper technique used for the ATP aptamer cannot be applied here. Therefore, experiments were performed using a $(dT)_{50}$-capture sequence attached to the $5'$ end of the aptamer (see Figure 2.2). After capture of an aptamer structure at 120 mV bias voltage, a fast electronic trigger circuit immediately reduced the voltage to 50 mV, followed by a voltage ramp that unfolded the aptamer on the *cis* side.

The stability of the G-quadruplex forming aptamer structure was initially characterized as a function of $[K^+]$, maintaining the overall ionic strength at 1 M by adding NaCl. Thus, only the K^+ binding form may be observed in our present studies which where carried out at 37 °C. The K^+ concentration was varied from 1 M, 100 mM and 10 mM. The obtained lifetime (τ) vs. voltage (V) curves are shown in Figure 3.5. The data was fit to an exponential function derived from Mathé 2.5. All three curves share the same value for the global fit parameter V_β (48 mV), while the extrapolated lifetime at zero voltage τ_0 was fitted for every curve individually. We observed a strong decrease in quadruplex stability towards lower potassium concentrations. The extrapolated lifetime at zero voltage decreased from 3.5 ± 1.1s at 1 M KCl to 0.5 ± 1.1s at 10 mM KCl concentration. As the debye length was maintained at ≈ 0.3 nm in our measurements, this effect may not be explained by a weaker electrostatic shielding at low KCl concentrations. Furthermore, in the presence of high concentrations of quadruplex-stabilizing potassium ions comparatively high unfolding voltages have to be applied, which are close to the maximal voltage sustained by lipid bilayer membranes (≈ 250 mV). This makes it hard to reliably measure binding of thrombin to the aptamer, which even further stabilizes the structure.

We therefore deliberately destabilized the aptamer structure by increasing the measurement temperature to 37 °C, and by reducing the potassium concentration. For thrombin-binding studies, was used a KCl concentration of 10 mM, while maintaining an overall ionic strength of 1 M through the addition of NaCl.

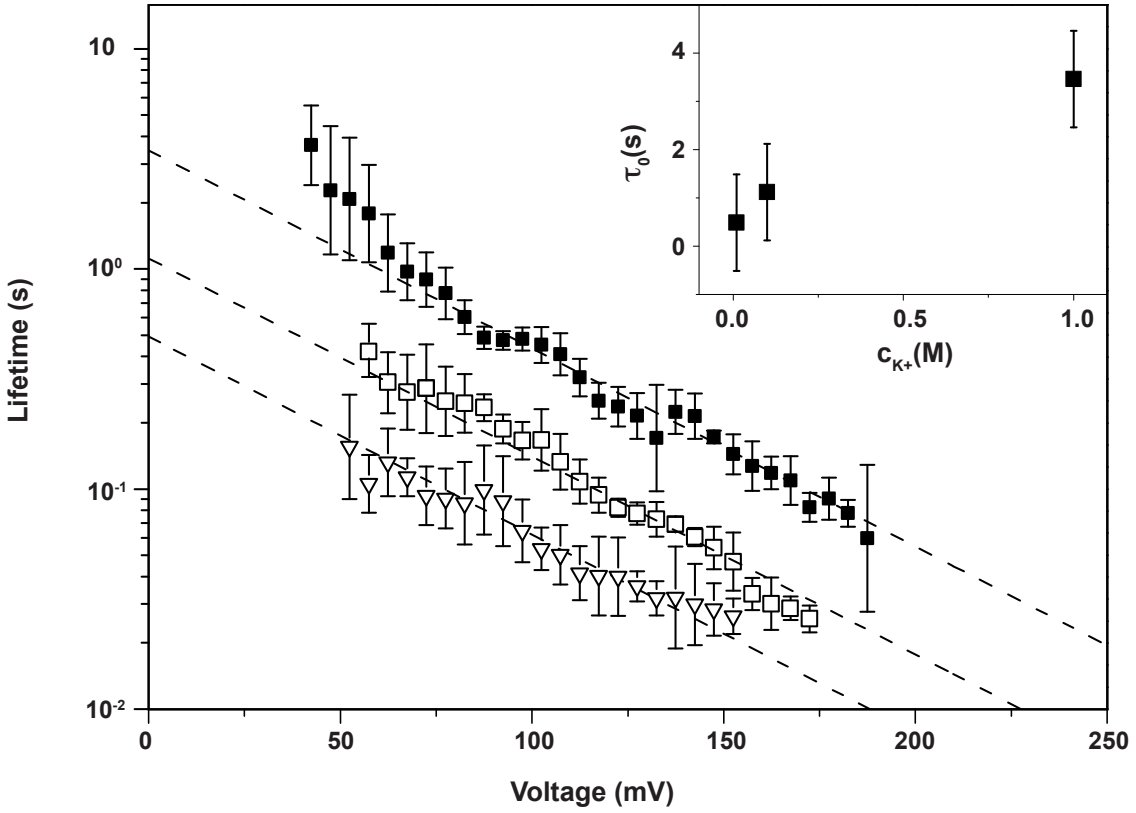

Figure 3.5: Thrombin aptamer stability as function of potassium concentration. Voltage dependent lifetime of structures at 1M (full squares), 100 mM (open squares) and 10 mM KCl concentration (open triangles). The overall ionic strength was maintained at 1 M by adding NaCl. Error bars are standard deviations from 5, 3 and 4 independent measurements, respectively. Dashed lines represent mono-exponential fits to the data. Inset: Extrapolated lifetime at zero voltage τ_0 determined from fits as a function of potassium concentration. Error bars are standard deviations obtained from fits.

In the absence of thrombin, we observed a single population in the unfolding voltage histogram (see Figure 3.6). We also performed experiments in the presence of 2 and 3 μM thrombin. At these concentrations a bound fraction of ≈ 100 % is expected for a K_d in the nanomolar range. Nevertheless, we observed an increase of the number of events at higher unfolding voltages accompanied by a shift of the most frequent unfolding voltage to a higher value and a broadening of the distribution.

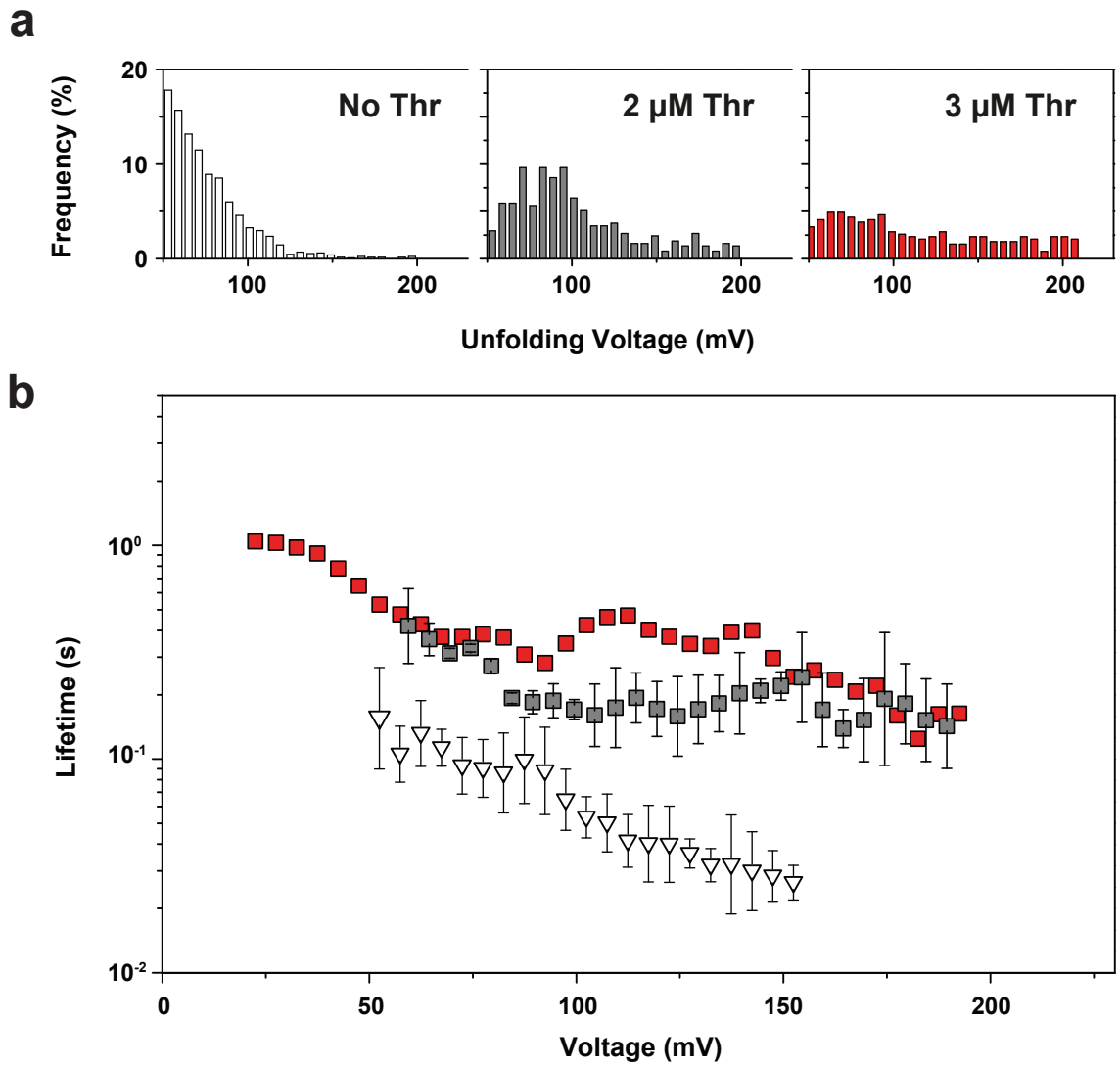

Figure 3.6: Unfolding of the thrombin aptamer at 10 mM K^+. a) Typical unfolding voltage distributions without (open bars)) and with (full bars) addition of thrombin at different concentrations (grey: 2 µM, red: 3 µM). Experiments were performed at a loading rate of 0.2 V s^{-1}. b) Voltage dependent lifetime of aptamer structures (open triangles) and aptamer - target complexes (full squares, grey: 2 µM, red: 3 µM thrombin). Error bars are standard deviations from 2 independent measurements.

To check whether bound and unbound populations can be separated at intermediate thrombin concentrations, we used Eq. 2.6 2 to calculate the unfolding voltage distribution for a bound fraction of 50% (see Figure 3.7). The parameters $V_{\beta i}$ and τ_{0i} were determined from single exponential fits to the lifetime vs. voltage curves in presence and absence of thrombin, respectively. The obtained curve shows, that bound and unbound populations overlap strongly and cannot be separated accurately in the experimental histograms. However, the fraction of events at higher unfolding voltages (>150 mV) still increases from 2 μM to 3 μM thrombin, indicating a larger unbound fraction than expected at such concentrations. This may be caused by a lower capture rate for the more slowly diffusing bound complexes.

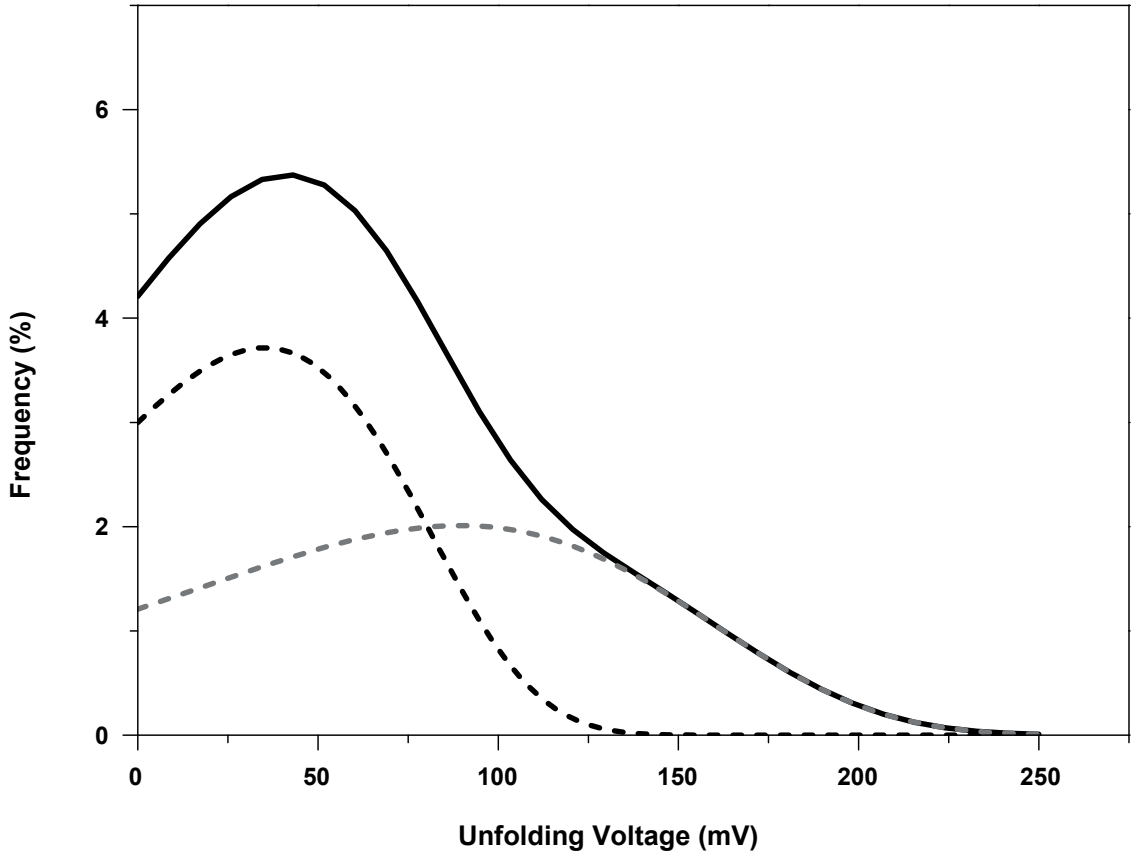

Figure 3.7: Simulated unfolding voltage distribution for the thrombin aptamer - ligand complex at a ligand-bound fraction of 50% (solid line). Individual subpopulations are shown as dashed lines (black: unbound, grey: ligand-bound). Curves were calculated from Eq. 2.6, using V_β and τ_0 values that were determined from single exponential fits to the voltage-dependent lifetime in absence and presence of thrombin, respectively (see Figure 3.6).

As before, we obtained the voltage-dependent lifetime of the complexes in the nanopore using the conversion formula of Eq. 2.10. In the voltage range considered, the thrombin-complexes typically have a 10-fold longer lifetime than the aptamer structure without thrombin. This difference is actually dependent on the potassium concentration. Experiments were performed at different KCl concentration, from 10 mM to 100 mM (see Figure 3.8). In the presence of thrombin, the observed stability is comparable to the 10 mM case, which is in contrast to the increasing stability of the unbound aptamer structure. Therefore, the stability difference of the bound and unbound case diminishes towards higher KCl concentrations.

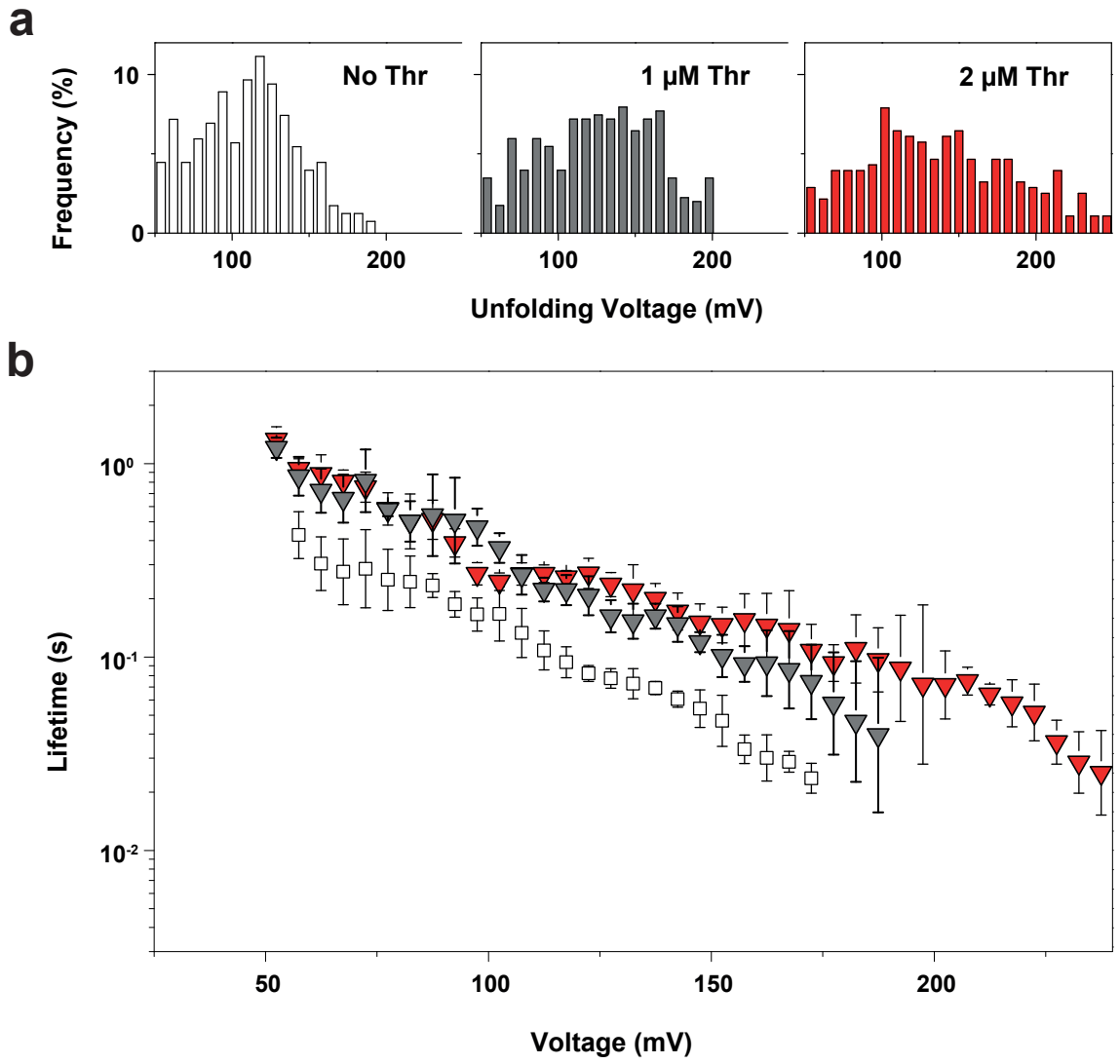

Figure 3.8: Unfolding of the thrombin aptamer at 10 mM K^+. a) Typical unfolding voltage distributions without (open bars) and with (full bars) addition of thrombin at different concentrations (grey: 1 µM, red: 2 µM). Experiments were performed at a loading rate of 0.2 V s^{-1}. b) Voltage dependent lifetime of aptamer structures (open squares) and aptamer target complexes (full triangles, grey: 1 µM, red: 3 µM thrombin) at apotassium concentration of 100 mM. Error bars are standard deviations from 3 independent measurements.

3.1.4 Conclusions

We performed experiments with two 'standard' aptamers - the ATP-binding aptamer and the thrombin aptamer. One of the most attractive features of nanopore force spectroscopy is that - in principle - it allows the measurement of molecular unfolding rates. For instance, our experiments indicate that AMP-aptamer complexes unfold slightly faster than ADP or ATP complexes, whereas the fraction of bound complexes (reflecting the association constant $1/K_d$) is higher for AMP than for ADP or ATP. We determined a dissociation constant for the

ATP-aptamer of $K_d \approx 119\mu$M in the presence of 1M monovalent salt. Furthermore, we found increasing affinity of the aptamer to ATP, ADP, and AMP under these buffer conditions. It indicates a correspondingly higher on-rate for the less charged adenine nucleotides.

We also were able to detect the formation of stable aptamer-ligand complexes for the thrombin aptamer. Due to the high stability of the G quadruplexes and also the aptamer-ligand complex, the experiments required careful tuning of the experimental parameters, indicating that NFS is more suitable for small ligand aptamers than for strong protein binders.

Other limitations of NFS become apparent when dealing with stronger secondary structures, and with aptamer-target complexes with lower K_d. In the case of the thrombin aptamer, which was also studied in this work, already the secondary structure of the target-free aptamer - containing guanine quadruplexes - is very strong. This not only prevents application of the backward translocation technique, it also requires the application of higher voltages, which reduces the stability of the lipid bilayer membrane. A related problem is that the bound and unbound aptamer fractions strongly overlap, which makes an interpretation of the data difficult. Measuring a titration curve for aptamers with low K_d requires application of aptamer targets at correspondingly low concentrations. Slower diffusion of the aptamer-target complexes combined with low on-rates for complex formation may then lead to an incorrect representation of the molecular distributions in solution in the unzipping experiments. In this case, other nanopore-based techniques for the study of aptamer-ligand interactions such as that developed in Ref. [133] are more suitable. Another option might be the utilization of solid state nanopores for force spectroscopy, as for these the accessible force range is potentially higher [146].

3.2 Force spectroscopy on RNA molecules

Biological nanopores were involved in detecting microRNAs using a probe-base approach, where a probe molecule is designed to target a specific microRNA sequence by Watson-Crick base pairing in its central region, and the catching of the molecule in the pore is facilitated by $(dC)_{30}$ at its $3'$ and $5'$ ends [157]. Another approach of analyzing RNA complexes is to ligate the ends of a tRNA to a synthetic DNA adapter molecule [143]. The DNA leading strand facilitates the capture and the threading into the nanopore. A ϕ29 DNA polymerase (DNAP) was used as a "molecular brake" to slow the rate of translocation. Experiments are performed at constant voltages and in order to distinguish between two tRNAs a algorithm was employed to analyze sublevels of the blocked current.

Previous constant force experiments were performed to determine RNA hairpin stability, however as known from experiments performed on DNA, dynamic nanopore force spectroscopy can be an alternative with an easy-to-handle analysis routine. Proof-of-principle dynamic unzipping experiments were performed on RNA hairpins using the fast electronic trigger technique in the forward direction (see Sec. 2.1.3) and the anchor the technique in backward direction (see Sec. 2.1.4) at 37 °C and 23 °C, respectively. The design of the RNA structure is slightly different to the DNA designs described in previous sections:

- Backward direction experiments were performed with the **anchor technique**. A random sequence for the spacer is preferred over a repetitive sequence as it was previously reported that the transcription is terminated after 8-12 poly(A) nucleotides [64]. For RNA aptamer experiments, the usage of random sequences for the spacer was not possible due to potential interaction with the aptamer's binding pocket and a thereby induced misfolding of the structure. For this particular experiment the random sequence was replaced with a C_{30} or A_{30} sequence. The catching tail was added post transcriptionally by a *E.Coli* Poly(A) tailing polymerase.

- To overcome the necessity of a spacer the **Fast Electronic Trigger Technique** was employed in the forward direction. Two different catching tails are used: a random sequence of 40 bases or a long poly(A) tail added post transcriptionally.

Previous experiments [129, 136] had indicated that DNA secondary structures are considerably stabilized within the vestibule of the αHL pore. In this context, we performed experiments for the same RNA hairpin (GC_4AU_4) in forward and backward direction. Forward direction experiments had to be performed at 37 °C in order to sufficiently destabilize the RNA hairpin to apply NFS within the accessible voltage range. Although the RNA folding free energies calculated with mfold are $\Delta G_{37^0C} = -11.2$ kcal/mol and $\Delta G_{23^0C} = -15.2$ kcal/mol, unzipping critical voltage (V_C) is two times higher in the forward direction than in the backward direction. The results obtained for RNA secondary structures are in agreement with the results reported for DNA. It can also be seen that a second more unstable population emerges for the backward experiment. Here, a probable explanation is wrongly transcribed DNA that is discarded in forward experiments. With anchor technique all RNA molecules that present an anchor can be analyzed, even though the hairpin is not correctly transcribed. Low transcription efficiency can be cased by the presence of the spacer. Due to the stability differences observed for backward and forward experiments, RNA and DNA unfolding will be considered separately in forward and backward direction.

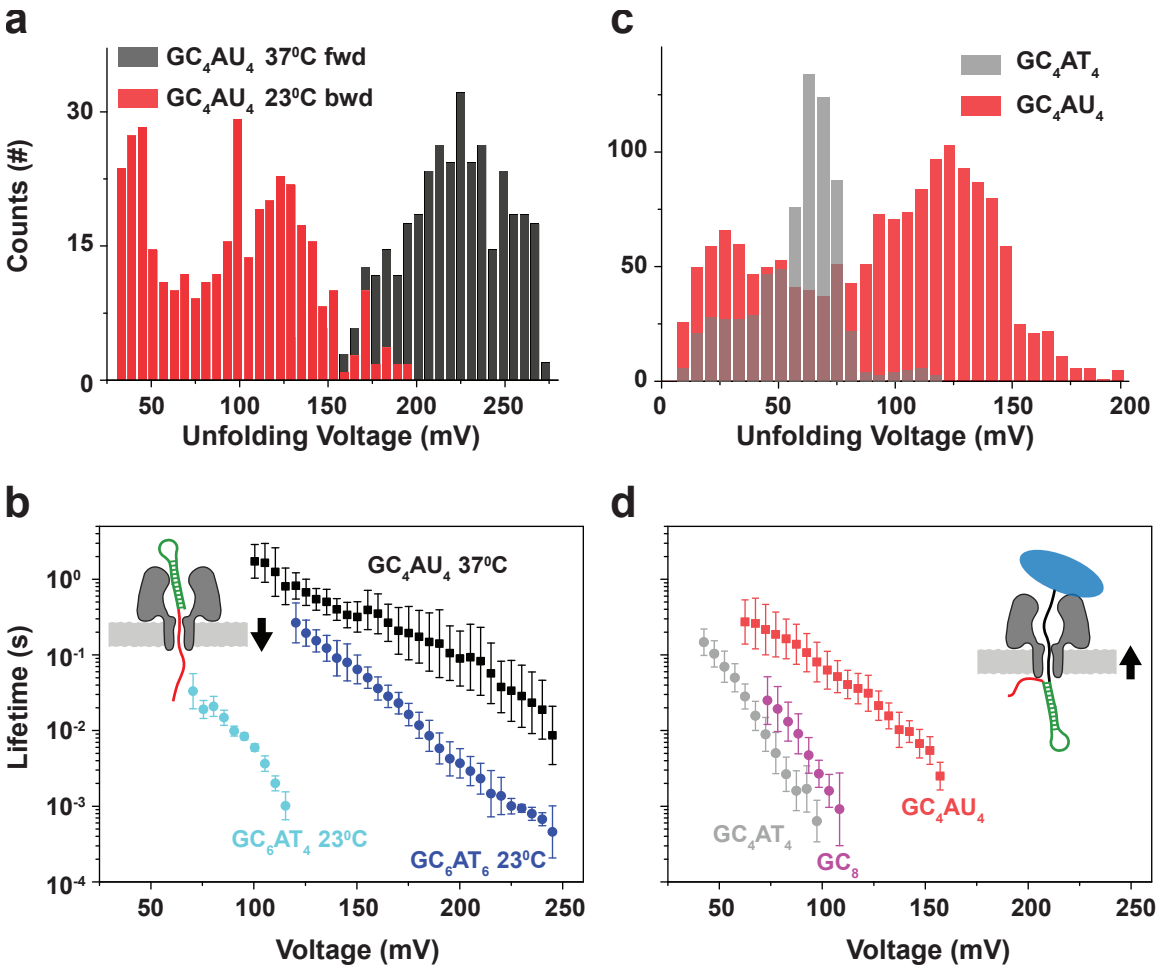

Figure 3.9: DNA, RNA stability comparison. a) Unfolding voltage distribution at a loading rate of 2 V/s for RNA hairpins (GC_4AU_4) in forward (black) and backward (red) direction at 37 °C and 23 °C, respectively. V_C shifts from 112 mV (bwd) to 224 mV (fwd) b) Voltage dependent lifetime in forward direction for a RNA hairpin GC_4AU_4 at 37 °C (black) and two DNA hairpins, GC_6AT_4 at 23 °C (cyan), GC_6AT_6 at 23 °C (blue). c) Distribution of unfolding voltage for DNA (gray) and RNA (red) hairpins at a loading rate of 1 V/s. Experiments performed at 23 °C in backward direction using anchor technique. d) Voltage dependent lifetime in backward direction for a RNA hairpin GC_4AU_4 (red) and two DNA hairpins: GC_4AT_4 (gray) and GC_8 (magenta). Experiments were performed at 23 °C. Insets: Schematic representation of two different experimental techniques, in the forward and the backward direction. Color coding: the investigated hairpin (green), the spacer (black), the catching tail (red) and the anchor (blue).

Figure 3.9 b the depicts lifetime at constant voltage for DNA and RNA hairpins in the forward direction. Three hairpins are chosen, a RNA hairpin GC_4AT_4 ($\Delta G_{37^0C} = -11.2$ kcal/mol) and two DNA hairpins GC_6AT_4 ($\Delta G_{23^0C} = -13.4$ kcal/mol) and GC_6AT_6 ($\Delta G_{23^0C} = -16.9$ kcal/mol). Surprisingly, we found that the RNA hairpin is more stable

than DNA hairpins even though folding free energies are lower for DNA hairpins. Several questions arose after this experiments: is this effect enhanced by the vestibule of αHL or is the experiment temperature not accurate.

To answer these questions backward direction experiments where performed (*trans* $\rightarrow$ *cis*) at room temperature. Two DNA hairpins were chosen: GC_4AT_4 (-10.5 kcal/mol) and GC_8 (-15.6 kcal/mol) and one RNA hairpin GC_4AU_4 (-15.2 kcal/mol). In Figure3.9 b, unzipping voltage histograms are plotted for a DNA hairpin (GC_4AT_4, gray) and RNA (GC_4AU_4, red) molecules. Even though the DNA and the RNA hairpins have an equal number of bases, higher stability was measured for the RNA, however this is still in agreement with the folding free energies. Next, we considered the GC_8 DNA hairpin which has a folding energy comparable with the RNA hairpin (see Figure 3.9 d). The same pattern as for the forward direction, was observed for backward experiments.

Exp	Structures				$-\Delta$G (kcal/mol)	τ_{100mV}(ms)
	Anchor	Spacer	HP	Tail		
fwd			GC_6AT_6	$(dT)_{50}$	16.9	520
			GC_6AT_4	$(dC)_{50}$	13.4	4.5
			GC_4AU_4	$Rand_{40}$	11.2 (37 °C)	960
bwd	GC_{12}	$(dT)_{50}$	GC_4AT_4	$(dT)_{30}$	10.5	0.5
	Q	$(dT)_{50}$	GC_8	$(dT)_{30}$	15.6	2.1
	GC_{10}	$Rand_{30}$	GC_4AU_4	poly(A)	15.2	52
Apt	GC_{10}	A_{30}	MGA	poly(A)	20.7	8.6
bwd	GC_{10}	A_{30}	MGA	poly(A)+MG		86.5
	GC_{10}	C_{30}	MGA	poly(A)	20.7	

Table 3.1: Stability comparison DNA-RNA and MG-Aptamer

Information about the lifetime of hairpins inside a nanopore at different voltages may be extracted from graphs in Figure 3.9 b and d. The lifetime of the molecule under no force is of particular interest. This corresponds to the lifetime at 0 mV. Assuming a first-order two state reaction the curves can be exponentially extrapolated, so that a τ_0 can be determined. But, as described in Ref. [136], hairpin unzipping and translocation is a complex process, which depends on the unzipping energy landscape and a simple phenomenological fit will not give us an accurate result. In this context we choose to extract the τ_{100mV} the lifetime at 100mV, although theoretical estimations for force extension unzipping curves show a large number of structural transitions that take place during force-induced RNA denaturation in contrast to the force free case [54].

Results obtained for forward and backward experiments for RNA and DNA secondary structures are summarized in Table 3.1. For example, in forward direction the RNA free energy is 20% lower than for DNA, but the τ_{100mV} is 20 fold higher. Similar in backward direction, although free energies for both hairpins are almost identical a 25 fold higher τ_{100mV}

was measured for RNA. Based on these findings we can hypothesize that the mechanical stability is higher for RNA hairpins and can not be predicted by the free energy of folding or the melting temperature.

As presented in Sec. 3.1.1 nanopore-based force spectroscopy is an accurate technique to study DNA aptamers and DNA-target complexes. In order to study RNA aptamer binding to its target using force spectroscopy, the malachite green aptamer (MGA) was chosen as a model. We used a A_{30} or a C_{30} as a spacer and a poly(A)-tail for catching added by *E.coli* Poly(A) Polymerase.

In the unfolding histogram for the MGA with a C_{30}-spacer, one population appears with a V_C =29 mV. In contrast, the RNA structure with a A_{30}-spacer presented two populations with V_{C1} =25 mV for the first population and V_{C2} =93 mV for the second population.

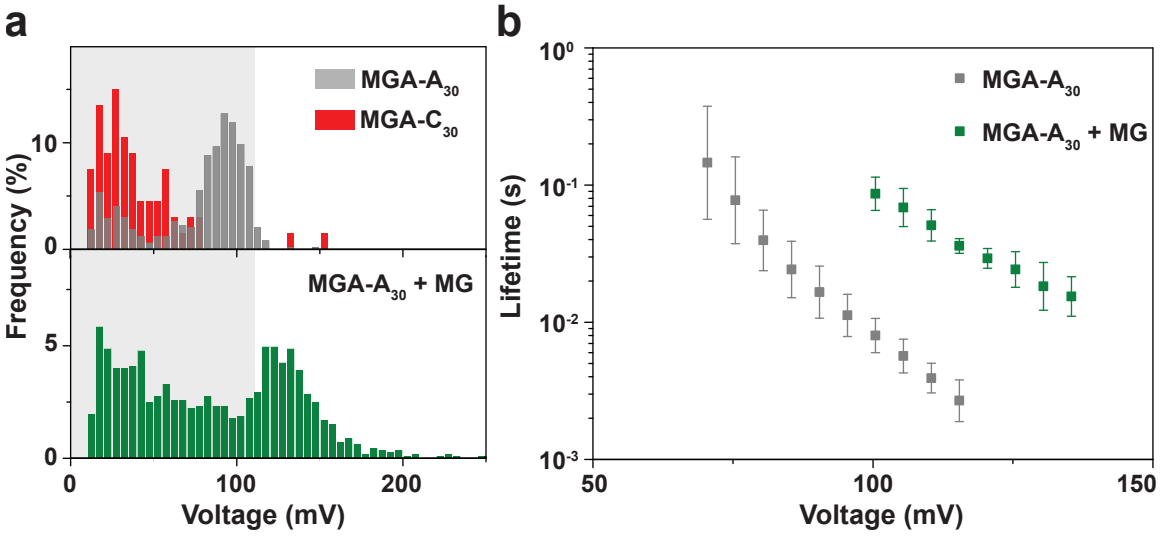

Figure 3.10: Malachite green aptamer (MGA) stability analysis. a) Unfolding voltage distribution for MGA with a A_{30}-spacer (gray), MGA with a C_{30}-spacer (red) and RNA-MG complex with a A_{30}-spacer (green) at a loading rate of 1 V/s. b) Voltage dependent lifetime of RNA and RNA aptamer (gray) MG complex (green) with a A_{30}-spacer. Experiments performed at 23 °C in backward direction using the anchor technique.

Secondary structures calculated with NUPACK show, that the aptamer interacts with the C_{30}-spacer, which disturbs the formation of the aptamer binding pocket. It is known that, MG fluorescence enhances upon aptamer binding, therefore the functionality of the aptamers was checked with fluorescence experiments. It was found that exchanging the A_{30}-spacer with the C_{30}-spacer reduces binding efficiency by ≈55%. In this context the binding partner was added on the MGA containing a A_{30}-spacer (see Figure 3.10 a, green). The unfolding voltage histogram is fitted using Eq. 2.6 and the V_C =125 mV and V_β =30 mV was obtained for the bound population, representing 70% of all recorded events. The lifetime versus voltage was plotted (see Figure 3.10 b) for the MGA and the MG-aptamer complex, the τ_{100mV} increased 10 fold for the MG-aptamer complex. The dissociation constant could not be determined as in the previous section for the ATP aptamer, due to MG concentration varying over time. Because of its lipophilic properties, the MG tends to dissolve into hexadecane which is used for the DIB oil bath.

In the next stage, NFS experiments were performed on the flavin mononucleotide aptamer

(FMNA). To overcome the necessity of an spacer and an anchor, Fast Electronic Trigger Technique was employed for analyzing poly(A) modified RNA aptamers. The vestibule influence was annihilated by performing the experiment in backward direction even though the catching probability from the *trans* side is low. Results are presented in the master thesis of D. Ziegler.

4 Origami Pores

A series of synthetic nanopore structures were developed, for which scaffold routing and shape was varied as well as the number of hydrophobic modifications.

- The lipid bundle pore (LB) was folded by using a 7249 bases long scaffold. The structure is made of 54 double helices packed on a honeycomb lattice (see Figure 4.1 a), consisting of two modules: a stem that penetrates and spans a lipid membrane, and a barrel-shaped cap that adheres to the membrane. The stem protrudes centrally from the barrel and consists of six double-helical DNA domains that form a hollow tube. The interior of this tube serves as a transmembrane channel with a diameter of ≈2 nm and a length of ≈42 nm and runs through stem and barrel (see Figure 4.1 b). The vestibule contains unused scaffold loops. The adhesion to the lipid bilayer is mediated by 28 cholesterol moieties (see Figure 4.2 a).

  Data previous published in Ref.[95], experiments were performed with Martin Langecker (electrical characterization), Thomas Martin (design of DNA origami and TEM analysis) and Jonathan List (channels vesicles interactions).

- The "pin"pore is an evolved version of the LB: the scaffold loops here become integrated into the structure as a well defined part of the vestibule (see Figure 4.1 d, e, f). Additionally strand breaking in the channel was avoided. Nominal lengths of several design elements are indicated in the image: height of the cap - 51 nm, length of the central stem - 42 nm, inner diameter - ≈2 nm transmembrane region - 14 nm.

  For the new generation of synthetic channels the attachment to the lipid membrane is mediated by tocoherol moieties, since tocopherol is known to interact well with the disordered membrane phases formed by the phosphatidylcholines used in our experiments.

- The "wheel"pore was created to further improve membrane incorporation. The stem is a 6HB, the cap is flatter and wider than the one of the pin pore. This offers space for more hydrophobic modifications (see Figure 4.1 g). As a result, the structure has a higher number of parallel helices (126), which enable 57 modifications in the structure. The positions are indicated in red in Figure 4.2 b. The inter membrane stem has the same length as the pin pore of 14 nm. The structure contains holes to reduce misfolded variants (see Figure 4.1 i). The large structure requires a long scaffold (8064 bases).

- The T pore is designed following an alternative design strategy. The structure was created by using a square lattice with 56 double helices, folded using a 7560 base long scaffold. The T pore is composed of a double-layered plate (46 nm x 51 nm) with 57 hydrophobic modifications at its bottom and a rectangular aperture with dimensions 3.7 nm x 8.4 nm in its centre. In contrast to the other pores, the helices of the stem are oriented perpendicularly to the top plate. The 27 nm long stem is composed of 12 helices arranged in a square (cross-section 4.2 nm x 4.2 nm). The T pore has a larger diameter pore of area 35.7 nm^2, in the top layer. The second layer has a hole with area of 55.5 nm^2. The stem contributes with an area of 21.2 nm^2. The structure has an effective rectangular pore with with sides 3.74 nm and 4.6 nm. The structure also

has no scaffold loops or breaks in the stem region (see Figure 4.1 j, k). The adaptor positions are indicated in red in Figure 4.2 c.

Transmission electron microscopy (TEM) images taken from purified structures (see Figure 4.1 c, f, i, l) confirmed that the intended shape is realized.

Second generation of synthetic channels were designed by Thomas Martin, dye influx and TEM measurements were performed with Swati Krishnan, elctrical characterization with Daniela Ziegler, results published in Ref. [91].

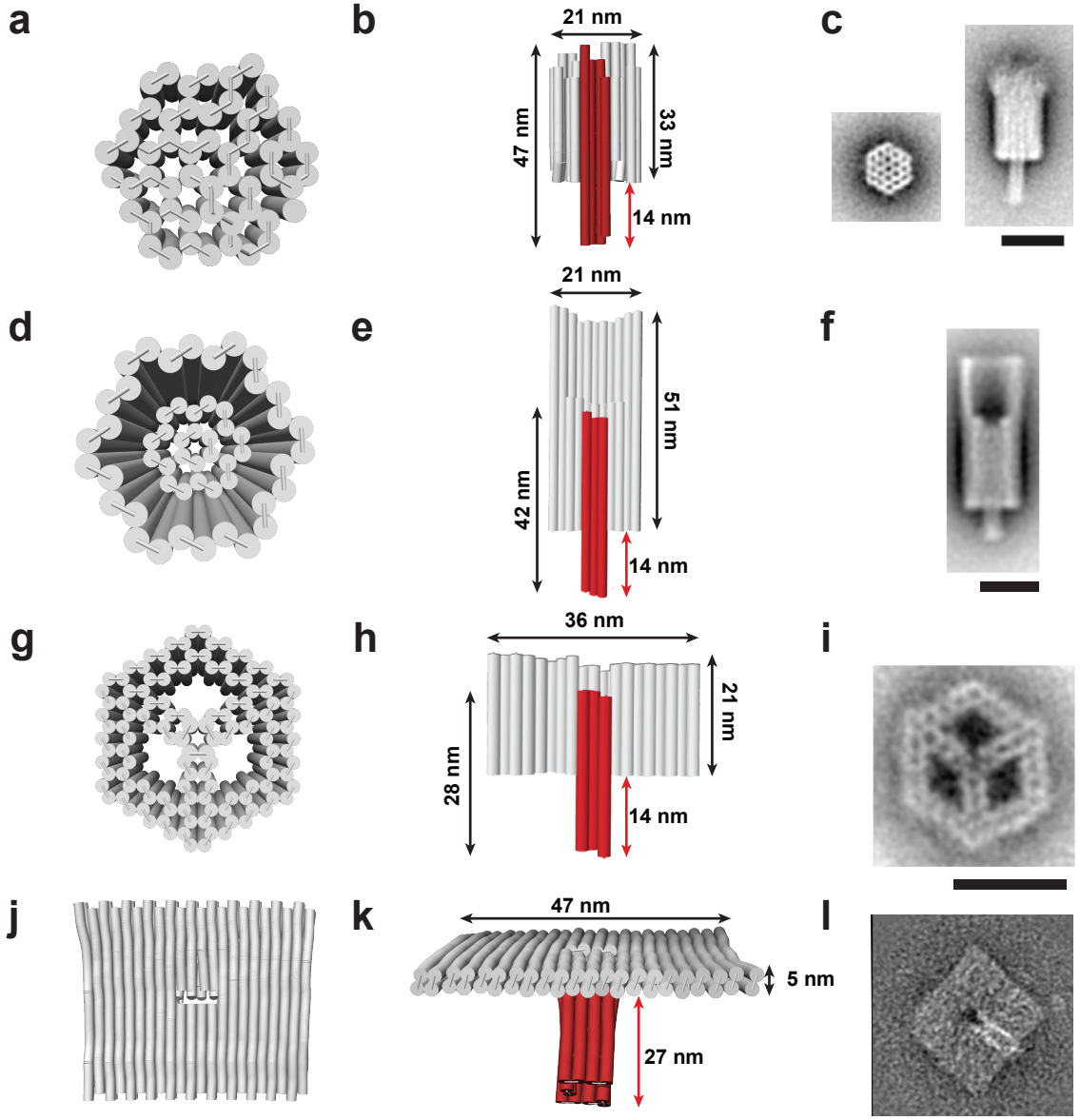

Figure 4.1: Design and electron microscopic characterization of DNA nanochannels. a) Schematic illustration of the channel top view. b) Side view of the channel. Each cylinder depicts one DNA double helix. The transmembran channel is represented in red. c) Averaged negative-stain TEM images obtained from DNA channel structures (top and side view) d) Schematic design of the "pin pore" (top view). e) Design of the pin pore (side view). f) Class averaged TEM image of the pin pore (side view) showing the cap structure and vestibule at the entrance to the pore. g) Schematic representation of "wheel pore" (top view), which is composed of 126 parallel DNA duplexes. h) Side view of the "wheel pore". i) Class averaged TEM image of the wheel pore (top view). j) Schematic top view of the "T pore". k) Design of the T pore (side view), which is composed of a double-layered DNA plate and a stem attached to the center of the plate. l) TEM class average image of the T pore showing the plate and stem of the structure.

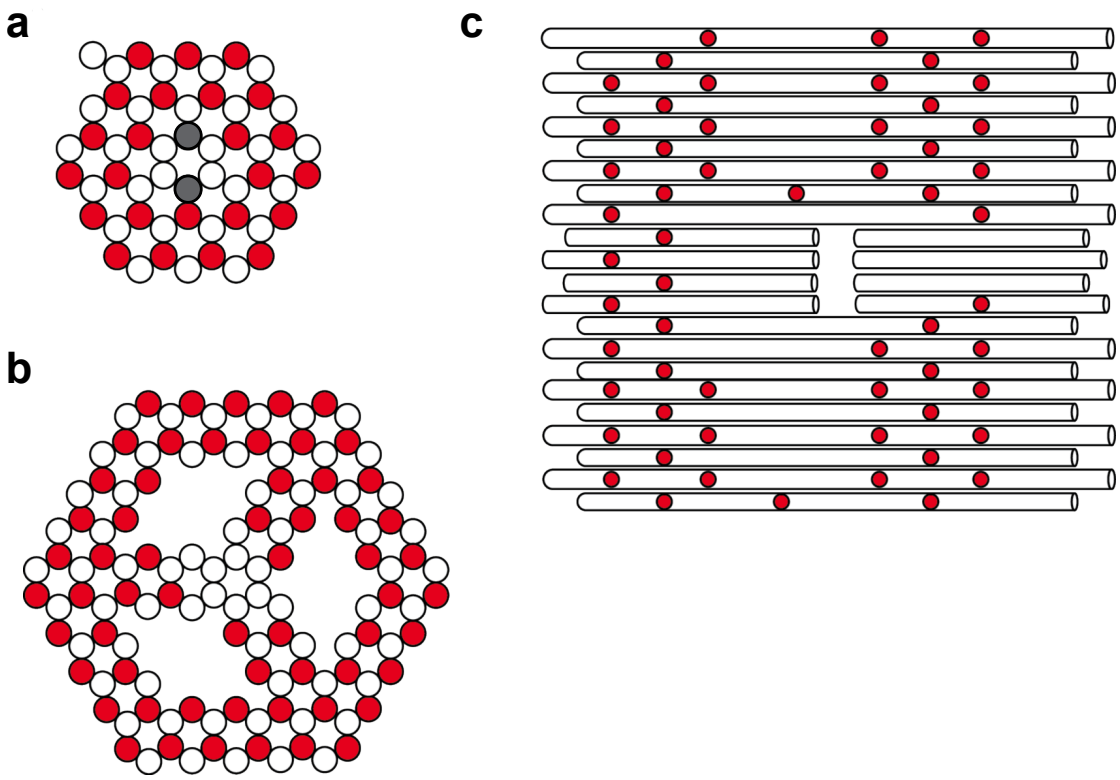

Figure 4.2: Distribution of adaptors on the DNA nanostructures. a) Red circles in the schemes indicate cholesterol modifications at the bottom of the DNA channel "barrel" domain, gray circles are modifications protruding from the sides of the six helix stem. The handles are single-stranded staple extensions (all having the same sequence: 5′-TAACAGGATTAGCAGAGCGAGG-3′) to which a complementary adaptor strand having a tocopherol modification at its 5′ end can hybridize (5′-CCTCGCTCTGCTAATCCTGTTA-3′). The lipid bundle pore has 28 possible handle positions. The pin pore has 26 possible handle positions, the two modifications on the stem presented for lipid bundle are removed. b) The wheel pore has 57 modification positions at the bottom of its cap, which improves membrane incorporation, but also increases the tendency to aggregate. c) The T pore also has 57 modification positions as indicated in red.

4.1 Vesicle measurements

4.1.1 TEM based evidence for channel-membrane interaction

Experiments performed in the presence of small unilamellar vesicles (SUVs) confirmed that the DNA channels bind to lipid bilayer membranes in the desired orientation in which the hydrophobic-modified face of the barrel forms tight contact with the membrane and the stem appears to protrude into the lipid bilayer. These observations suggested that the synthetic channels could form membrane pores as designed. Figure 4.3 depicts the interaction of LB with lipid vesicles and lipid patches.

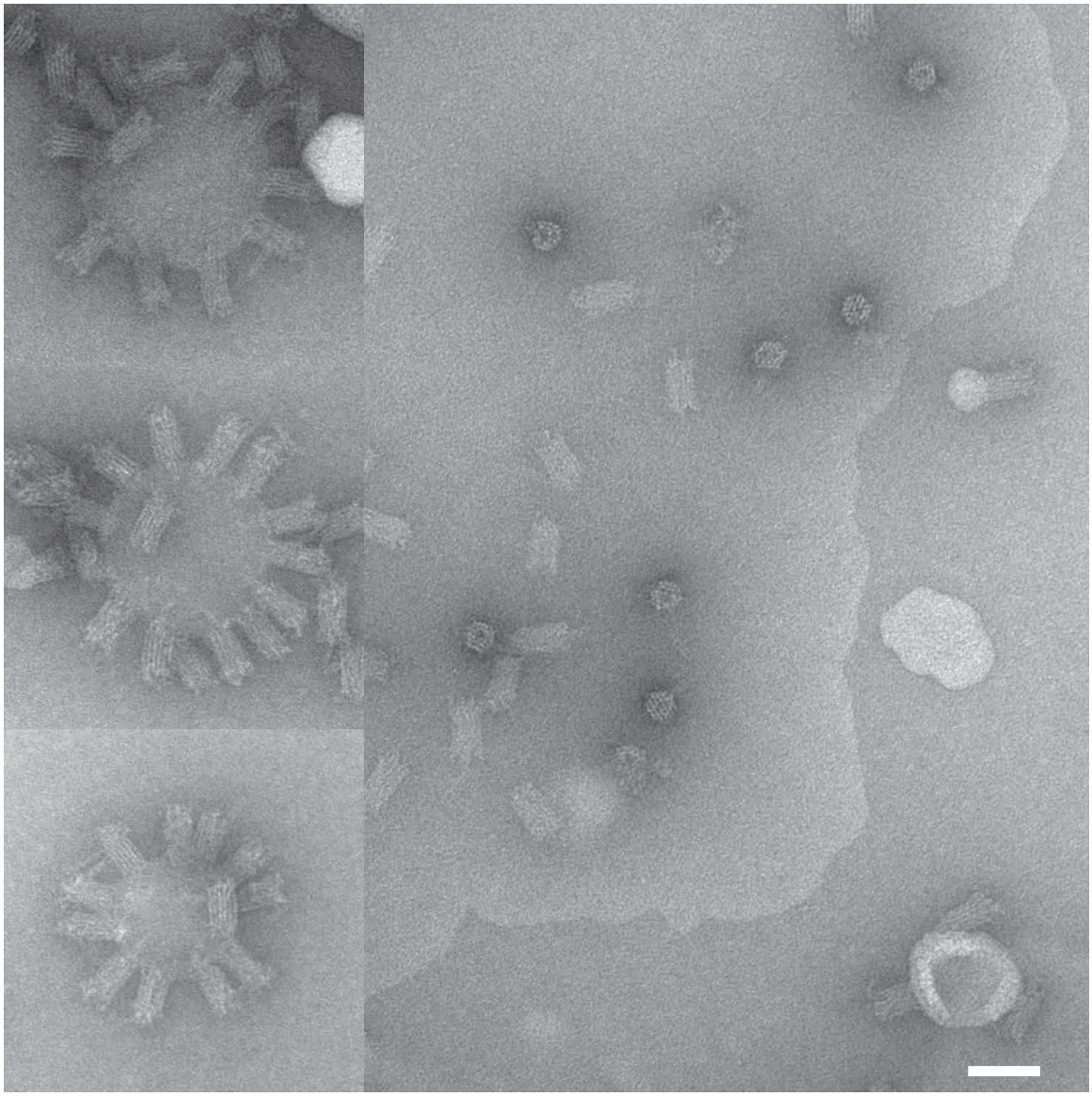

Figure 4.3: Negative-stain TEM micrographs of cholesterol-modified LB channels attached to POPC membrane. Scale bar: 50 nm.

We further investigated the influence of the number of cholesterol modifications on their efficacy of promoting binding of the LB to membranes. A statistical analysis of our samples showed that the small unilamellar vesicles had a typical projected diameter on the order of 50 nm. The fraction of vesicles with at least one DNA channel increased with the number of cholesterols, with good binding starting above ≈10 cholesterols per channel (see Figure 4.4).

The TEM data obtained with the LB channel version featuring 26 cholesterols further clearly revealed that the cholesterol modifications at the stem-face of the barrel promote binding of the DNA channel to lipid membranes in the desired orientation in which the stem faces the membrane (see Figure 4.4 c).

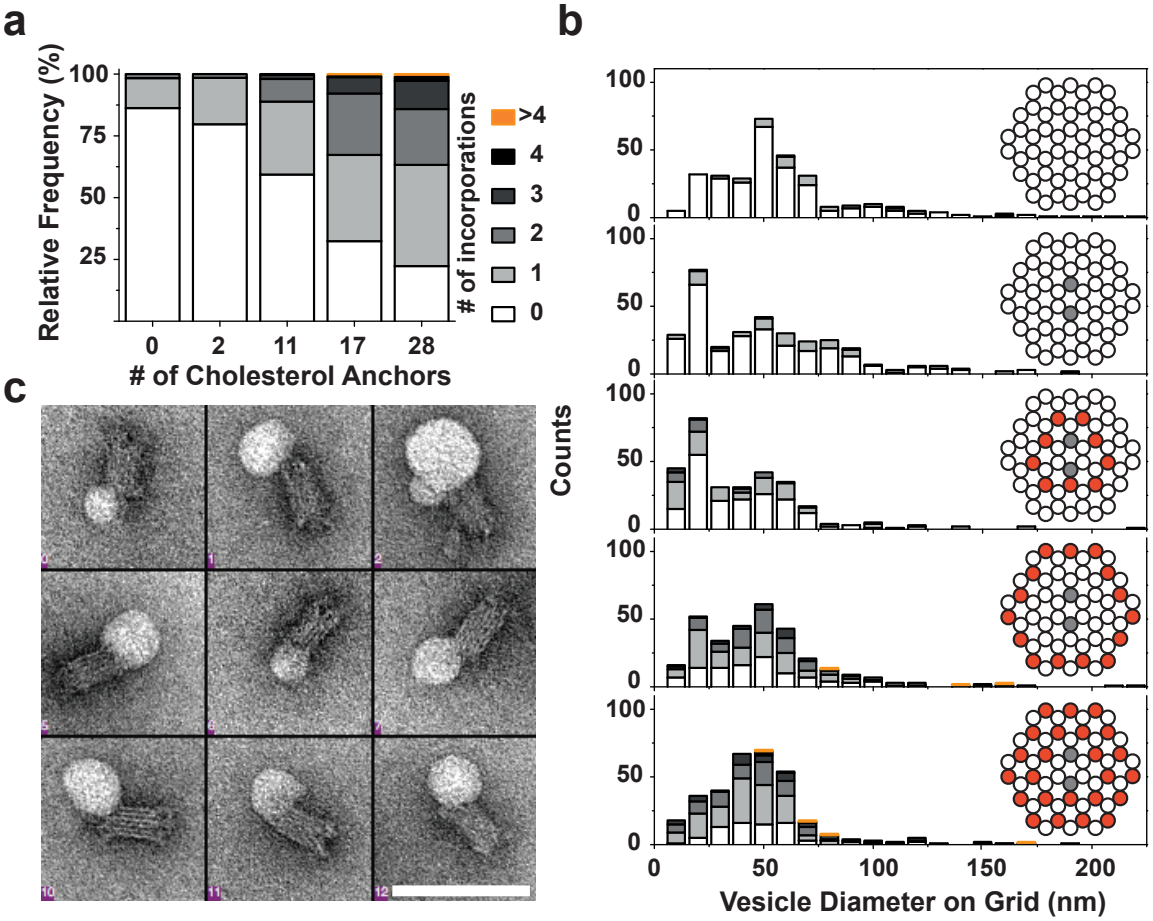

Figure 4.4: Influence of cholesterol anchors on the LB incorporation into membranes. a) Statistical analysis of size distribution of membrane patches and influence of the number of cholesterols per DNA channel on binding. b) Combined histograms showing the SUV size distribution (apparent diameter upon adsorption to the TEM grid) and the binding efficiency. Red circles in the schemes indicate cholesterol modifications at the bottom of the DNA channel "barrel" domain, gray circles are protruded modifications from the sides of the six helix stem. c) Negative-stain TEM micrographs of cholesterol-modified DNA channels attached to POPC small unilamellar vesicles (SUV).

Similar behavior was observed for other synthetic channels. The pin pore interacts with

the lipid membrane, the presence of the vestibule helps in easily identifying the orientation of the structure during TEM imaging with SUVs (see Figure 4.5). On TEM image, the pore is not always oriented perpendicularly towards the lipid membrane (see Figure 4.5 top). Strong electrostatic interaction cause the long channel cap to interact with the vesicle.

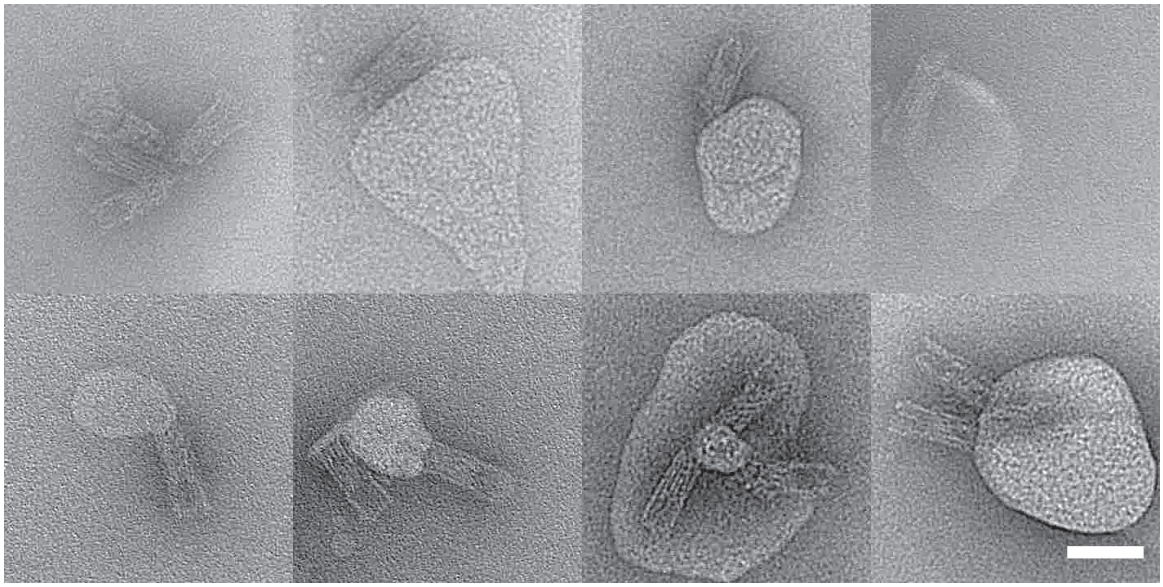

Figure 4.5: TEM images of the pin pore interacting with small unilamellar vesicles (POPC). The pores are oriented perpendicularly to the membrane surface, which is the desired orientation for transmembrane pore formation. The pores exhibit some aggregation but incorporate well into SUVs, potentially also supported by the high curvature of the SUV membrane. Scale bar: 50 nm.

We also surmised that due to its oblate aspect ratio, the wheel would tend to lie on the membrane in the correct orientation (see Figure 4.6).

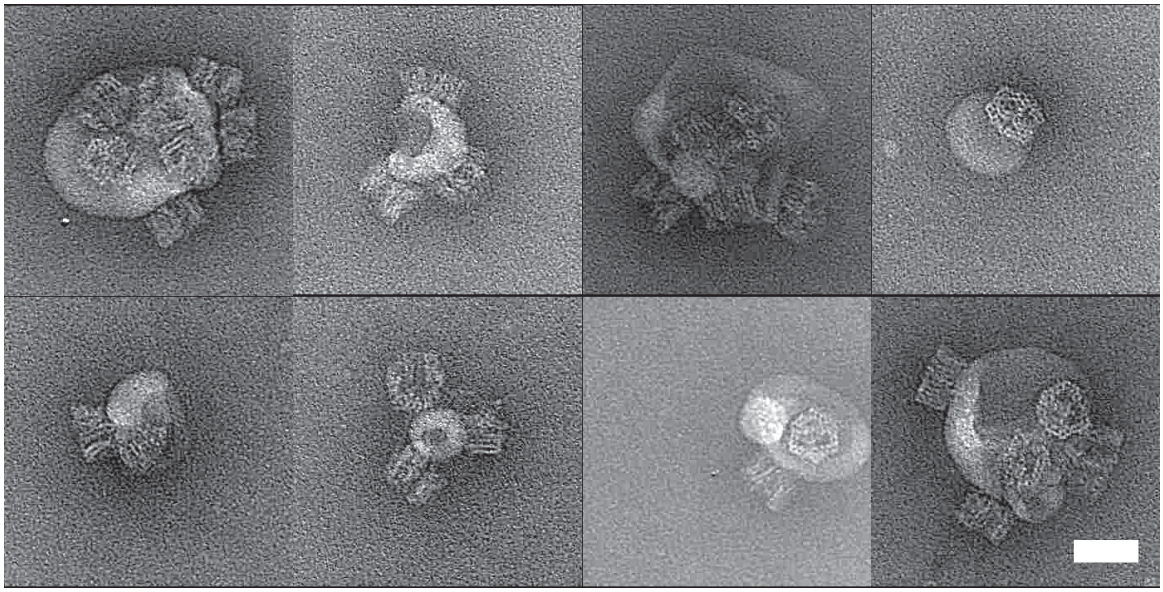

Figure 4.6: TEM images of the wheel pore modified with tocopherol moieties interacting with SUVs. Note the presence of some aggregation of pores on the SUVs. Scale bar: 50 nm.

The T pore shows strong interaction with the lipid membrane. The design helps a tighter binding of the structure with the lipid bilayer and the bending of the cap along the curvature (see Figure 4.7).

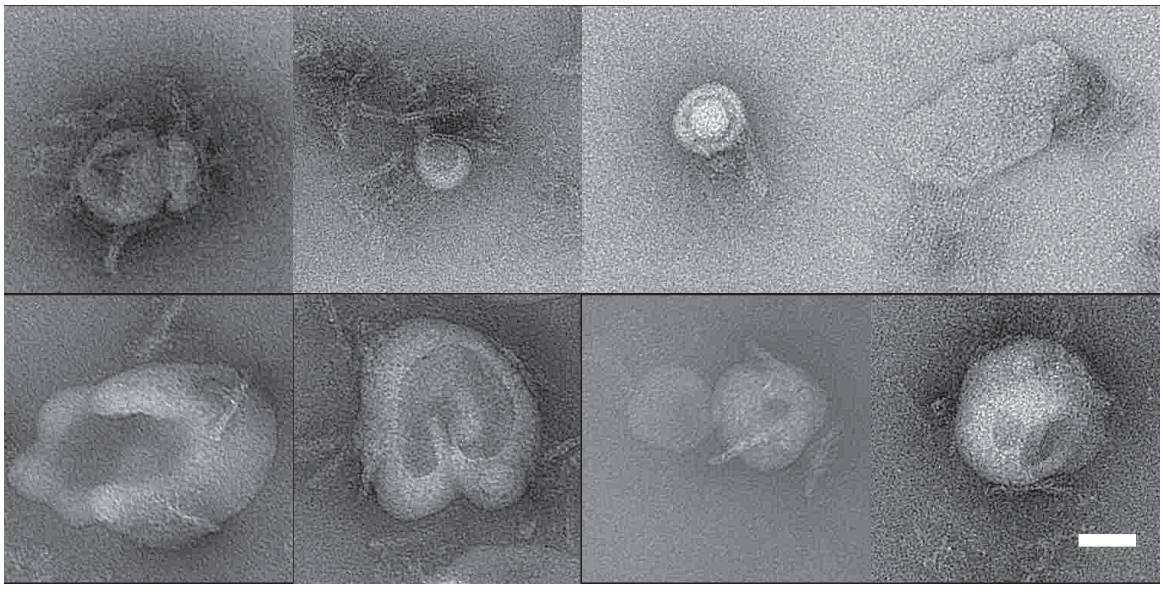

Figure 4.7: TEM images of T pores modified with tocopherol interacting with SUVs. Scale bar: 50 nm.

4.1.2 Dye influx assays for characterizing spontaneous membrane incorporation of DNA channels

The dye influx assay is regularly used to study interactions of membrane binding peptides and pores with lipid membranes, and has here been adapted to characterize membrane perforation by DNA origami pores. The assay involves the long term observation by confocal laser fluorescence microscopy of indvidual surface-immobilized giant unilamellar vesicles (GUV's). In order to be able to perform the studies, buffer conditions were carefully adjusted to avoid accidental bursting or perforation of the GUVs. The interior of the vesicles initially contained buffer solution only, while the exterior solution also contained the fluorescent dye Atto 633, which does not penetrate the lipid bilayer. After addition of nanopores at a nanomolar concentration, the vesicles were monitored for dye influx for several hours. Additionally a dextran-500000-fluorescein conjugate (nominal radius of 14.7 nm) that can not pass through the origami channel was added. Fluorescently labeled pores were added in order to prove pores absorption on the vesicle membrane. Control experiments were performed to rule out accidental bursting or leaking through spontaneously formed membrane pores. We found that both T pore (see Figure 4.8) and wheel pore (see Figure 4.12) were able to induce dye influx, while the pin pore (see Figure 4.13) was not.

Following will be presented dye influx experiments performed on the T pores added externally (final concentration ≈20 nM) on vesicles created using inverted emulsion technique. In experiments with fluorescently labeled pores (see Figure 4.8 a) we observed immediate adsorption of the pores to the vesicles, followed by a lag time after which the membrane was perforated (see Figure 4.8 b, c). Dye molecules tethered to a dextran moiety larger than the pore diameter were unable to enter the vesicles (see Figure 4.8 d). The control experiments when no channel solution is added show no dye influx (see Figure 4.8 e).

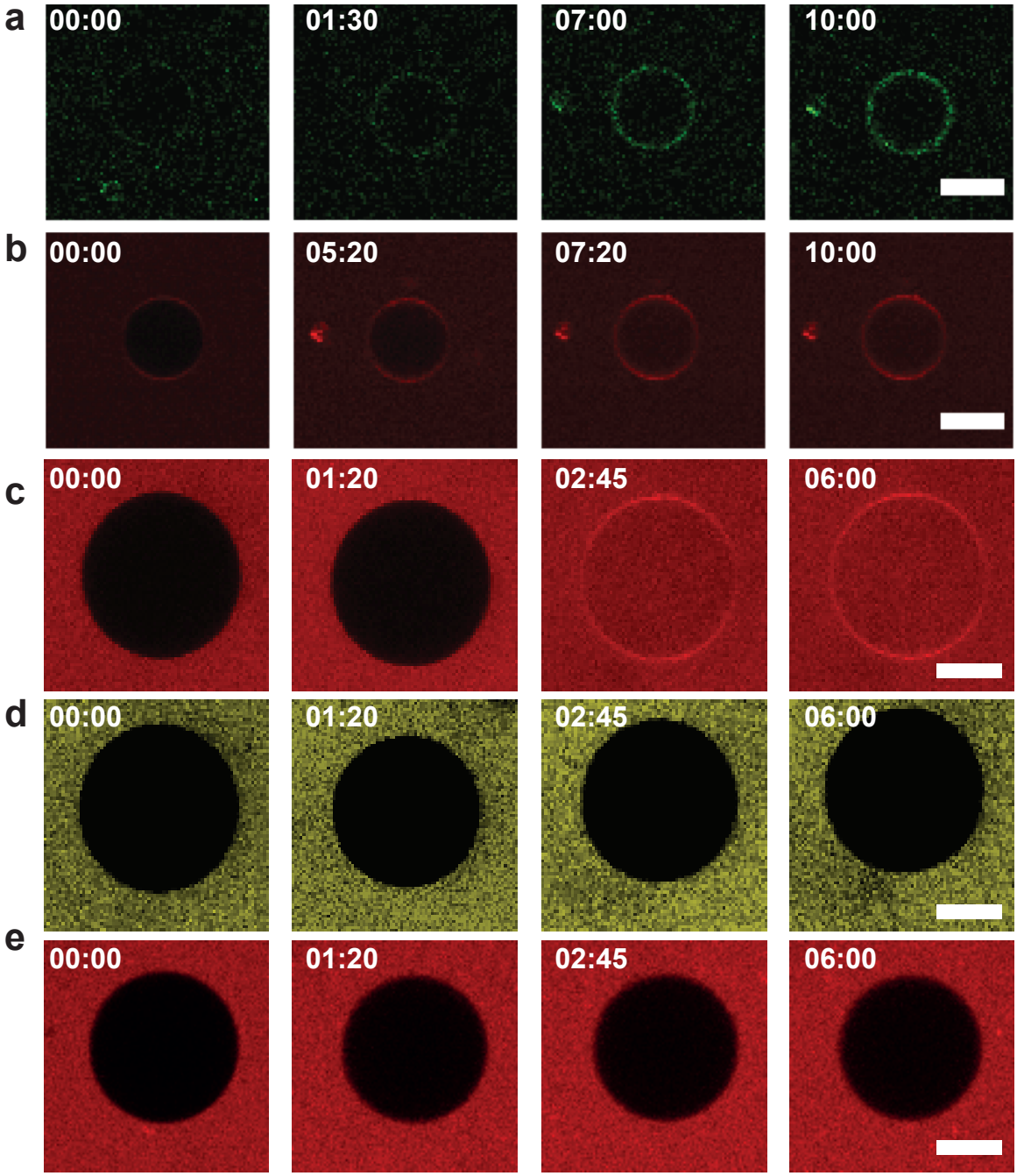

Figure 4.8: Dye influx experiments with GUVs and externally added T pore. a) Time series of confocal fluorescence microscopic images recorded during attaching of labeled origami channels to the vesicle wall. b) The same vesicle as in (a) monitoring dye influx (Atto 633) into vesicle. c) Other example of dye influx (Atto 633) into a vesicle. d) The same vesicle as in (c) observed in the fluorescein channel. The larger fluorescein-dextran conjugate present in the outside solution is unable to enter the GUV (nominal radius of 14.7 nm). e) Control experiment in the absence of DNA origami channels showing no dye influx during the course of the experiment (Image taken every 5 or 10 minutes).

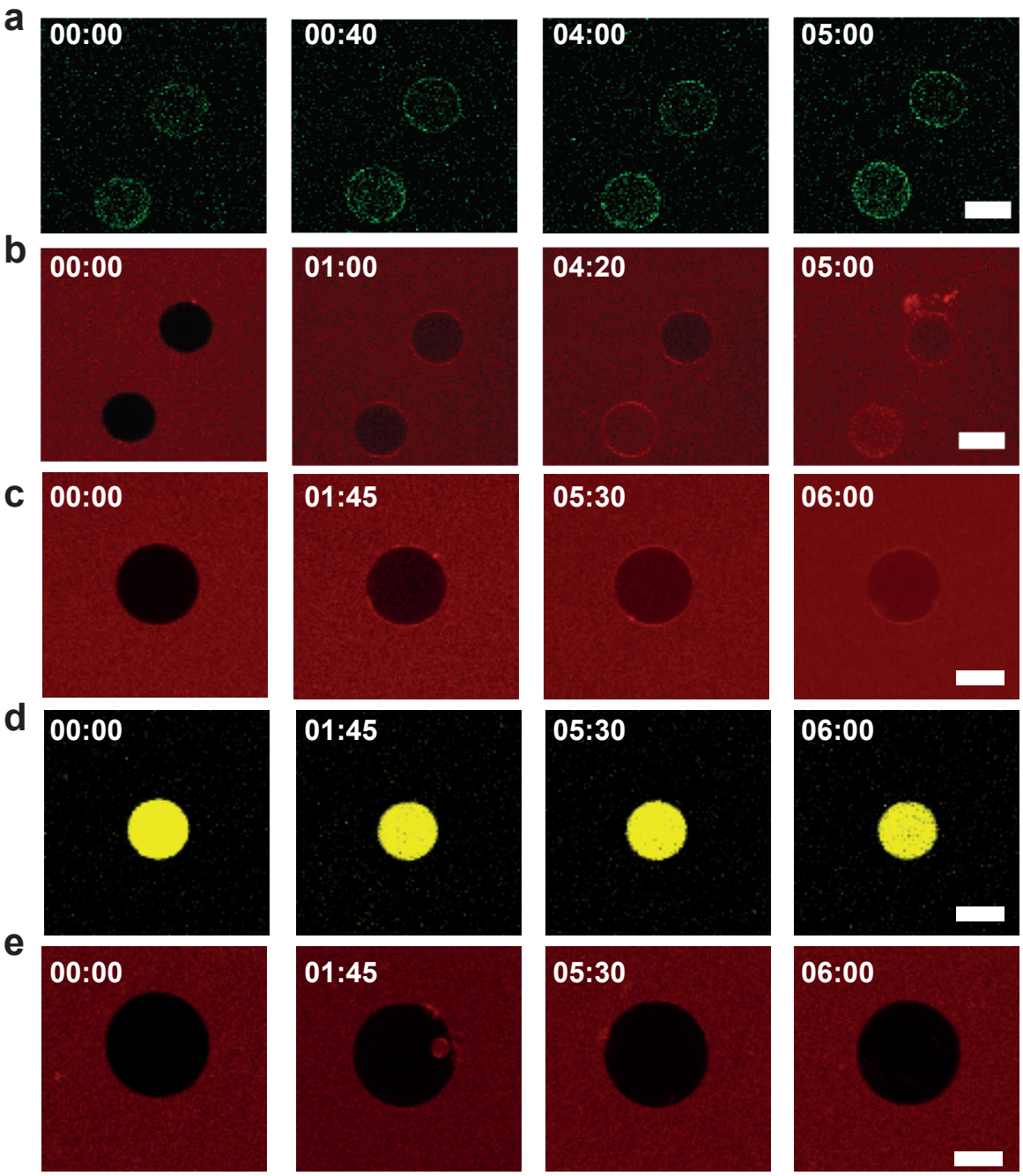

Figure 4.9: Dye influx assay with the encapsulated T pore. a) Time series obtained from fluorescent origami pores encapsulated within two vesicles. Note that fluorescently labelled origami pores are present at the vesicle boundary from t=0 (in contrast to the externally added origami T pores in Figure 4.8)b) Time series of dye influx (Atto 633) into the same vesicles as in (a), indicating membrane perforation by the encapsulated pores. c) Other example of confocal fluorescence images monitoring the pore-mediated influx of Atto 633. d) Time series monitoring the same vesicle as in (c) in the fluorescein channel, demonstrating that in contrast to Atto 633 the dextran conjugate cannot leak out. e) Control experiment in the absence of DNA origami channels showing no dye influx.

We also studied dye influx through DNA channels incorporated from the interior of the vesicles in an "inside-out" configuration (see Figure 4.9). As for the externally added pores experiments the origami channels were encapsulated into vesicles using inverted emulsion technique, which also resulted in a successful perforation of the membrane (see Figure 4.9 b, c). As also shown in Figure 4.9 d, while Atto 633 dye entered through the pores into the vesicles, encapsulated dye-dextran conjugates did not leak out. As previous shown, control vesicles are impermeable to Atto 633 (see Figure 4.9 e).

As visible in the fluorescence traces (see Figure 4.10 b (blue dots)) for externally added origami solution, after a time delay of t $\approx$ 1h, a sudden influx of Atto 633 into the vesicle is observed, which approximately follows exponential kinetics. The time delay corresponds to the waiting time between adsorption and first incorporation of one or several pores into the bilayer (see also Figure 4.8 a for experiments with dye-labeld pores). Using a simple model for dye influx, we estimated the number of incorporated pores for each vesicle from the ratio between the expected single channel time scale and the actually observed time scale: $N = \tau_{single}/\tau_{observed} = LV/(DA\tau_{observed})$. As expected, the number of pores increased with the vesicles' surface area (see Figure 4.11 a).

Furthermore, for encapsulated pores the influx follows exponential kinetics but in contrast to the externally added pores, there was no major time lag before membrane penetration (see Figure 4.10 d), which may be a result of the high concentration of nanopores within the vesicles. However, we observed a weak correlation between the number of pore and the membrane area for encapsulated T pores (see Figure 4.11 b), corresponding to a smaller number of simultaneously inserted pores. A time trace for a control vesicle is also shown (see Figure 4.10 b, d (grey dots)).

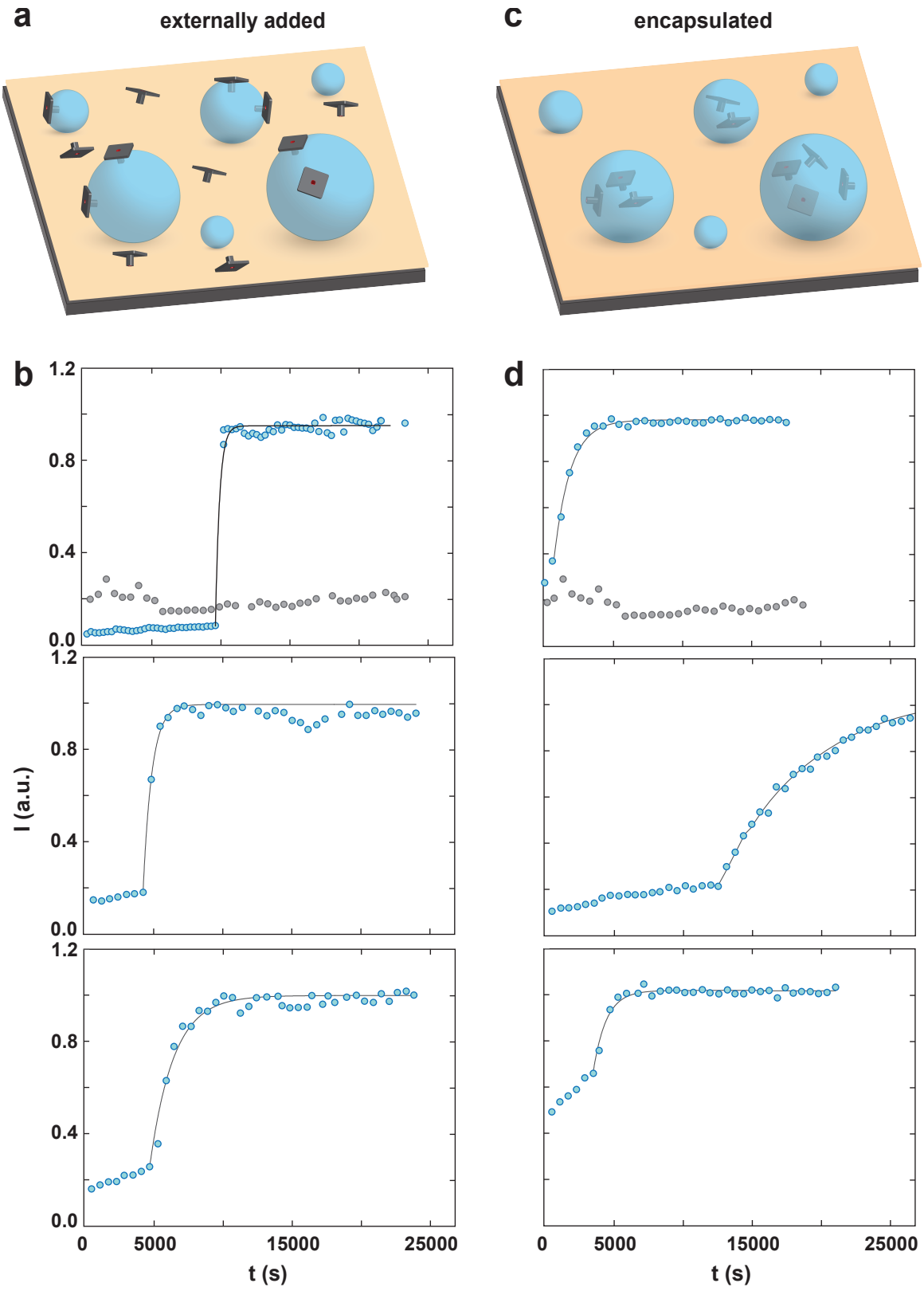

Figure 4.10: Vesicle dye influx. a) Schematic representation of externally added T pores penetrating a vesicle. b) Example traces demonstrating the increase of fluorescence inside the vesicles when modified T pores are added externally (blue dots). Control experiment in the absence of DNA origami channels showing no dye influx (gray dots). c) Schematic representation of T pores incorporated into a vesicle in an inside-out configuration. d) Fluorescence traces for encapsulated modified T pores. The traces are fit using an exponential model for dye influx (see Eq. 2.15)

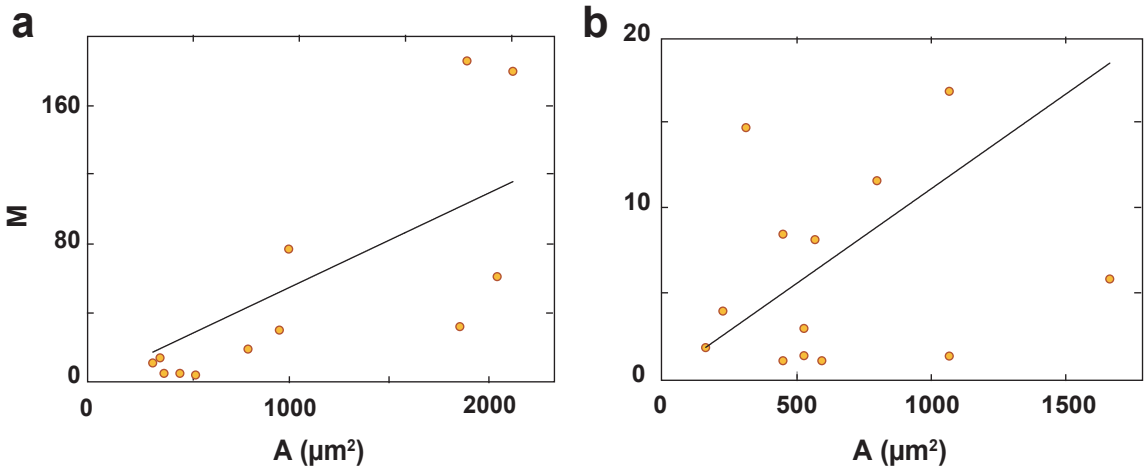

Figure 4.11: Dye influx statistical analysis. a) Number of pores, N, estimated from the influx rate using an exponential model for dye influx (Section 2.6.6) and plotted as a function of the surface area, A, of the corresponding vesicles. The line is obtained from linear regression analysis. b) Estimated number of pores, M, vs. vesicle area, A, obtained from time series recorded from vesicles with encapsulated pores. The number of incorporated pores is smaller and the correlation between M and A appears to be weaker than for externally added pores.

Results of the dye influx assay with the wheel pore are summarized in Figure 4.12. Both externally added (see Figure 4.12 a, b) as well as encapsulated (see Figure 4.12 c) pore experiments displayed successful dye influx.

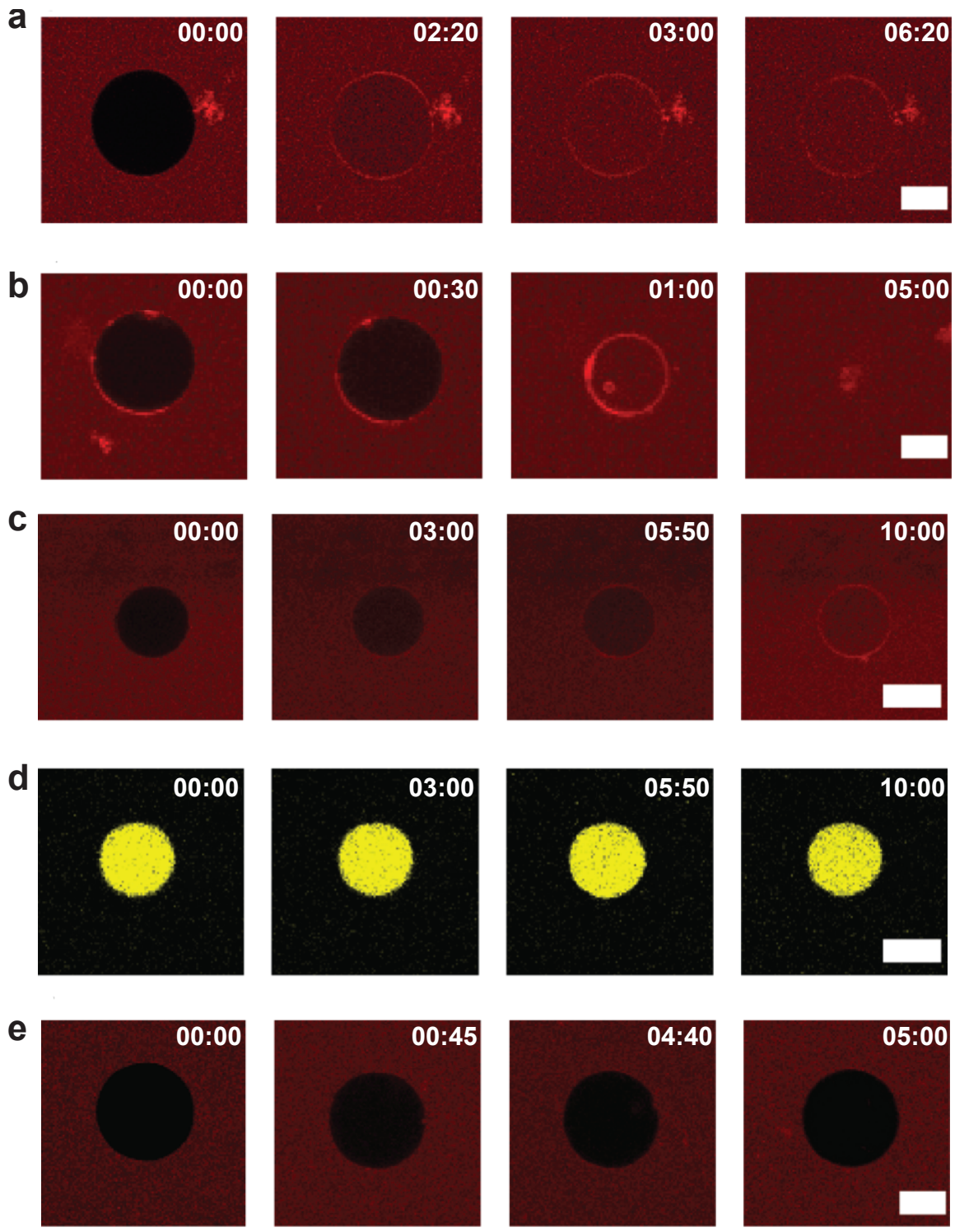

Figure 4.12: Dye influx assay using the wheel pore. a) Time series of dye influx induced by externally added wheel pores. b) Example for a time series with externally added wheel pores resulting in membrane destabilization. c) Time series of Atto 633 dye influx into a vesicle containing encapsulating wheel pores. d) Time series of the same vesicle, in which the fluorescence of a dextran-fluorescein conjugate was observed. e) Control experiment. In the absence of DNA origami pores the membrane is not permeable to the dye. Scale bar: 10 µm

In dye influx experiments with the pin pore filling of the vesicles with the external dye was not observed (see Figure 4.13). In contrast to experiments with SUVs (with a higher curvature), the pin pore does not appear to be able to penetrate GUV bilayer membranes spontaneously. Images recorded with fluorescently labelled pin pores (see Figure 4.13 a) demonstrate a complete coverage of the GUVs with the structures, most probably lying on the membrane with their long sides.

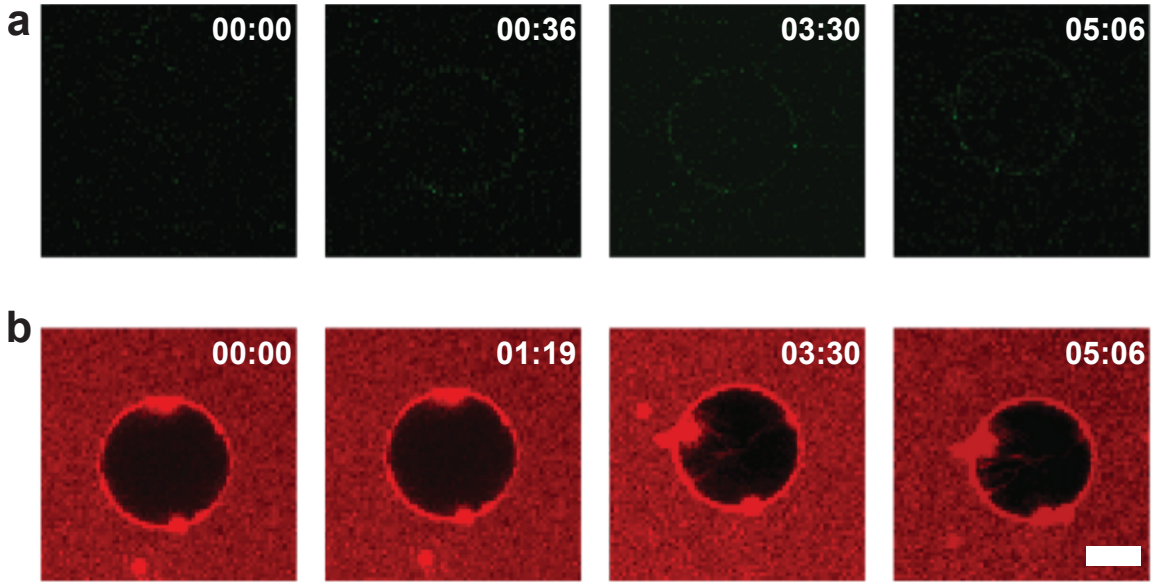

Figure 4.13: Dye influx assay using the pin pore. a) Time series observing binding of fluorescently labelled pin pores binding to the vesicle over time. b) Time series monitoring Atto 633 dye influx into the vesicle after external addition of the pin pore. Note growth of filaments on the vesicle over time indicating membrane destabilisation or deformation upon binding of pore. Dye influx is not observed. Scale bar: 5 µm

4.2 Electrophysiological experiments

4.2.1 Electrical characterization

In order to prove the membrane channel formation, we performed single-channel electrophysiological experiments [134]. Electrophysiological experiments were performed first on LB pores using an integrated chip-based set-up (see Figure 2.1 b) [9].

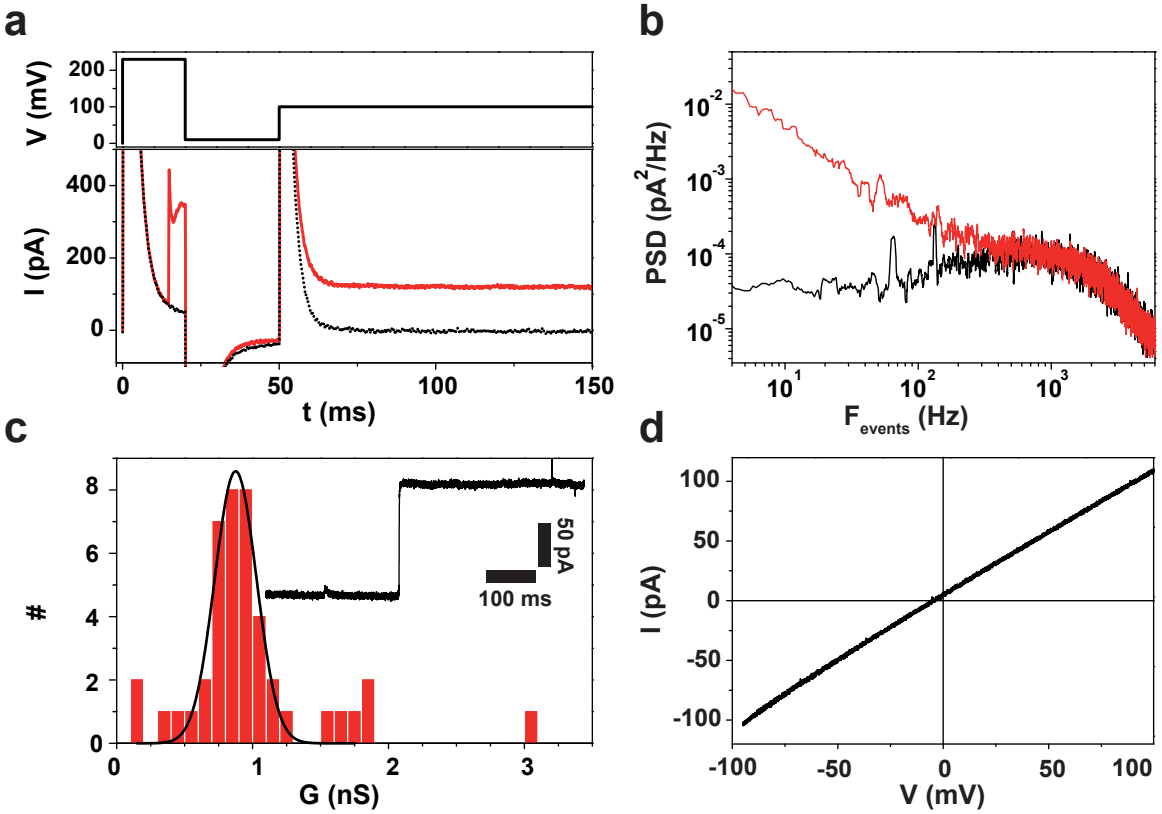

Figure 4.14: Electrical characterization performed on painted DPhPC bilayers on a chip-based electrophysiology set-up. a) Top: Voltage pulse used for incorporation of origami channels into the lipid membrane. Bottom: Corresponding current response before (black dots) and during incorporation (red line). b) Noise power spectra before (black line) and after the incorporation of a single origami pore (red line). Current traces were recorded at 100 mV at a filter frequency of 3 kHz. c) Histogram of channel conductances obtained from 43 incorporation events. The black line depicts a Gaussian fit. Inset: Stepwise increase in ionic current during an incorporation event at V=200 mV. d) Current-voltage dependence of the channel after incorporation.

Low concentration of LB pores (≈200 pM) were added to the *cis* side of the set-up and voltage pulses were applied to facilitate incorporation into membrane. As with biological channels, successful membrane incorporation of individual synthetic DNA channels manifested itself in a stepwise increase in transmembrane current (see Figure 4.14 a) along with an increase in electrical noise (see Figure 4.14 b). The synthetic DNA channels displayed

an average Ohmic conductance of G=0.87±0.15 nS (I=174 pA at 200 mV) per channel in a solution containing 1 M KCl and 2 mM $MgCl_2$ (see Figure 4.14 c, d). Occasionally large conductances were observed that corresponded to the presence of several channels in parallel (see Figure 4.14 c). TEM images confirmed that the DNA channels tends to aggregate in groups of two, three, four or more pores.

Electrical single-channel recordings were performed on wheel-, pin- and T pores as well. IV curves for analysed structures are presented in Figure 4.15, where all three pores show Ohmic behavior (see Figure 4.15 a, b, c), and because of similar size and shape the IV curves for a wheel (red) and pin pore (green) are comparable. As seen from the conductance histograms incorporation events are spread from 0.5 nS to 4.5 nS. Multiple incorporations were assumed for conductance higher than 2 nS. Single channel conductance was determined by fitting the histograms, where for all channels the conductance was surprisingly ≈1 nS. Similar conductances are expected for pin and wheel pore that share a 6HB (2.2 nm diameter) as a transmembrane channel, however the same conductance was measured for the T pore. By contrast, a slightly higher conductance of 1.6 nS was deduced from the gating steps (see Sec. 4.2.4).

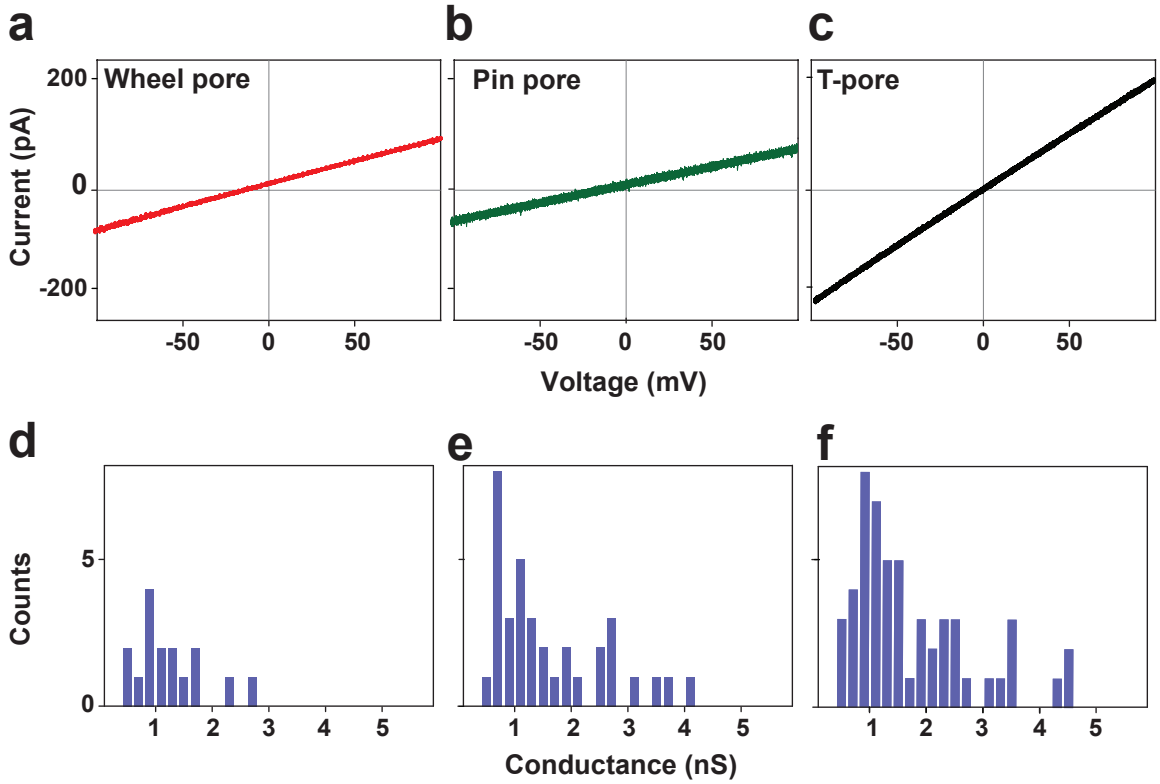

Figure 4.15: Electrical characterization of pin, wheel, and T pores performed on painted bilayers on a chip-based electrophysiology set-up. IV curves for a) wheel, b) pin and c) T pores. Incorporation histogram for d) wheel, e) pin and f) T pores.

Conductance measurements were also performed on the synthetic nanopores using the DIB. For the pin pore, we observed a conductance of G = 1.6 nS (see Figure 4.16 e, N=1), but the structure displayed a low incorporation frequency, which we attributed to its relatively small number of hydrophobic modifications (see Figure 4.17 a). By contrast, the wheel pore, with 57 hydrophobic anchors (see Figure 4.17 b), showed improved membrane interactions. We obtained conductance values around 1.5, 2.8 and 5.8 nS (see Figure 4.16 d, N=9). Thus, as before, we frequently observed insertion of multiple channels at the time and a correspondingly higher apparent conductance. Data analysis allowed us to extract a single channel conductance of G=1.7 nS, which is consistent with the dimensions of the channel and is similar to that of the pin pore. We therefore assume, that the conductance values around 2.8 nS correspond to two pores and the values around 5.8 nS correspond to four pores.

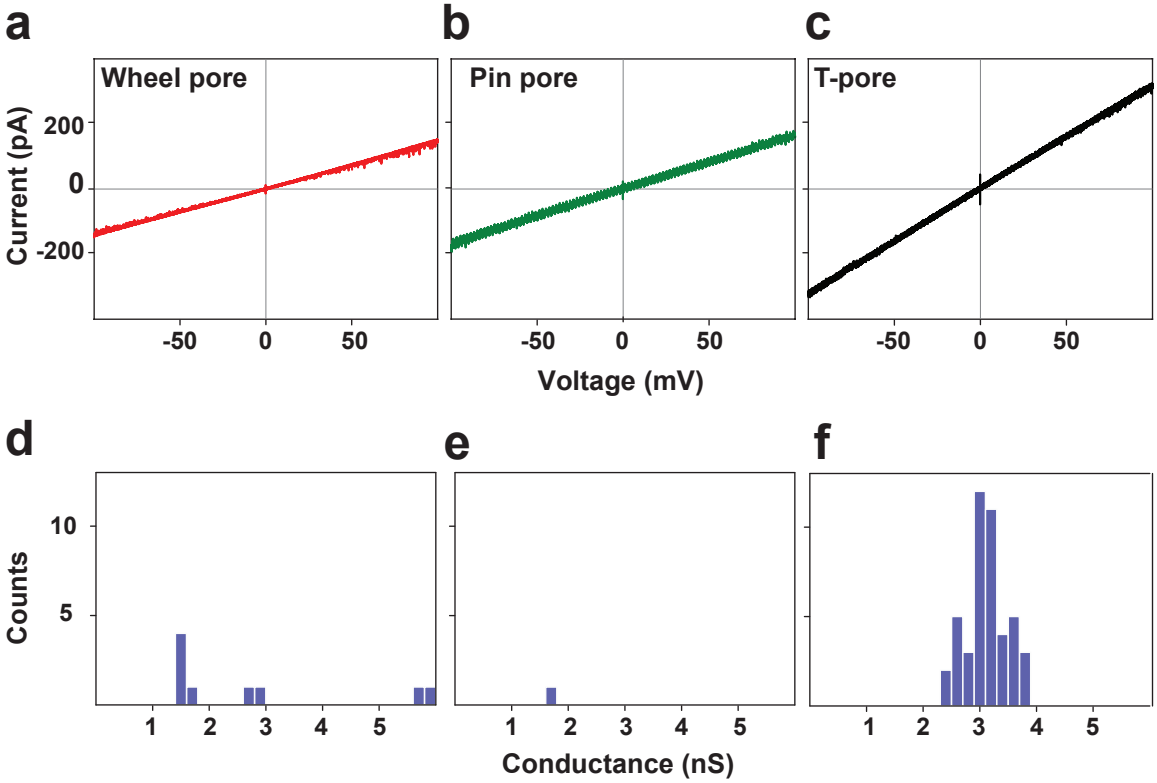

Figure 4.16: Electrical characterization on DIB. IV curve for a) the wheel, b) the pin and c) the T pore. Measured conductance values for d) the wheel, e) the pin and f) the T pore.

In comparison to the other pores, the T pore displayed a higher membrane insertion frequency, and its larger pore diameter resulted in a larger conductance value of G= 3.1 ± 0.3 nS (see Figure 4.16 f, N=45). Control experiments with DNA nanostructures lacking a membrane stem structure did not result in any measurable transmembrane current.

4.2.2 Conductance estimation of Origami channels

Conductance measured for LB, pin and wheel pores are close to that of αHL, which initially inspired the cap-stem structure for our DNA channel. For 1 M KCl, e.g., a conductance of

G=0.93 nS is measured for α-HL (I=112±3 pA for V=120 mV at T=21 °C) [110]. One has to note, however, that the physical properties of the DNA channel and αHL are quite different. αHL is shorter (10 nm including cap), narrower (1.4 nm at its central constriction), and less negatively charged, in addition the cap structure of the DNA channel appears to be leaky to the flow of small ions. Thus, presumably the combination of a variety of counter-acting effects coincidentally makes the DNA channel conductance similar to that of αHL.

A simple estimate for the conductance of a simple pore with length l, diameter d, and cross-sectional area A equals

$$G = \kappa(\frac{l}{A} + \frac{1}{d})^{-1} \tag{4.1}$$

Here the first addend corresponds to the contribution of the conductive channel itself, while the second addend accounts for the access resistance. For a 1 M KCl electrolyte, the conductivity κ is 10.86 S/m at T =25 °C [127]. The cross-sectional area of the pore determines the conductance value. The area for pores used for calculations are shown in Figure 4.17 a. The area for LB, pin and wheel pores is A_1. In case of the T pore, the stem area is masked slightly by the top layer, so that the lowest cross-sectional area A_2 through which ions has to pass equals the intersection of the stem area and the hole in the top layer. Experimentally, we find different conductance depending on the used set-up. For Orbit, a conductance of ≈1 nS was measured for pores with area A_1. For DIB a conductance slightly higher than calculated above was determined, supporting a higher leakage around the structure. It is also conceivable, that the central channel is actually slightly compressed and has a smaller diameter than the assumed 2 nm, but this effect might be overcompensated by leak current.

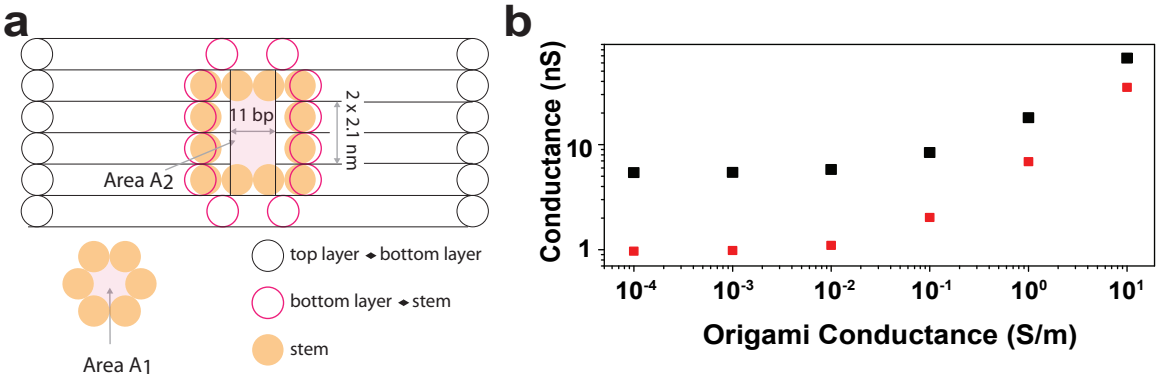

Figure 4.17: a) Cross-sectional channel area A_1 for LB, pin and wheel pore and A_2 for the T pore b) Simulated conductance across a LB (red), T pore (black) incorporated into a lipid bilayer for varying intrinsic origami conductivity at 100 mV bias voltage and 11 S/m bulk solution conductivity.

For the T pore with an area A_2, measured conductance on Orbit is 30% and for the DIB is 50% from the calculated conductance. Assuming a higher flexibility of the T pore stem due to square latice design, the membrane rigidity does influence the structure conductance.

As the influence of leaks on synthetic channels' electrical properties cannot be answered quantitatively at this point without more detailed structural studies. MD simulations predicted that the origami structure is not an insulator, and a strong ionic conduction along the DNA helices was detected [167, 168, 97]. In this context, we performed electric field calculations using Comsol. Here, the origami conductivity was varied from 10^{-4} S/m (insulating)

to 10 S/m in order to screen the influence on channel conductivity. Figure 4.17 b shows the results of the simulations for LB (red) and the T pore (black). As expected, the calculated channel conductance coincides with that of a simple geometrical model for the limit of zero origami conductivity. For origami with conductivity values of 10^{-1} S/m (corresponding to 1% of the bulk solution conductivity), a considerable increase in channel conductance is observed ($G_{\kappa_{DNA}=10^{-1}}$ S/m). In the bulk solution limit, the channel conductance corresponds to a channel with a length equal to the lipid bilayer thickness and a diameter equal to the stem's outer size.

Table 4.2.2 shows experimentally determined conductance for Orbit and DIB set-ups, estimated conductances using a simple model and simulated conductane considering origami conductivity of 10^{-1} S/m.

	G_{Orbit}(nS)	G_{DIB}(nS)	G_{moldel} (nS)	$G_{\kappa_{DNA}=10^{-1}S/m}$(nS)
LB	0.87 ± 0.15		1.02	2
pin	1.1 ± 0.2	1.6	1.14	
wheel	1.1 ± 0.2	1.7	1.69	
T pore	1.6 ± 0.2	3.1 ± 0.3	5.8	10

Table 4.1: Channel conductance comparison

4.2.3 Incorporation mechanism

The molecular mechanism of membrane insertion of our DNA channels so far is not understood, no molecular dynamics studies are available that correspond to this case. It has been shown previously in several cases that in principle penetration of of large, charged molecules through a bilayer can occur. For instance, hydrophilic (charged) HIV-1 TAT peptides were shown to spontaneously translocate through zwitterionic phospholipid bilayers [67], involving large membrane fluctuations and lipid rearrangements. Similar processes have been observed in MD simulations for translocation of the peptide penetration [165] through the lipid bilayer. In case of the DNA channel we assume that the lipids can re-arrange dynamically with the hydrophilic heads facing the stem of the structure. Otherwise the energy cost associated of inserting a DNA channel into the hydrophobic core of the membrane without rearrangement of the lipids would be extremely high (already the insertion of a single monovalent ion would cost several eV (or several 100 kJ/mol) according to the Born model).

In order to be able to insert a hydrophilic channel into a lipid membrane, a potentially high activation barrier first has to be surmounted. The height of this barrier will depend on the lipid type (or lipid composition for mixtures), the curvature of the membrane, the presence of phase boundaries or defects within the lipid bilayer [108, 105]. Membrane defects can be created thermally, by chemical or electrical gradients, or by mechanical tension [105]. Membrane binding molecules are in fact thought to preferentially insert at such defects and phase boundaries [122, 20].

The free energy cost of a defect of radius R in a bilayer membrane is typically estimated to be $E = 2 \cdot \pi \cdot \gamma_L \cdot R - \pi \cdot \gamma_S \cdot R^2$, where γ_l is the specific line tension of the lipid membrane and γ_S is its specific surface tension. A defect exceeding a critical size $R_c = \gamma_L/\gamma_S$ will actually continue to grow, whereas smaller defects tend to reseal. We here estimate the energy cost for formation of a small hole conservatively by keeping only the linear term which dominates for small R, i.e. by $E \approx 2 \cdot \pi \cdot \gamma_L \cdot R$. Experimental and theoretical values for γ_L lie in the range of 5 - 40 pN [164]. To accommodate a six helix bundle of diameter 6 nm would therefore cost less than $\approx$ 100 - 800 pN nm $\approx$ 25 - 200 k_BT. This is compensated

by the free energy gained from binding of the cholesterols to the lipid membrane. Insertion of a single cholesterol from solution into a lipid bilayer results in an energy gain of order 20 - 25 k_BT [85]. As the hydrophobic modifications are concentrically arranged around the stem (see Figure 4.2), the maximum number of hydrophobic insertions is achieved, when the stem points perpendicularly through the membrane. In addition, positive charge of the zwitterionic PC headgroup may directly interact with the negative phosphate, whereas electrostatic interactions between the negative lipid charge and the phosphate backbone may be mediated by Mg^{2+} ions presented in DNA channel solution [122, 58].

In our work two different types of lipid bilayer membranes were used: POPC lipids were used for the fabrication of small unilamellar vesicles (SUV), EggPC for the GUV while DPhPC lipids were used for the electrophysiological measurements. This choice was made as POPC and EggPC provided better SUV and GUV's samples, while DPhPC provided more stable suspended bilayer membranes, which are better suited for long-term electrophysiological measurements, and which sustained higher voltages. POPC, EggPC and DPhPC are quite different in their physical properties: POPC is a phospholipid with an unsaturared fatty acid chain and is in the liquid disordered state in our experiments, EggPC is a natural lipid and contain a mixture of lipids, DPhPC is a fully saturated lipid and is known to form very stable lipid membranes. In fact, we seem to observe spontaneous insertion into the lipid bilayer only for POPC and EggPC lipids, whereas for DPhPC bilayers the additional application of voltage pulses is required. It seems likely that for the "more fluid" POPC and EggPC bilayers, thermal fluctuations are sufficient to promote insertion of the stem into the membrane, whereas the energy barrier for spontaneous insertion into DPhPC layers is too high. Furthermore, as is also well known from pore forming proteins, insertion into SUVs is actually easier than insertion into large vesicles or membranes [78], which may be attributed to a larger separation between the lipid headgroups due to the curvature of the SUVs. One of the main problems of our synthetic pores remains the relatively low success rate of membrane incorporation and the strong batch-to-batch variations. In addition incorporation probability seems independent of the used hydrophobic molecules, we did not observe any major difference between tocopherol and cholesterol anchors.

4.2.4 Origami channel gating

Synthetic DNA channels displayed gating behavior similar to the stochastic "gating" of biological ion channels (see Sec. 4.2.4). Gating is divided into three categories: total channel closure, short-lived and lower-amplitude events called sub-conductance events [14] and baseline sub-states. We chose two pores and performed a careful analysis in order to understand the gating behavior. Voltage-dependent gating analysis was performed on T pores using Orbit and DIB set-ups.

Figure 4.18 a shows a total closure of the pore, which was triggered over 125 mV. The graph suggest the simultaneous presence of three pores in the lipid membrane. Every step was measured and plotted in a histogram for 125 mV and 150 mV (see Figure 4.18 b). Gating steps, for the T pore on the Orbit corresponds to the single channel conductance of 1.6 ± 0.2 nS. Remarkably, this gating behavior was not observed for experiments performed on the DIB.

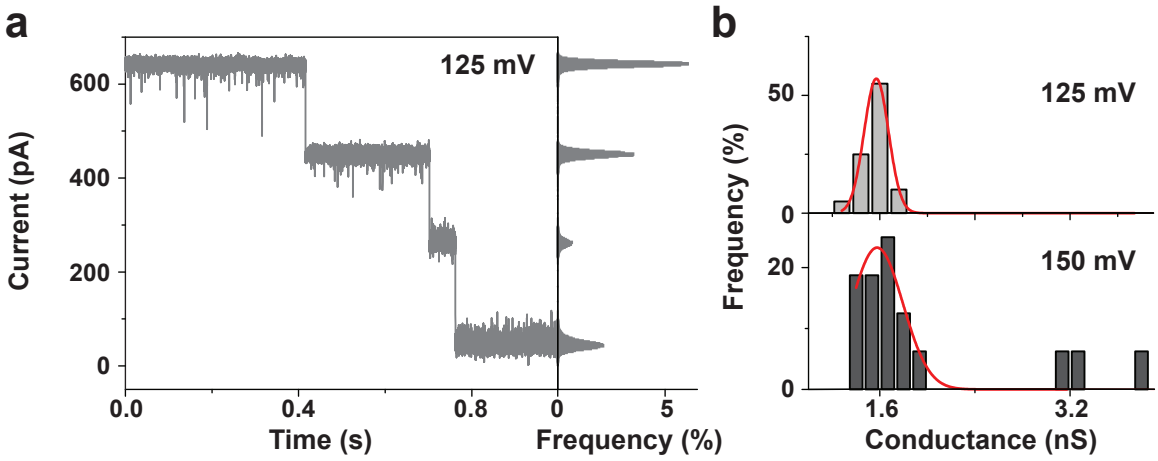

Figure 4.18: a) Gating steps for T pores, recorded at 125 mV. b) Histogram over several closing steps for 125 mV and 150mV. The conductance for one channel corresponds to 1.6 ± 0.2 nS

Figure 4.19 a depicts the current traces recorded at 100 mV for T pore on Orbit (pink) and DIB (blue). In contrast to the total closure, both set-ups display sub-conductance states. As mentioned above, we assumed the simultaneous incorporation of three pores in the lipid membrane for the Orbit. We measured similar current in case of the DIB, but assigned it to one channel, as we did not observe any closure there. Figure 4.19 b shows scatter plots of the current change versus the dwell-time of the closure states. A slight increase of frequency was observed for both set-ups (see Figure 4.20 a). In the Orbit a voltage dependence was observed for the event frequency up to 100 mV while at 125 mV and 150 mV, the events frequency rises. Our first assumption is that at voltages higher than 100 mV, recorded events are a mixture of sub-conductance states and total channel closure. The experiments performed on the Orbit showed current reductions of $\Delta I/I_0$ from 30% to 100%, considering I_0 as one third of the measured current. The corresponding lifetimes are in the range of 0.1 ms and are voltage independent (see Figure 4.20 b).

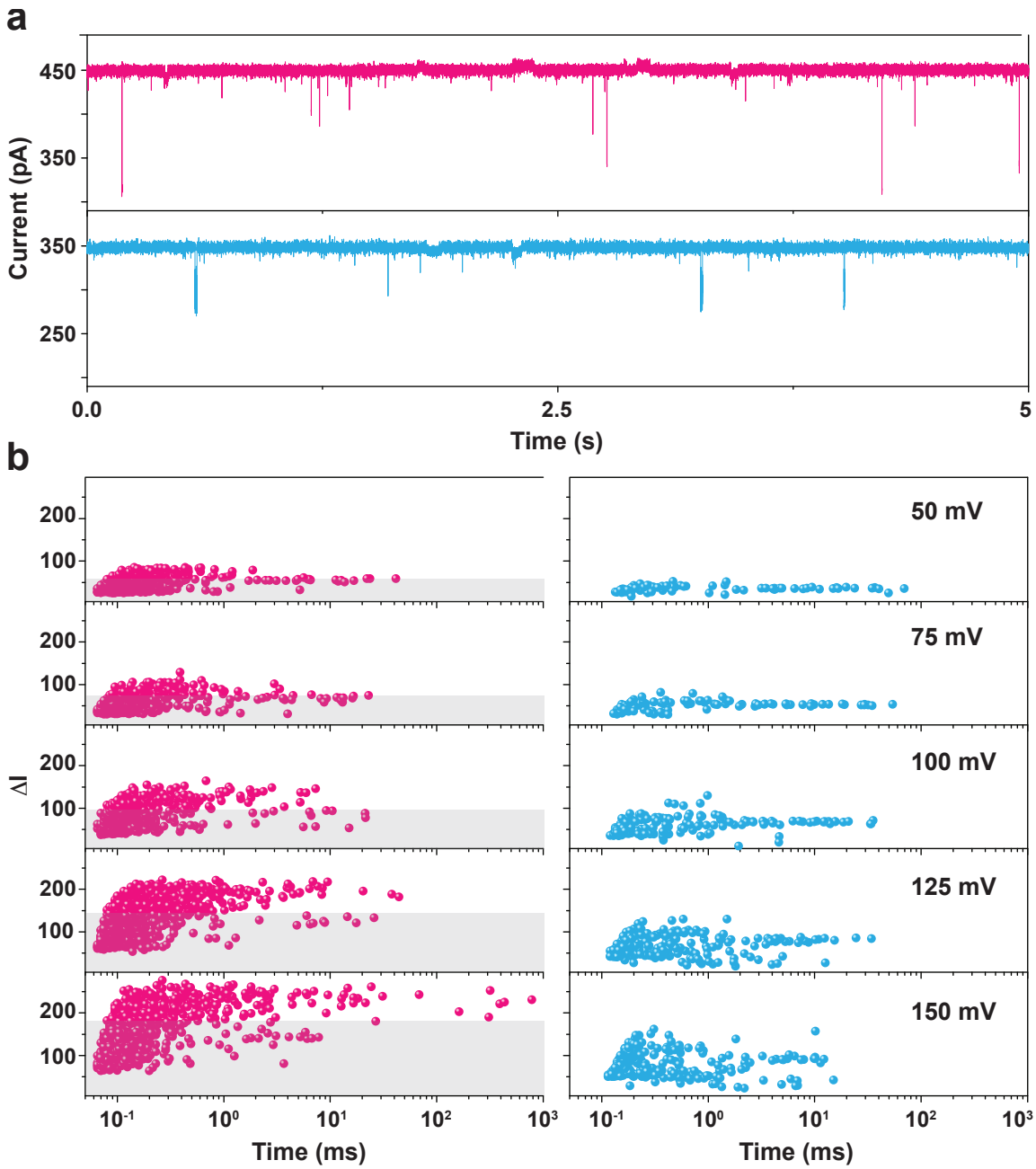

Figure 4.19: T pore gating behavior for Orbit vs DIB set-up. a) Example of traces for Orbit (pink) and DIB (blue). b) ΔI vs lifetime scatter plots for T pore recorded on Orbit (pink) and DIB (blue).

As visible in the scatter plots (pink), two events populations are present. At lower voltages, both populations strongly overlap, while at 125 mV and 150 mV the second population becomes prominent. The border between Pop_1 (population 1, faded colour points) in Figure 4.19 b and Pop_2 (population 2) is considered at $\Delta I/I_0$=70%. Pop_1 contains all events between 0 and 70 %, and Pop_2 contains all events between 70 and 100 %.

At 50 mV Pop_1 contains 80 % of events, but at 150 mV, the number of events reduces to 55%. Pop_1 dwell-time is ≈100 µs and appears to be voltage independent. The lifetime of Pop_2 shows a voltage dependence, with the time constants, increasing from 80 µs at 100 mV

to 170 µs at 125 mV and 190 µs at 150 mV. Apparently, the closure time of Pop_2 increases slightly with increase in voltage, indicating the coupling of the closure events to electrostatic forces. Dwell-time histograms are fitted using a single exponential. In this case, the result is influenced by fast events, and the events slower than 0.3 ms do not contribute much as expected. In order to analyze long-lived events, a time rate unit was introduced that is created by the ratio of the overall time that the pore spends in one state and the total recorded time (t_{states}/t_{total}). The lifetime is dominated by short-lived events, in contrast to the time rate which is dominated by long-lived events. As expected, the time rate is voltage dependent, increasing from 0.0011% at 50 mV to 2.2% at 150 mV (see Figure 4.22 c).

The same experiment was performed with T pores on the DIB (see Figure 4.19 a blue trace). The relative current reduction ($\Delta I/I_0$) is between 10 to 30% of the open current. As described in Sec. 4.2.1, the single channel conductance measured on DIB is twice as high as for the Orbit. In this case the I_0 will be considered 350 pA at 100 mV. For these experiments the event frequency is slightly higher with applied voltage (see Figure 4.20 a). The lifetime (≈0.3 ms) and time rate (≈10%) are slowly decreasing with voltage. These findings suggest that the sub-conductance states detected on DIB have other sources. One assumption is that translocation of unfiltered staples was recorded, due to technical reasons dilution was not possible for the DIB. A counterargument for this hypothesis is the high lifetime (0.3 ms) of the sub-conductance events. As will be described later in Sec. 4.2.5 a lifetime of 0.15 ms was obtained for 500 bases ssDNA in 2 M KCl at 100 mV. Although the maximum staple size is 50 bases (10 times shorter), the lifetime is twice as was measured for 500 ssDNA bases. Another idea is that the staples could hybridize to each other in solution and translocate as dsDNA, though the staple concentration is low in filtered origami solution.

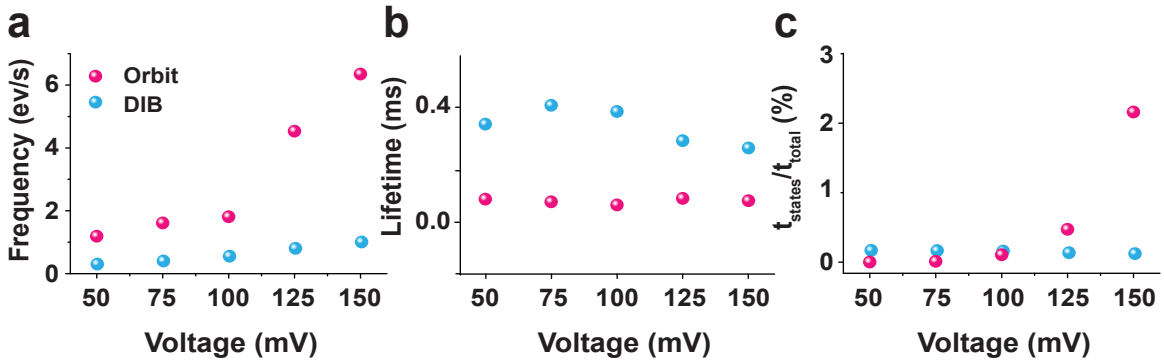

Figure 4.20: T pore gating voltage dependence for Orbit (pink) vs DIB (blue) set-up. Scatter plots for a) Event frequency b) Lifetime c) Time rate percentage.

In addition to clear, visible sub-conductance events, individual T-channels displayed distinct baseline switching (see Figure 4.21 top). For a better understanding of these baseline levels, Hidden Markov Model (HMM) analysis was performed on channels showing small sub-states. The color coded trace (see Figure 4.21 bottom) reveals three types of events: type I (green), type II (blue) and type III (red). The cumulative histogram was fitted, using Eg. 2.2 as seen in Figure 4.22 a and the lifetime of these events were determined.

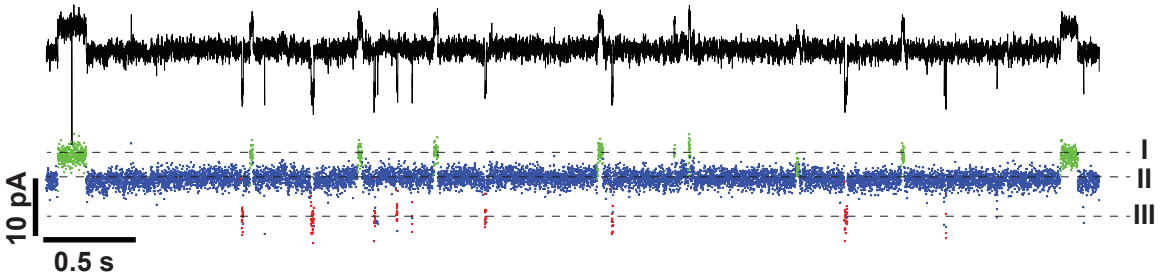

Figure 4.21: Example traces for a T pore presenting baseline sub-states (black). Detected events using HMM, the blue region (type II) represents the most probable state and the green (type I) and red levels (type III) are secondary states. Experiment was performed at 100 mV.

Figure 4.22 compares all three states by their lifetime, frequency of appearance and time rate percentage. Type II events occurs most frequently, and the lifetime for all voltages is 400 ms and the state is present 95% of the recorded time. Type I events are slightly less frequent than type III events but have a longer lifetime (30 ms). As shown in Figure 4.22 b-d all plotted results are voltage independent.

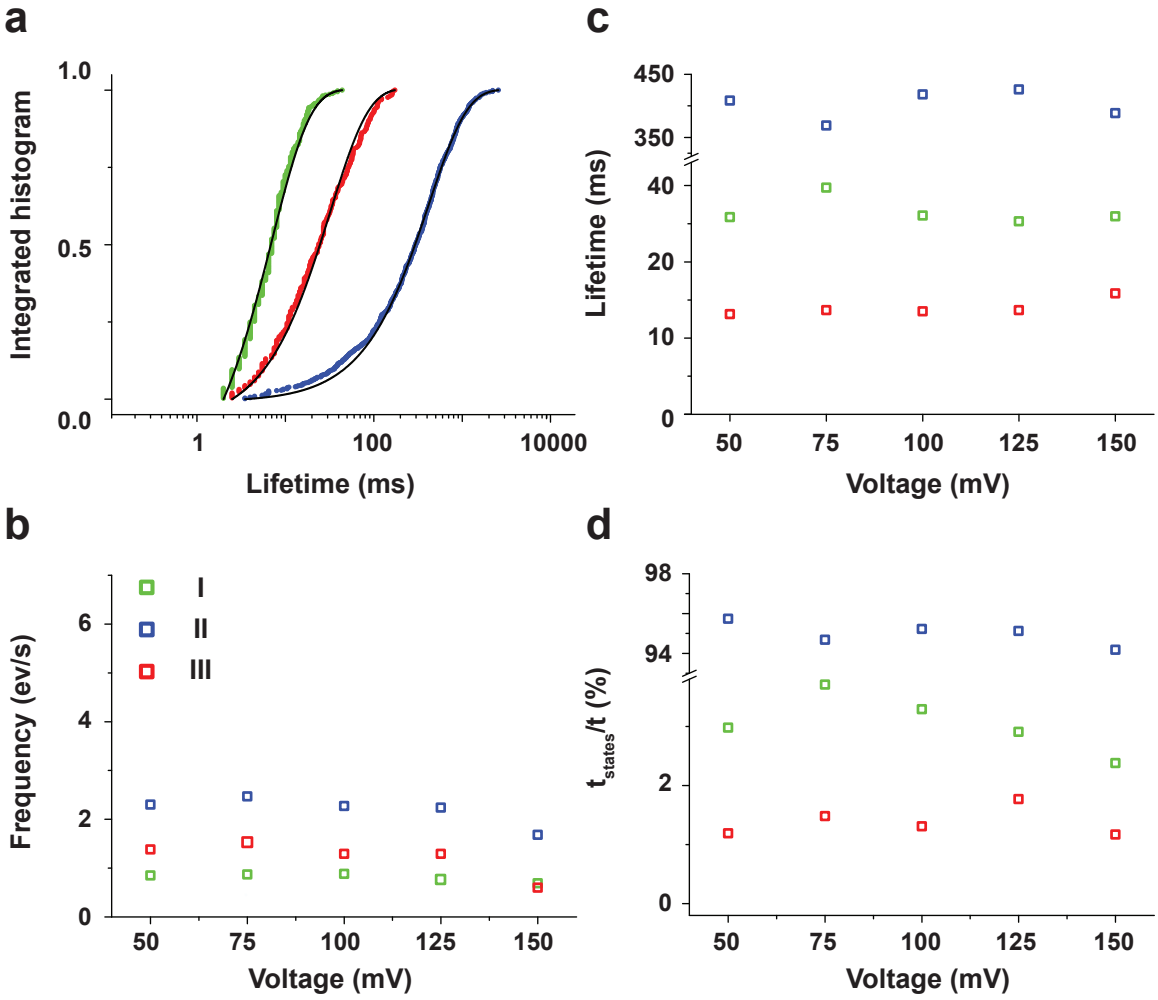

Figure 4.22: Baseline sub-states voltage dependence a) Cumulative lifetime distribution for all observed types of states, type I (green), type II (blue) and type III (red). The solid lines are the fits with Eq. 2.2. Scatter plots for b) States lifetime versus voltage c) Events frequency d) Time rate percentage.

Analysis of gating behavior of the T pore suggests that the gating has different sources, states that are voltage dependent or independent. The gating behavior is set-up specific. DNA pores recorded on DIB revealed no total channel closure.

Baseline sub-states are observed for both set-ups, but a HMM analysis was possible only for the Orbit. Here, type I, II, III events presented no voltage dependency for any of the analyzed parameter.

At first glance sub-conductance states were present for both set-ups, but a careful analysis revealed different behavior. For the Orbit, events frequency and the time rate percentage increased with voltage. After breaching 100 mV, sub-conductance events became a combination of fast flickering caused by certain effects connected with the T pore and a total closure caused by the membrane properties. Short-lived sub-conductance events (Pop_1) appeared to be caused by modifications in the T pore, - that is unzipping, either by rezipping of short double-helical DNA domains in the channel or by channel deformations. Longer-lived and deeper events (Pop_2) are slightly voltage dependent and become more pronounced at higher

voltages. In the DIB the lifetime and the time rate percentage decreases with voltage as it is to be expected for DNA molecule translocation. But due to a long dwell-time, staple translocation is excluded.

To test whether unzipping of staples causes gating we designed LB "Mutant" channels that differed from the "Wild type" channel only by a single-stranded heptanucleotide which was not incorporated into the main origami structure. We studied two channel mutants - for modification M_1 and M_1^* the heptanucleotide pointed into the central channel (see Figure 4.23 a). For modification M_2 the staple extension was oriented away from the central stem, pointing into one of the neighboring holes of the stem (see Figure 4.23 b). M_1 and M_1^* contain different bait sequences: M_1 (sequence TTTCCGG) and M_1^* (AAAAAAA). These modifications could fluctuate, block the channel, or one could act as a "handle" for the electric field, leading to partial unzipping of a DNA staple strand.

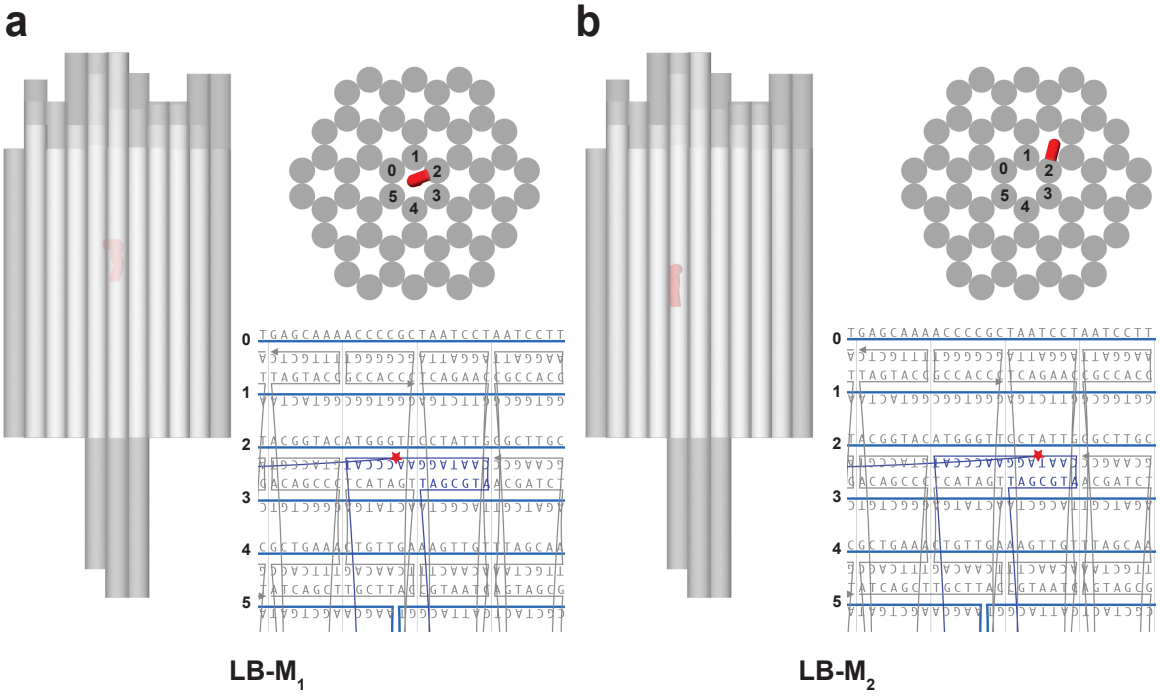

Figure 4.23: Scheme of mutant LB channels. Mutations strands are represented in red, LB side view, top view and a zoom in the cadnano file. a) LB-M_1 and LB-M_1^* with the bait pointing into the central channel. b) LB-M_2 pointing in one neighboring channel.

Here, LB presents similar gating behavior as the T pore, even though the shape and the conductance are totally different. As for the T pore at high bias voltages, the channels underwent full closure as seen in (see Figure 4.24). The closure steps histogram is fitted and steps size corresponds to the single channel conductance of 0.9 nS. To be noted, the total closure is triggered at a higher voltage that is inquired for the T pore.

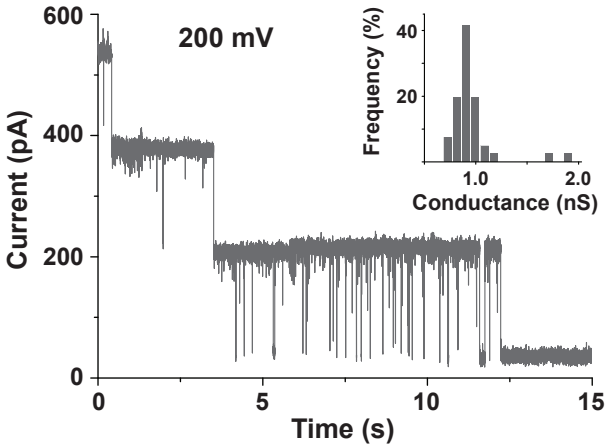

Figure 4.24: Total closure of the LB. Time course of the ionic current across the lipid bilayer with multiple origami channels incorporated at 200 mV bias voltage. Inset histogram over several closing steps show a conductance of 0.9 ± 0.1 nS. Simultaneous closing of two channels were recorded.

At lower voltages we typically observed fluctuations with amplitudes (ΔI), corresponding to fractions of a single-channel conductance. Figure 4.25 shows scatter plots of conductance change vs. channel closure time for an unmodified DNA channel (LB-WT) structure recorded at 100 mV. The scatter plots reveal that the sub-conductance states have different statistics in comparison with the T pore. In order to compare all the experiments, the baseline conductance was calibrated with the conductance of a single channel.

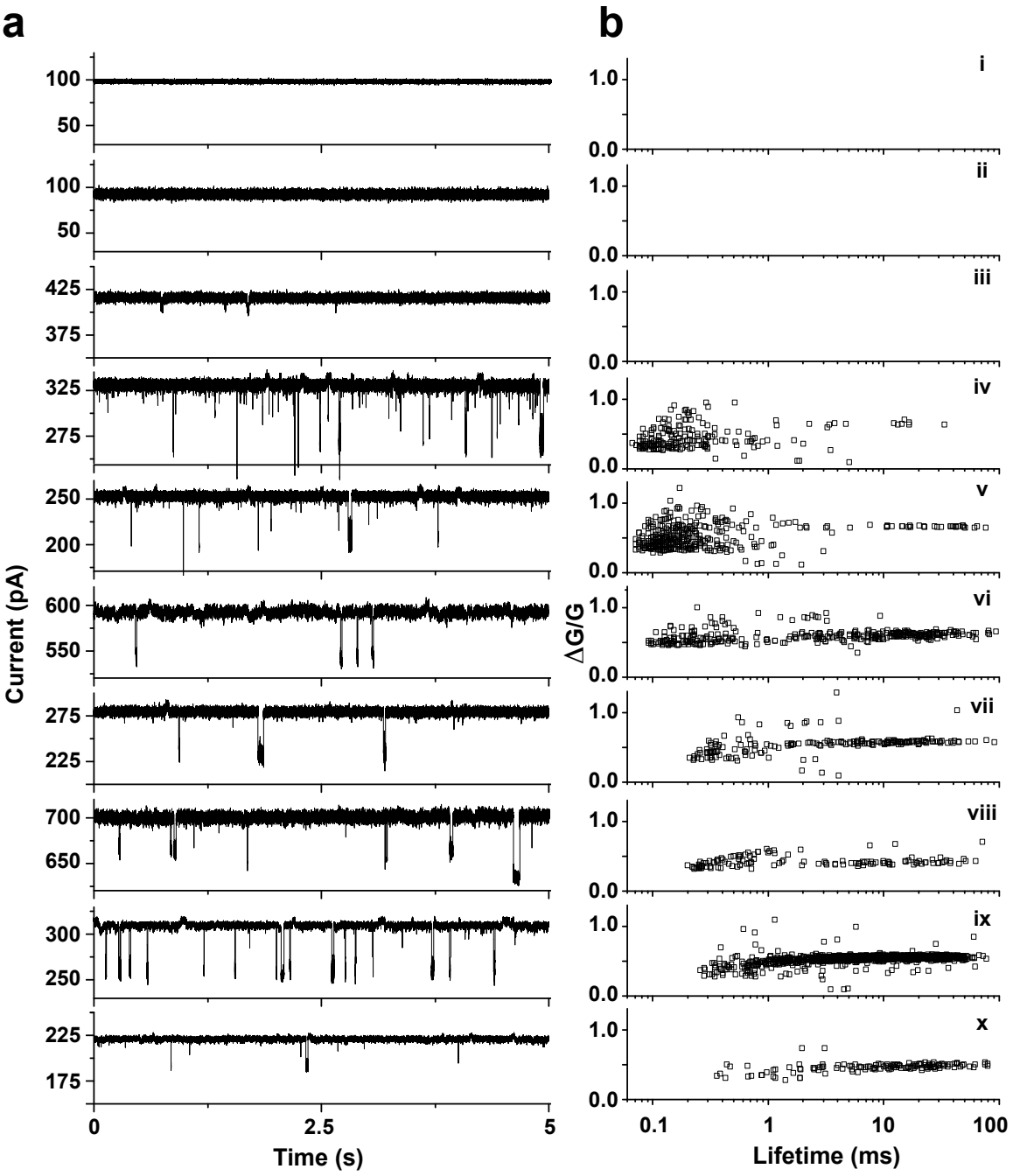

Figure 4.25: Sub-conductance states for WT origami channel a) Typical current traces obtained from LB-WT channels. b) Scatter plots of the relative conductance change versus dwell-time for the closure states origami channel. Each data point corresponds to a single closing event.

The first three experiments presented for LB-WT exhibit no gating behavior. These channels were used to perform DNA translocation experiments. Sub-conductance states for experiments number iv to vi show similar signatures, and their scatter plots shows two populations. Pop_1 is faster than 1 ms with an average dwell-time of 100 µs and has a broader amplitude range and Pop_2 is long-lived with a dwell-time higher than 12 ms and an amplitude of 45%. From graph vii the Pop_2 increases its presence probability, from 7% to

90%. Events frequency for these traces vary from 0.3 ev/s to 5 ev/s (see Table 4.2 LB-WT). These variations suggest that sub-conductance states have different sources.

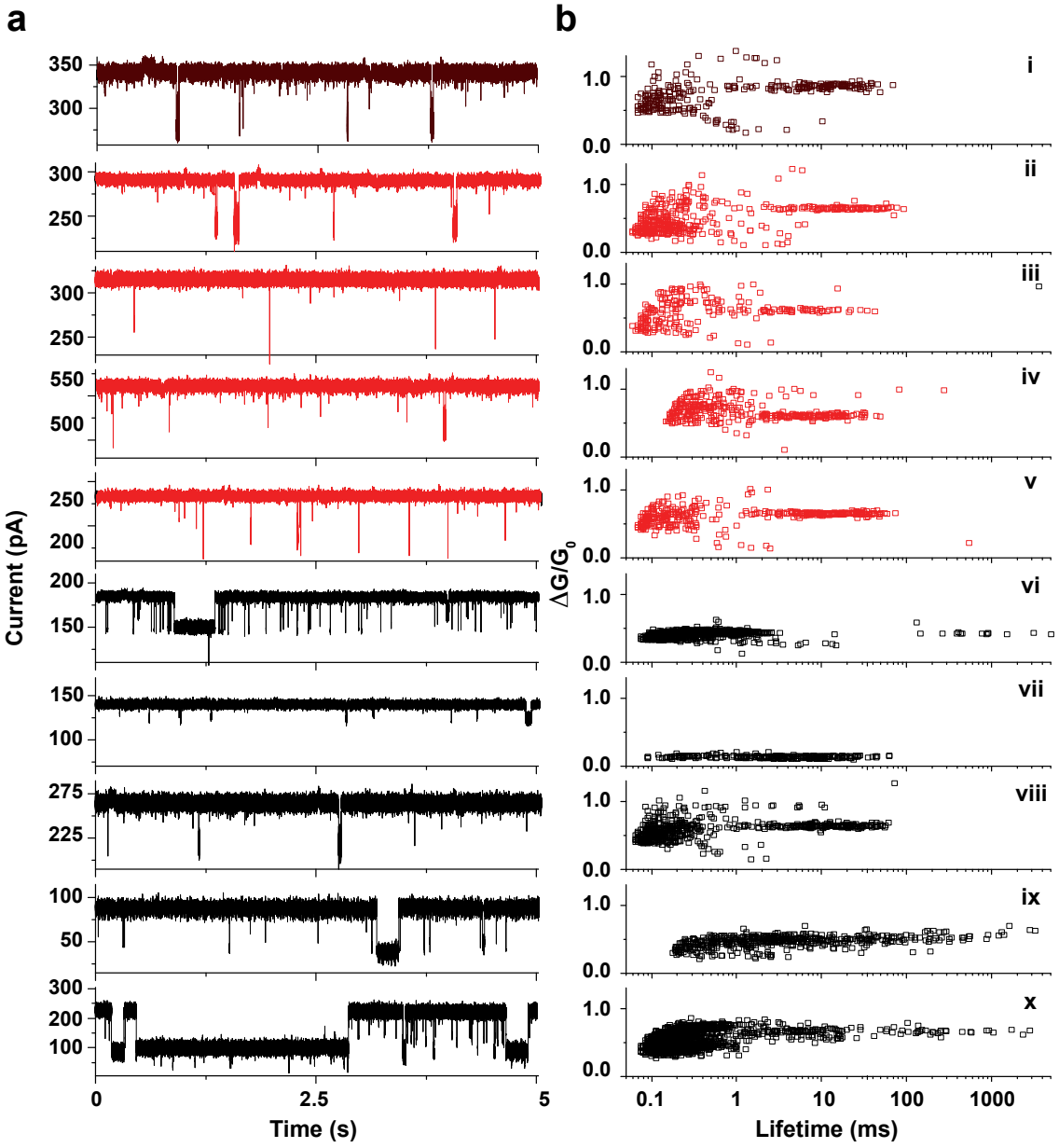

Figure 4.26: Sub-conductance states for LB-mutant origami channel. a) Typical current traces. b) Scatter plots of the relative conductance change vs dwell-time for the closure states of i a channel with modification sequence (AAAAAAA) on site M_1, ii-v with modification (sequence TTTCCGG) on site M_1, vi-x with a modification on site M_2 with different sequence (TTTCCGG) at 100 mV bias voltage.

In contrast with the LB-WT, LB-M_1 and LB-M_2 show sub-conductance states for every recorded channel (see Figure 4.26), whereas many of the unmodified DNA channels showed no gating at all (such as current trace i-iii in Figure 4.25).

As seen in figure 4.26 i-v, for M_1^* and M_1 modification (heptanucleotide pointing into the central channel), two populations occurred. One population is defined by a broader $\Delta G/G_0$ and lifetimes between 80 µs and 250 µs and one with a with an average dwell-time of 17 ms with two exceptions for experiment iii (5 ms) and v (9 ms), and with a blockade amplitude of 45 %. As for T pore the time rate was calculated, for M_1 the pore spends in the sub-conductance state $0.56 \pm 0.04\%$. As expected the M_1^* has the same time rate, 0.57%. The event frequencies are similar for all experiments and range from 0.6 to 1 ev/s. Pop_1 contains 53 to 75 % of all recorded events. M_1^* (i) mutant exhibits very similar sub-conductance statistic as M_1 (ii-v), suggesting that the sequence of the bait does not influence the sub-conductance behavior.

For the M_2 mutant, the additional staple pointing away from the central stem does not lead to a reproducible event distribution. Notably, experiment viii shows similar event statistics as the M_1 mutant. The average dwell-time for Pop_1 is 100 µs and 15 ms for Pop_2. The event frequency is 0.8 ev/s and Pop_1 contains 67 % of all events. For experiments vi and x the percentage of Pop_1 ranges between 24 to 92 % and the event frequency is 5 ev/s, which is higher in comparison to M_1. Experiment vii display different event statistics and signatures.

Events frequency, Pop_1/Ev (%), lifetime of Pop_1 and Pop_2 and the time rate percentage are summarized for LB-WT, LB-M_1, LB-M_1^* and LB-M_2 in table 4.2. Consistent results are obtained for LB-M_1, LB-M_1^*, the event-frequency of ≈0.8ev/s, the Pop_1/Ev rate is ranged between 53 and 75%, the time rate percentage is ≈0.5% with exception of experiment iii, the τ for both populations are slightly varying, τ_{Pop_1} is between 80 and 250 µs and τ_{Pop_2} is ≈16 ms with two exceptions. Events lifetime (τ) are error prone due to the arbitrary fixed border between populations and in some cases events number reduced.

In contrast to the LB-M_1 and LB-M_1^*, results obtained for LB-WT and LB-M_2 are inconsistent and the events frequencies vary for LB-WT from 0 to 5.7 ev/s. The Pop_1/Ev rate is between 7 and 92%. The time rate percentage for LB-WT is ≈0.56% with one exception of 4% in contrast to the LB-M_2 where the t_{states}/t_{total} increases from 0.41 to 24.3%.

Channel	Frequency(ev/s)	Pop_1/Ev (%)	τ_{Pop_1} (µs)	τ_{Pop_2} (ms)	t_{states}/t_{total}
LB-WT					
iv	5.0	90	91		0.48
v	1.3	86	83		0.39
vi	0.7	36	152	16.0	0.72
vii	0.5	31		13.0	0.47
viii	1.0	45		12.5	0.88
ix	3.2	7		14.8	4.04
x	0.3	8		19.9	0.44
LB-M_1^*					
i	1.0	55	117	15.3	0.57
LB-M_1					
ii	1.1	75	82	16.8	0.58
iii	0.6	69	125	5.4	0.14
iv	0.9	53	249	8.7	0.49
v	0.6	53	110	17.5	0.54
LB-M_2					
vi	5.7	92	264		0.57
vii	0.9	24		8.8	0.66
viii	0.8	67	108	15.5	0.41
ix	4.6	30		4.6	24.3
x	2.1	88	184	6.1	5.73

Table 4.2: Sub-conductance states summary for LB-WT, LB-M_1 and LB-M_2 at 100 mV.

For some LB-WT channels the sub-conductance events are absent which indicate that the scaffold loops dangling on the top of the channel were not responsible for those events. As a control, experiments were performed at negative voltage (see Figure 4.27). Sub-conductance behavior was observed at negative voltage as well and events recorded at −100 mV (red) overlap with events recorded at 100 mV (black). Event number was lower due to a shorter recording time and interestingly, no similarity was found in the event statistics. A possible reasons for this inconsistency could be the "wrong" orientation of the pore in the lipid membrane. The "right" orientation is considered when the pore cap is on the *cis* side of the

membrane (ground electrode). For the Orbit, nanopores are located in both *cis* and *trans* compartments, possibly due to the membrane breakage in time of the experiment.

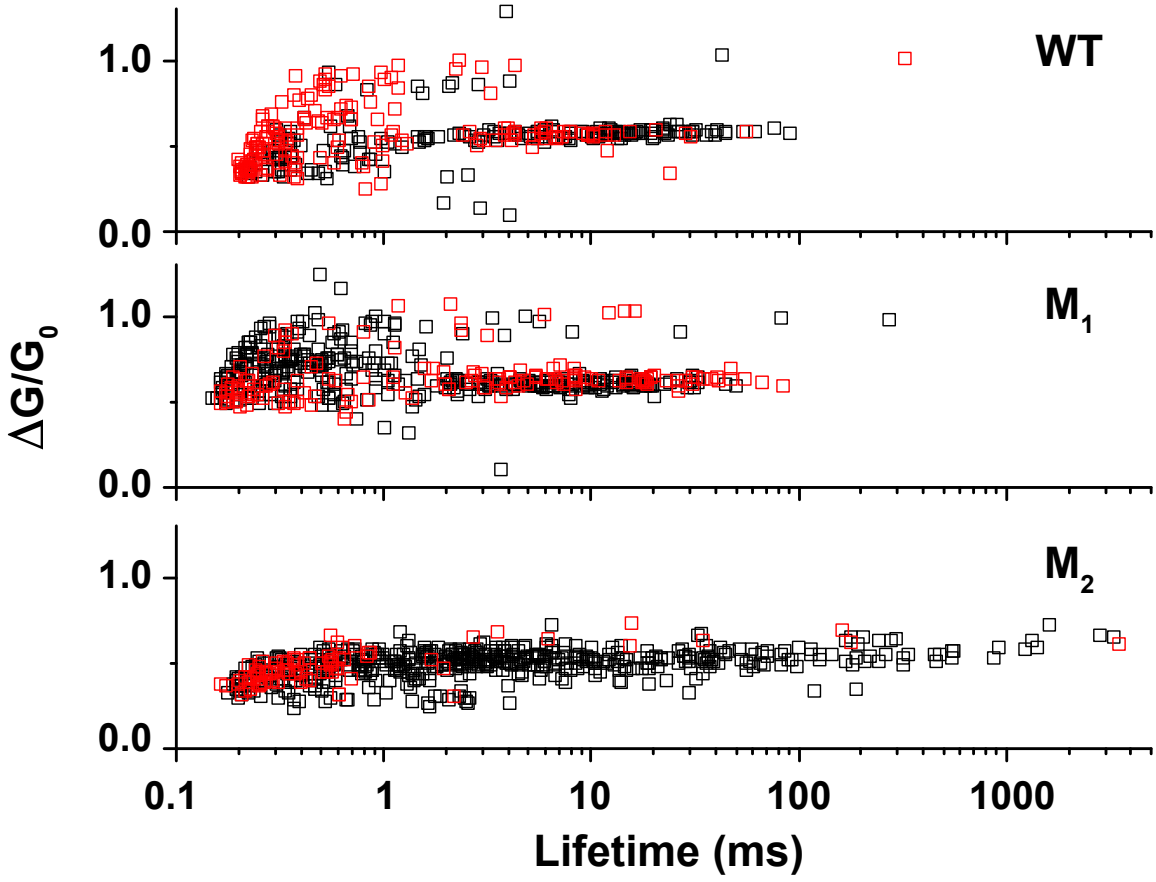

Figure 4.27: Scatter plots statistics of sub-conductances, recorded at 100 mV (black) and -100 mV(red)

In addition as for T pore, for some LB channels baseline sub-states events were detected. Structure dependent behavior were compared for (T pore, LB-WT, LB-M_1, LB-M_2) of baseline sub-states (I, II, III) and the sub-conductance states (IV) at 100 mV (see Figure 4.28, Table 4.3).

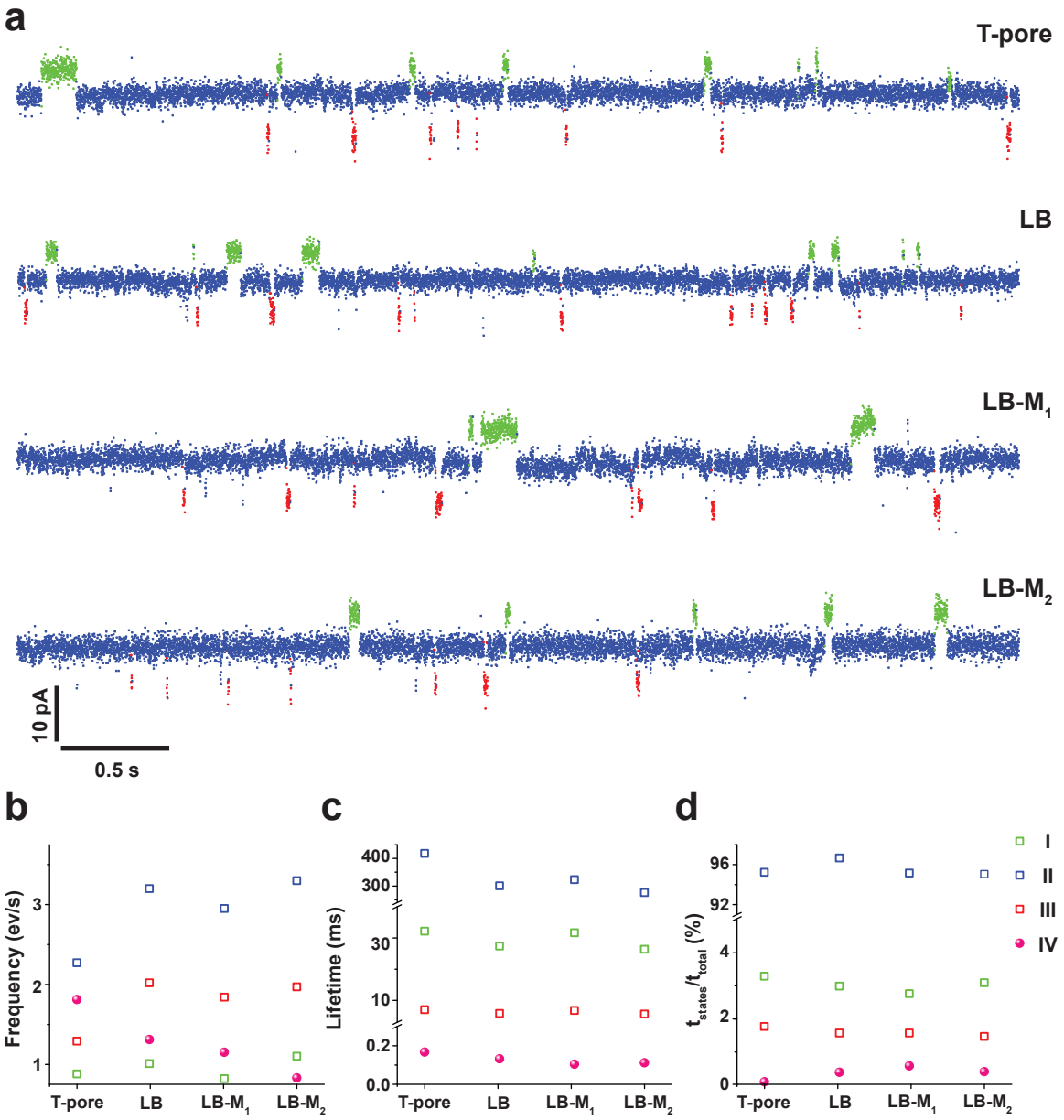

Figure 4.28: HMM analysis summary for T pore and LB-WT, LB-M_1 and LB-M_2 a) Baseline sub-states distribution for several synthetic channels, recorded at 100 mV. b) Frequency distributions, c) Lifetime distribution and d) Time rate percentage of type I (green), type II (blue) and type III (red) and events, for synthetic channels

Channel	Voltage	Frequency (ev/s)				τ (ms)				t_{states}/t_{total}(%)			
		I	II	III	IV	I	II	III	IV	I	II	III	IV
T pore	50 mV	0.85	2.3	1.4	1.2	31.7	408	6.3	0.119	3.0	95.7	1.2	0.0011
	75 mV	0.87	2.5	1.5	1.6	39.4	369	7.4	0.115	3.7	94.7	1.5	0.011
	100 mV	0.88	2.3	1.3	1.8	32.1	418	7.0	0.167	3.3	95.2	1.3	0.104
	125 mV	0.77	2.2	1.3	4.5	30.6	426	7.3	0.133	2.9	95.1	1.8	0.47
	150 mV	0.69	1.7	0.6	6.4	31.9	388	11.7	0.146	2.4	94.2	1.2	2.16
LB-WT	100 mV	1.01	3.2	2.0	1.3	27.4	301	5.8	0.132	3.0	96.7	1.57	0.39
LB-M_1	100 mV	0.82	2.9	1.8	1.15	31.6	323	6.75	0.1	2.8	95.2	1.57	0.58
LB-M_1^*	100 mV	1.22	3.5	1.9	0.95	22.7	261	16.1	0.1	3.0	92.2	4.17	0.57
LB-M_2	100 mV	1.10	3.3	2.0	0.8	26.3	276	5.6	0.111	3.1	95.1	1.47	0.41

Table 4.3: Baseline sub-states (I, II, III) and sub-conductance (IV) statistics summary for gating behavior

For experiments recorded on the Orbit synthetic DNA origami channels presented baseline sub-states. Recorded channels does not have a consistent baseline sub-states behavior. Our main hypothesis is that these events are correlated with the lipid membrane and its elasticity can differ from one preparation to another due to different solvent concentrations present in the lipid membrane. However, all channels exhibit similar trends in the event frequency, event lifetime and the presence of sub-states. We can conclude that the baseline sub-states are therefore independent of the channel geometry. We observed total channel closure for all synthetic channels on the Orbit with step size corresponding to a single channel conductance.

LB-WT exhibits sub-conductance states, but the statistic varies from one channel to another. Channels with no flickering were also recorded, therefore the hypothesis that the current flickering are caused by extrachannel scaffold loops is excluded. While experiments performed at negative voltage could not prove or disprove this assumption. Second hypothesis for the cause of of sub-conductance states is that DNA staples can unzip from the structure under the influence of the electric field in the channel. In regard to this two different mutants were tested, M_1 containing a bait pointing into the central channel and M_2 pointing in one of the neighboring cup channels. All mutant channels showed sub-conductance (see Figure 4.26). The events statistics are very similar for all M_1 mutant channels (see Figure 4.26 i-v). In contrast M_2 event statistics are different for each channel (see Figure 4.26 vi-x). This suggests that the position at which the DNA staples are broken is electric field sensitive, and therefore the other staples can unzip. Additionally, as seen in figure 4.26 viii the event statistic can be very similar for M_1 and M_2, suggesting that the bait can cross into the main channel, or that a staple in the same region broke, or did not hybridize properly, causing similar fluctuations.

4.2.5 Translocation experiments

Similar to biological pores synthetic DNA channels can be used as sensing devices to discriminate analyte molecules by studying their translocation characteristics. Here, we used LB and T pores for single-molecule studies of hairpin unzipping, guanine quadruplex [26] unfolding and dsDNA translocation. Single-stranded DNA is expected to fit through the 2 nm wide central pore of the LB, while the increased size of the T pore permitted the passage of biomolecules with larger diameter.

Translocation experiments on LB was performed using Orbit that was attached to the Tecella amplifier. The translocation time of ssDNA through αHL at room temperature is $\approx$100 µs [113] which is below the Tecella detection limit. For this reason we choose DNA molecules (hairpin and quadruplex structures) with polythymidine tails. The DNA catching will be facilitated due to the ssDNA tail but in order to pass the pore the structures need to unzip or unfold as known from experiments done using α-HL [153, 135, 107]. This time delay in the current blockades allows to create signals detectable by the Tecella amplifier. Experiments were performed for both forward (*cis* $\rightarrow$ *trans*) and backward (*trans* $\rightarrow$ *cis*) directions (see Figure 4.29). For one set of experiments, we used a DNA hairpin with a 9 base-pair long stem flanked by 50 thymidines on the 3′ end and 6 thymidines on the 5′ end (see Figure 4.29 a).

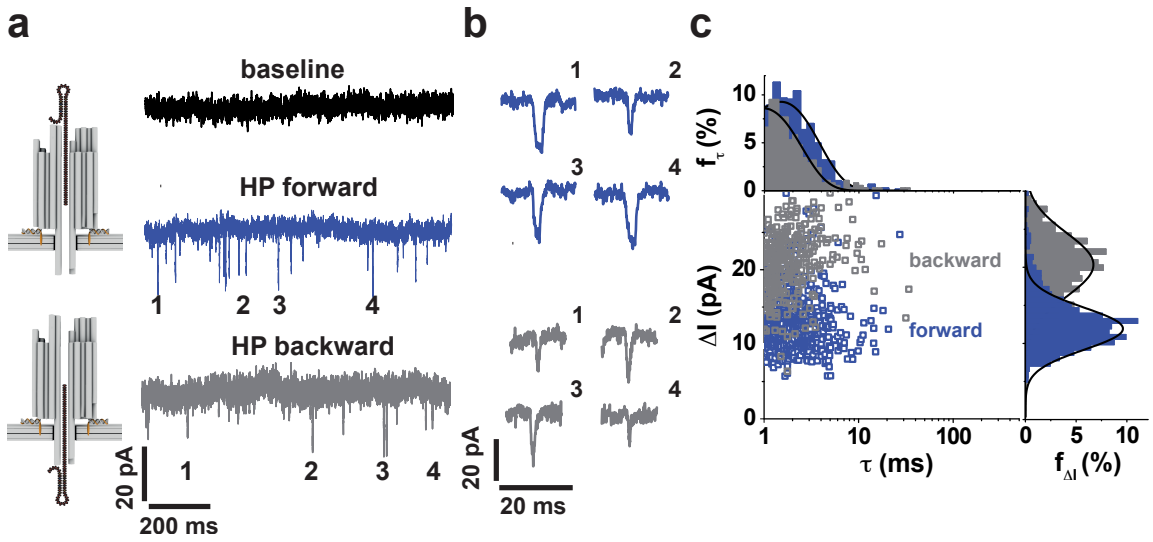

Figure 4.29: DNA-HP translocation studies LB. a) Addition of DNA hairpins (T_6-HP-T_{50}) to a DNA channel at V=200 mV results in the appearance of current blockades, indicating unzipping and translocation of hairpin molecules from *cis* $\rightarrow$ *trans*. Hairpins accumulated on the *trans* side can also be transferred back from *trans* $\rightarrow$ *cis* by a reversal of the transmembrane voltage. b) Representative blockade events for forward (top) and backward (bottom) translocation of DNA hairpins. c) Scatter plot for the translocation of T_6-HP-T_{50} DNA through a DNA channel from *cis* $\rightarrow$ *trans* (blue) and from *trans* $\rightarrow$ *cis* side (gray) at V=200 mV, and corresponding histograms. Each data point corresponds to a single translocation event. In total, 777 (forward) and 379 (backward) events were analyzed.

The hairpin molecules were initially added to the *cis* side of a lipid membrane containing a single synthetic DNA channel that displayed a stable current baseline without gating. Application of a positive voltage bias (200 mV) leads to capture, unzipping, and translocation of the hairpin structures resulting in transient current blockades (see Figure 4.29 a, b). Reversal of the bias (-200 mV) after approximately ≈30 min again led to transient current blockades, this time caused by molecules that had accumulated in the *trans* compartment by previous translocation through the DNA channel. The blockade amplitudes for both translocation directions were $\Delta I_{cis-trans}$=11.9±2.7 pA and $\Delta I_{trans-cis}$=20.3±4.2 pA. The blockade dwell-times were distributed exponentially with a characteristic lifetime of $\tau_{cis-trans}$=1.5 ms and $\tau_{trans-cis}$=1 ms, respectively (see Figure 4.29 c). In order to demonstrate that the observed translocation signals are not subconductnce-gating, their voltage dependence was studied (see Figure 4.30).

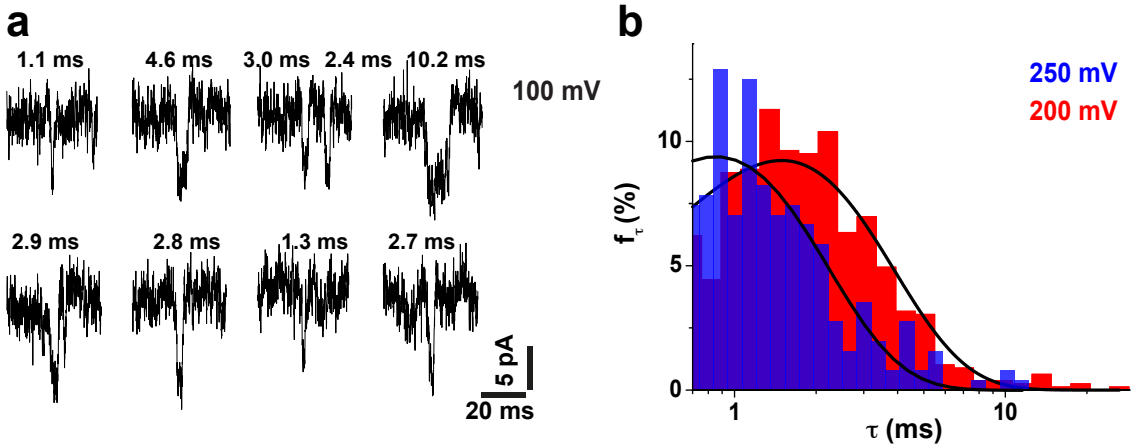

Figure 4.30: LB, hairpin translocation voltage dependence a) Examples for hairpin translocations at 100 mV with dwell-times in the range 1-10 ms. b) Comparison of hairpin translocations at 200 mV and 250 mV. The black lines correspond to exponential fits with τ = 1.5 ms and τ = 0.9 ms.

As shown in Figure 4.30 a, hairpin translocation can be measured at V=100 mV with typical dwell-times in the range 1 ms to 10 ms. At this voltage, the event rate as well as their amplitude is very low and we were therefore not able to collect enough data for performing a statistical analysis. Translocation studies were also performed at V=250 mV (see Figure 4.30 b). The dwell-times decrease from 100 mV over 200 mV to 250 mV, which is a clear sign of voltage-assisted unfolding/translocation of the hairpin structures. In contrast, sub-conductance states observed for some LB channels are voltage independent as described in Sec. 4.2.4. Measurements at V=250 mV are already performed close to the breakdown voltage of the lipid bilayer membrane, and thus also demonstrate that the stability of the DNA channels in an electrical field is not a limiting factor.

In another set of experiments, we added quadruplex-forming oligonucleotides with a 60 thymidine long single-stranded tail (Q-T_{60}) to the *cis* side of a membrane containing a single synthetic DNA channel (see Figure 4.31 a, b). Again, we observed transient current blockades, which correspond to the capture and threading of quadruplex DNA molecules into the channel, followed by unfolding and subsequent translocation through the pore. Removal of the analyte from the *cis* compartment restored a stable baseline current without blockades. Subsequent addition of quadruplex DNA with a longer $(dT)_{125}$ tail (Q-T_{125}) led

to larger current blockades. The average current blockades were ΔI_{Q-T60}=5.6±1 pA and ΔI_{Q-T125}=15.3±2.3 pA respectively. The fact that longer tails lead to a larger transient current reduction is another clear indication of translocation through the central channel of our DNA structures. Moreover, the current blockade amplitudes measured in these experiments can be used for a qualitative discussion of the electric field distribution within the DNA channel. The blockade dwell-times are distributed exponentially with characteristic lifetimes of $\tau_{Q-T_{60}}$ = 9.7 ms and $\tau_{Q-T_{125}}$ = 8.1 ms.

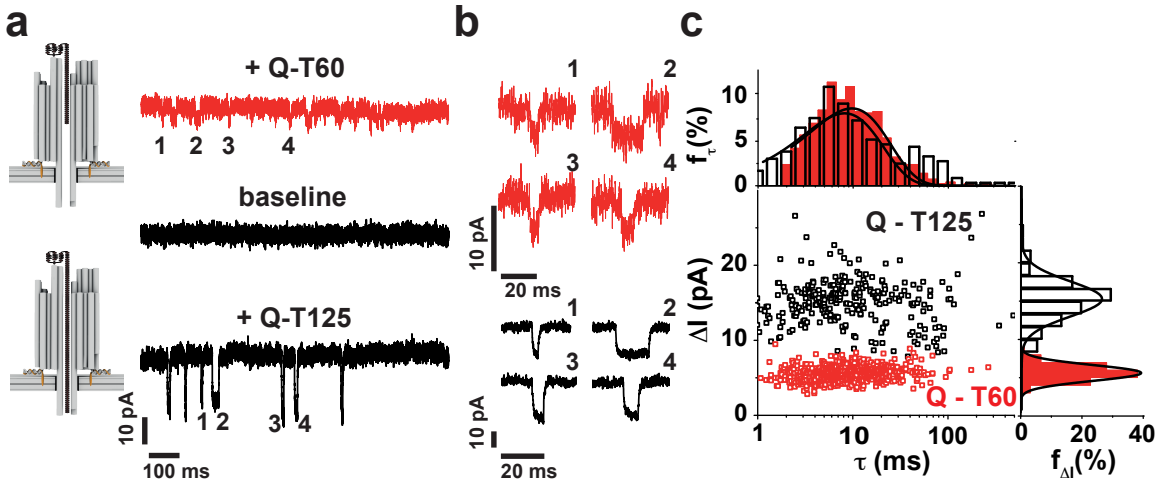

Figure 4.31: DNA-Q translocation studies LB, forward. a) Top: Typical current trace at V=200 mV after addition of 10 µM of Q-*T*60 DNA. Middle: Current trace after rinsing with buffer solution. Bottom: Current trace after subsequent addition of 10 µM of Q-T_{125} DNA to the same channel. b) Representative blockade events for Q-T_{60} (top) and Q-T_{125} DNA (bottom). c) Scatter plot of the current blockade versus dwell-time for the translocation of Q-T_{60} (red) and Q-T_{125} DNA (black) through the DNA channel. In total 631 (Q-T_{60}) and 279 (Q-T_{125}) events were analyzed. On the right and on the top corresponding histograms are shown. The lines correspond to single exponential (top) and Gaussian fits (right).

In Figure 4.32 a, a scatter plot generated from backward translocation events (*trans* → *cis*) of Q-T_{125} DNA at negative bias potential is shown. The scatter plot histograms yield a blockade amplitude that is 27% lower (11.2 pA) and a characteristic dwell-time that is 2.3 times shorter (3.5 ms) than for the forward direction. This observation indicates a directionality of the translocation process itself, as the integrated electrophoretic force along the DNA channel should be independent of the direction of translocation (as the T_{125} tail is expected to traverse the whole central channel). A possible reason for this effect may be steric or binding interactions at the entrance of the asymmetrically designed origami structure.

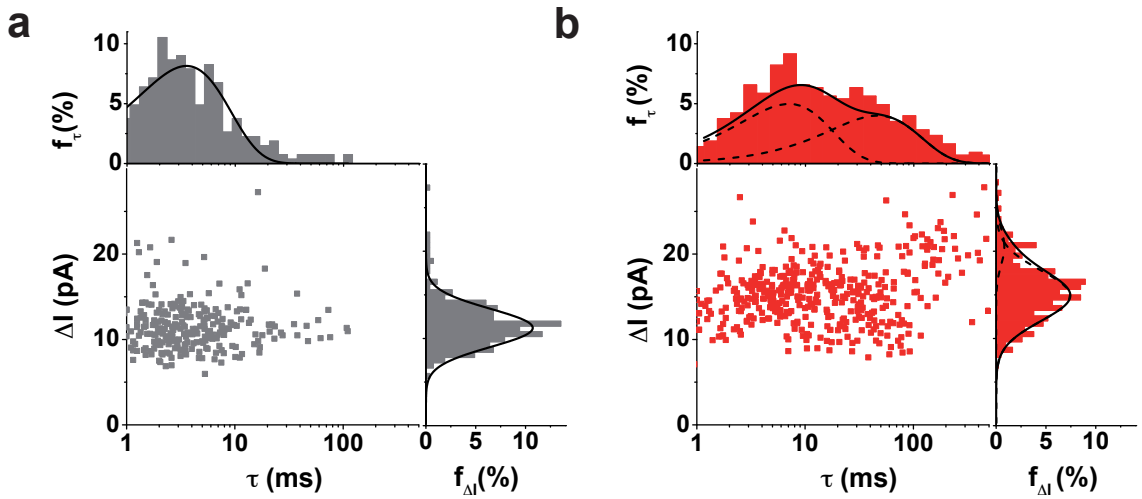

Figure 4.32: DNA-Q translocation studies LB. a) Scatter plot of the current amplitude vs. dwell-time for the backward translocation of Q-T_{125} through the artificial ion channel at negative bias voltage (-200 mV), accompanied by the corresponding histograms. 266 events were detected. The solid lines correspond to single exponential (top) and Gaussian (right) fits to the histograms. b) Scatter plot of the current amplitude vs. dwell-time for forward translocation of Q-T_{125} (see Figure 4.31), including data from the last part of the measurement. Each data point corresponds to a single translocation event. The lines correspond to single exponential (top) and Gaussian (right) fits to the histograms.

For prolonged measurement times for the Q-T_{125} translocation experiment in forward direction (see Figure 4.31 c), a sudden increase in long-lived blockade events was observed. A scatter plot including all Q-T_{125} measurement data recorded for these events is shown in figure 4.32 b. In this plot, a second population is clearly visible. It features a higher blockade amplitude (20.5 pA) than the main population and a considerably longer characteristic dwell-time (46 ms). A comparable population was not observed for the Q-T_{60} measurement or for the Q-T_{125} backward translocation measurement. One possible explanation for this time dependent effect is the agglomeration of DNA molecules at the channel entrance over the course of a measurement run. In fact, after addition of quadruplex DNA the event rate continuously increased, indicating that the DNA concentration at the pore entrance rises over time. This may be a result of insufficient mixing upon addition (we mixed very gently to avoid destruction of the membrane) or interaction of DNA with single-stranded scaffold loops protruding from the DNA channel structure.

As discussed above, in contrast to the LB pores the T pore can allow translocation of long double-stranded DNA molecules. The experiments were performed on the DIB, and the signal was recorded using a Heka amplifier. As expected, blockade events appeared after addition of dsDNA (see Figure 4.33 a). In figure 4.33 b, a scatter plot of the current reduction ΔI vs. the translocation time τ is shown for all events detected at 75, 100 and 125 mV before and after dsDNA ($\approx$ 500 base-pair (bp)) addition. ΔI increases with voltage, while the event duration decreases. The frequency of translocation events and the speed of the molecules increases with transmembrane voltage (see Figure 4.33 c). The dwell-time in the channel decreases from 162 µs (75 mV) over 146 µs (100 mV) to 143 µs (125 mV) (see Figure 4.33 d).

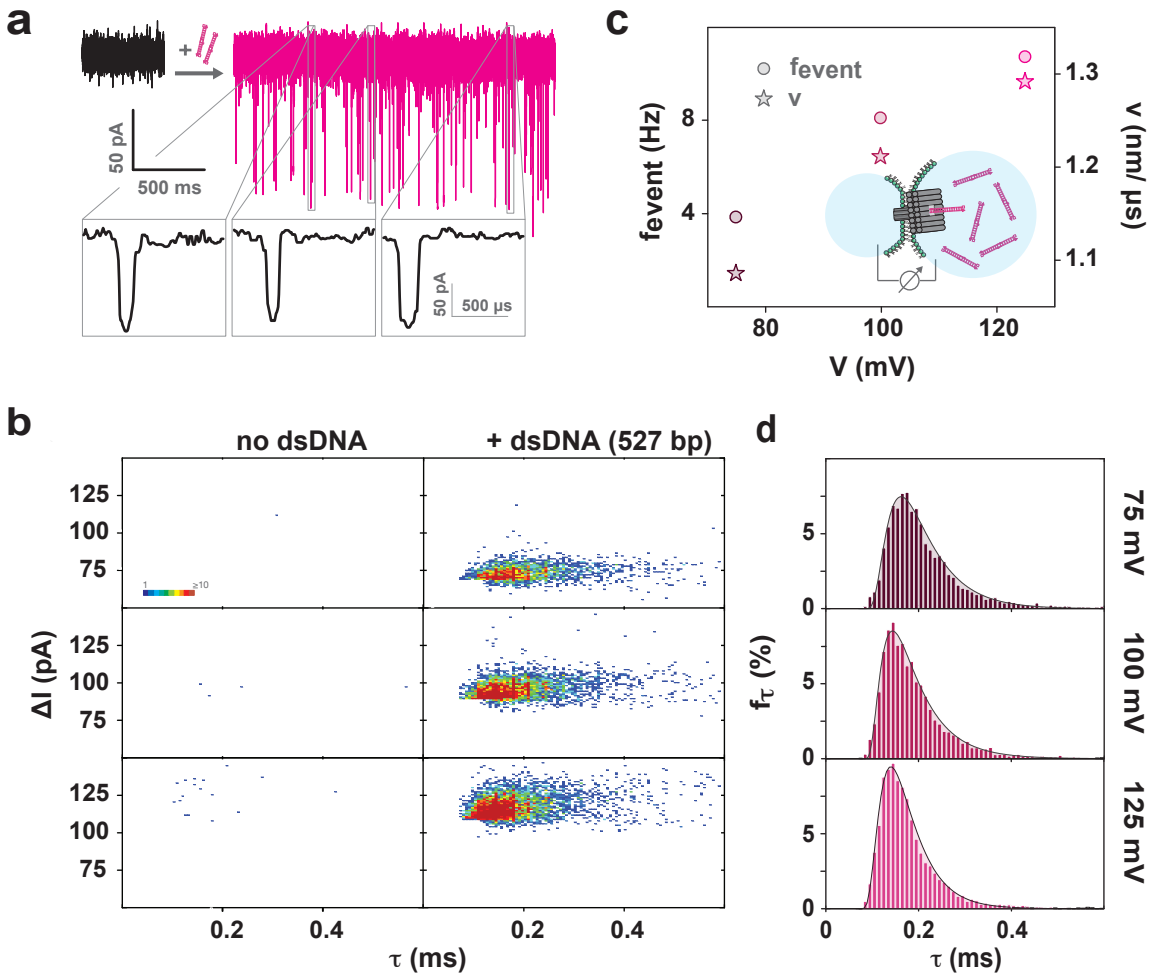

Figure 4.33: Translocation of 527 (bp) dsDNA through T pore. a) Sample trace of a current measurement through a single DNA channel incorporated into a lipid bilayer membrane in the absence of analyte molecules, performed at a transmembrane voltage of 125 mV (black). Current trace recorded in the presence of 527 bp long dsDNA (pink). Three examples for translocation events are shown in detail below the trace. b) Scatter plot of the current reduction ΔI vs. the translocation time τ is shown for all events detected at 75, 100 and 125 mV. c) Translocation velocities and event frequencies extracted from the measurements. Inset: All electrical recordings were performed with the droplet interface bilayer technique. d) Distribution of event durations extracted from current traces recorded at 75, 100 and 125 mV. The histograms were fit with a one-dimensional drift-diffusion model for nanopore translocation 7 with the two fit parameters v and D (velocity and diffusion coefficient).

Another set of translocation experiments was performed with both ssDNA and dsDNA analytes, using a T pore modified with a 6 nt long single-stranded DNA obstacle (sequence 5′ - TTGGCC - 3′) in the middle of the central channel. A single-stranded obstruction inside of the channel slows down the speed of the translocations. We also find that translocation of single-stranded DNA results in less pronounced current reductions than for dsDNA analytes, consistent with the smaller diameter of ssDNA (see Figure 4.33).

In the experiments, first ssDNA (140 bases) and then dsDNA (115bp) molecules were added to one of the aqueous droplets of the DIB (2M KCl, 5mM $MgCl_2$) in a stepwise fashion. While in the presence of only ssDNA translocation events were indeed recorded (see Figure 4.34 a), their depth and length overlapped with events occurring in the background signal. However, the event frequency increased significantly compared to background. As expected for real translocation events, event frequency and translocation velocity increased (see Figure 4.34 b), while translocation time decreased with increasing voltage (see Figure 4.34 c). The diffusion coefficients (2.4 $nm^2/\mu s$ (50 mV), 2.4 $nm^2/\mu s$ (75 mV) and 2.8 $nm^2/\mu s$ (100 mV)) were approximately independent of the applied voltage. Clear translocation events were observed for the ssDNA-dsDNA mixture, i.e., after addition of dsDNA (see Figure 4.34 d). The event frequency increased drastically compared to the previously recorded ssDNA (see Figure 4.34 e). The translocation times decreased with increasing voltage (from 184 µs (50 mV) over 170 µs (75 mV) to 150 µs (100 mV)), whereas the velocity increased with voltage (0.26 nm/µs (50 mV), 0.32 nm/µs (75 mV) and 0.42 nm/µs (100 mV)). These results confirm that the observed events are caused by the passage of DNA through the pore. In order to obtain information about translocation time and velocity of the translocating dsDNA molecules only, the events were split into two populations for further analysis. We attributed the top (large ΔI) population in the scatter plots predominantly to the presence of dsDNA (see Figure 4.34 f, top), while the bottom population (shown in faded colours in Figure 4.34 f) was not taken into account. The resulting translocation times obtained from the restricted population are displayed in figure 4.34 f (velocities in Figure 4.34 e). The diffusion coefficients 2.7 $nm^2/\mu s$ (50 mV), 2.5 $nm^2/\mu s$ (75 mV) and 2.3 $nm^2/\mu s$ (100 mV) obtained by the 1D drift-diffusion regression analysis are approximately independent of voltage. The velocitiy of dsDNA is thus approximately half of the values obtained for ssDNA in this particular set-up. This finding seems consistent with the smaller persistence length, diameter and charge density of ssDNA, which might result in less friction and electrostatic interactions inside of the DNA channel. Notably, the translocation of 115 bp dsDNA in the presence of an obstacle inside of the channel is much slower (by a factor of $\approx$5) than of the longer 527 bp dsDNA without obstacle (see. Figure 4.33 d and Figure 4.34 f), indicating that the ssDNA obstacle has a drastic effect on translocation dynamics.

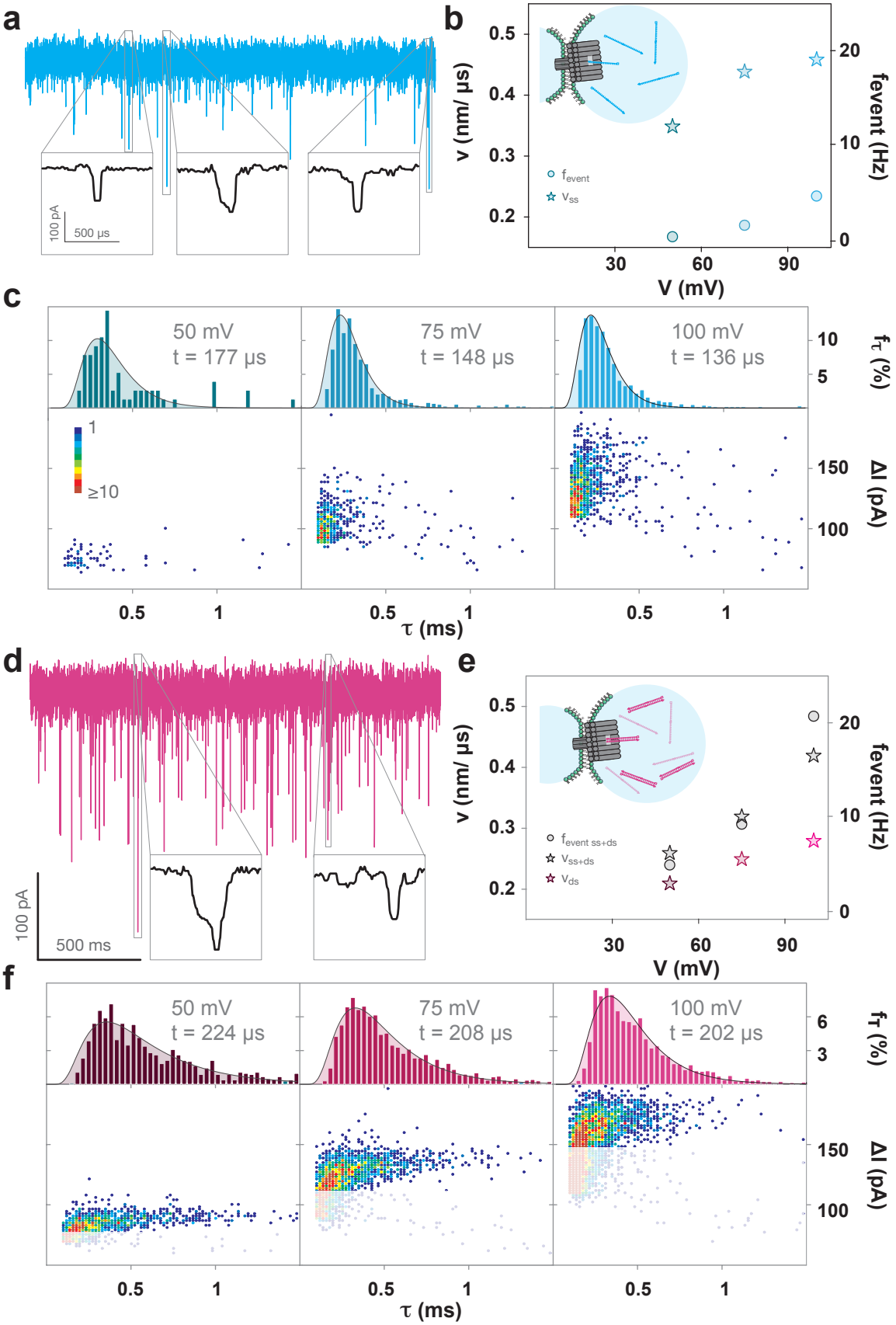

Figure 4.34: Translocation experiments ssDNA and dsDNA. a) Sample trace with ssDNA at 100 mV. b) Event frequency (f) and translocation velocities (ν) for ssDNA c) Distribution of event length (τ) and f. d) Sample trace with ssDNA and dsDNA at 100 mV, e) f and ν for a mixture of ssDNA and dsDNA and f and ν for dsDNA only. f) Distribution of τ and f for dsDNA.

4.2.6 Mapping the potential inside the LB pore

The larger current blockade for Q-T_{125} as compared to Q-T_{60} translocations can be explained by the larger volume occupied in the channel by the longer T_{125} tail as compared to the T_{60} tail. In a simple picture, the presence of a DNA strand of length L_{DNA} reduces the effective area of the channel from A to A-A_{DNA}, where A_{DNA} is the area of single-stranded DNA. Hence, the total conductance of the channel is given by the series of the conductances of blocked (G_b) and unblocked (G_u) part, i.e.,

$$\begin{aligned} G_b &= \sigma(A - A_{DNA})/L_{DNA} \\ G_u &= \sigma A/L - L_{DNA} \\ G_{tot} &= (G_b G_u)/(G_b + G_u) = \\ &= \sigma(A(A - A_{DNA}))/((A - A_{DNA})L + A_{DNA}L_{DNA}) \end{aligned} \tag{4.2}$$

Compared with an unoccupied channel the relative current reduction (conductance reduction) is then given by:

$$\begin{aligned} \Delta I/I = \Delta G/G = 1 - (A - A_{DNA})L/((A - A_{DNA})L + A_{DNA}L_{DNA}) = \\ = (A_{DNA}L_{DNA})/((A - A_{DNA})L + A_{DNA}L_{DNA}) \end{aligned} \tag{4.3}$$

A 125 thymidine tail fully stretched to its contour length has a length of L_{DNA} ≈50 nm, i.e., it spans the whole length of the DNA channel. Assuming an effective diameter of 1 nm for ssDNA, we would expect a current/conductance reduction of ΔG/G of A_{DNA}/(A-A_{DNA}) ≈ 33% (L=L_{DNA} in the formula above), which is considerably higher than what we observe (around 10%). This may be attributed in part to the lateral leak conductance of the channel structure. A 60 nt long tail corresponds to a length of L_{DNA} ≈24 nm (assuming a base-to-base distance of 0.4 nm), from which we expect a ΔG/G of ≈ 33%. While again our experimentally observed reduction is smaller (≈ 5%), this value is completely consistent with the value for the 125 tail if one takes the leak conductance into account. A qualitative study of how the LB-origami structure's intrinsic electrical conductivity impacts potential distribution and channel conductance was performed by means of a finite element simulation using Comsol Multiphysics. The channel interior and adjacent solution compartments were simulated with KCl solution bulk conductivity (11 S/m). To screen the influence of origami leakiness, the conductivity of the origami structure was varied in the simulation from 10^{-4} S/m (insulating) to 10 S/m.

The electrical potential along the channel's central axis is shown in Figure 4.35 c. Even at comparably low origami conductivity, a considerable inhomogeneity of the potential drop is apparent. Notably, the region of the steepest slope is not at the center of the channel structure, but at the bilayer, i.e. 26 nm from the *cis* side channel entrance. The local variation of electric field strength for non-zero leak conductivity can be expected to strongly influence translocation experiments, where charged molecules are pulled electrophoretically through the pore (see Section 4.2.5).

As discussed in the previous Sec. 4.2.2, a partially conductive DNA channel structure would result in a more complicated potential landscape and electric field distribution than the simple pore picture used for the estimations above. In Figure 4.35 d, the lengths of the DNA molecules are depicted together with several values of leak concuctivity. For a finite leak conductivity, we expect a much stronger influence on the conductance from DNA molecules with long tails - traversing the high field region defined by the lipid bilayer membrane - than for the short tails. In fact, it is expected that short - tailed DNA molecules may feel a considerably smaller electric force depending on the exact field distribution. Furthermore, we expect short-tailed molecules to be sensitive to the translocation direction. As seen in

the scatter plot (see Figure 4.29) for DNA hairpins with a 50 nt tail, backward translocation results in faster translocations with a higher current amplitude, indicating that the short tail penetrates deeper into the high field region for the backward direction.

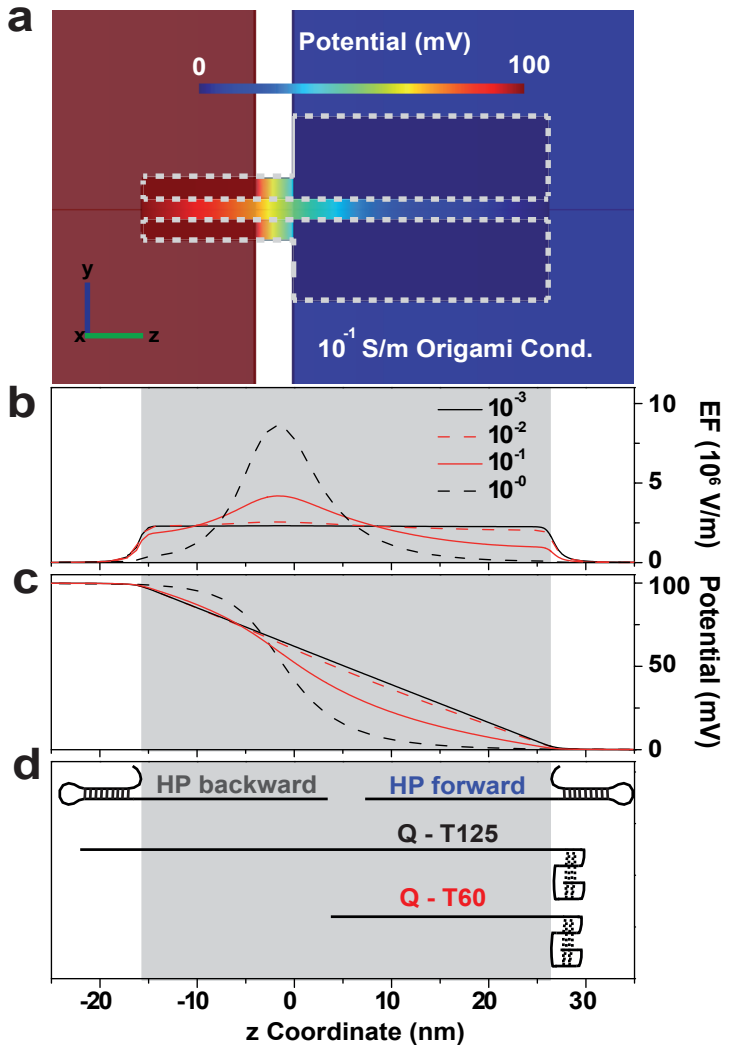

Figure 4.35: FEM Simulations of the LB pore. a) Color map of the electrical potential distribution along a y-z plane at x=0 calculated for 0.1 S/m origami conductivity. The dashed line marks the structure boundaries. b) Electric field along the symmetry axis (z-axis) of the channel for varying origami conductivity. c) Corresponding potential drops along the channel. d) Schematic illustration of the penetration depth of the structures used in translocation experiments before unzipping (see Figure 4.29 and 4.31).

For translocation experiments we expect the DNA tails to be fully stretched in the channel, and therefore their lengths are simply given by the number of bases mulitplied with the base-to-base-distance for ssDNA (0.4 nm-0.5 nm). As the channel width (2 nm) is close to this length as well as to the persistence length of ssDNA, the usual theories for polymer conformation inside a narrow channel are not applicable - these refer either to the limiting case where the channel diameter is much larger than the persistence length (resulting in a

scaling treatment) or much smaller than the persistence length (resulting in a mechanical deflection model) [154]. A better molecular understanding of the conformation of DNA strands inside a DNA channel will require molecular modeling and simulation [3]. For 100 mV applied bias over a length of L=42 nm, we expect electrostatic forces to be well in the higher pN regime, which is supported by the fact that we observe force-induced melting of DNA duplexes in the translocation experiments. In free solution experiments, a single-stranded random coil structure would be completely stretched out at these forces, and we assume the same to be the case in the context of our translocation studies.

Electric field was mapped for the T pore, similar with the LB pore higher electric field is simulated at the lipid membrane region.

4.3 Conclusions

In conclusion, the shape and size of DNA-based nanochannels can be widely adjusted using the tools of DNA nanotechnology. They can be easily modified with multiple chemical functionalities, at exact stoichiometries and with nanometer precision, which allows tuning of the channels to meet the requirements of specific applications. Force spectroscopy using synthetic nanopores for hairpin unzipping and G-quadruplex unfolding was demonstrated. Electrically driven translocation of double-stranded DNA through a large T pore was proved. For future investigations it will be interesting to actively unfold proteins, which are too large to pass through a DNA channel without the application of electrical forces. An alternative will be to perform force spectroscopy experiments similar to those accomplished with aptamer-ligand complexes, however then replacing αHL with DNA channels. Nanopore force spectroscopy on αHL has been shown to be an attractive tool for the investigation of interactions of DNA molecules with smaller ligands. Single molecule nanopore experiments allow the determination of the distribution of bound and unbound complexes, dissociation constants, and of voltage-dependent unfolding rates. Single molecule protein biosensors can be created by modifying a DNA channel with protein binding partners. First experiments were performed by adding an aptamer on a neighboring stem helix on the top of one of the DNA pores, the wheel pore. Small differences in the lifetime were observed after the addition of the binding partner. In order to achieve a larger effect the aptamer apparently has to be placed at the entrance or inside of the channel, here we will have to find a balance between large current modulation and potential blockage of the channel.

In addition to single molecule sensing, the synthetic DNA channels introduced here open up broad perspectives for applications as antimicrobial agents and interference with cellular homeostasis. In this context we have shown that DNA membrane channels can spontaneously insert into lipid bilayer membranes also in the absence of transmembrane potentials. The incorporation efficiency increased with an increased number of hydrophobic modifications. Generally, we believe that fully synthetic lipid membrane channels are a crucial first step towards harnessing ion flux for driving sophisticated nanodevices that are inspired by the rich functional diversity of natural membrane machines such as ion pumps, rotary motors, and transport proteins.

5 Appendix

5.1 Wheel pore as a molecular biosensor

We investigated the influence of an aptamer modification (an anti-thrombin aptamer) close to the channel entrance on a neighboring stem helix of the wheel pore (see Figure 5.1). We expected that the analyte thrombin would transiently bind to the aptamer and thus modulate the current measured through the channel.

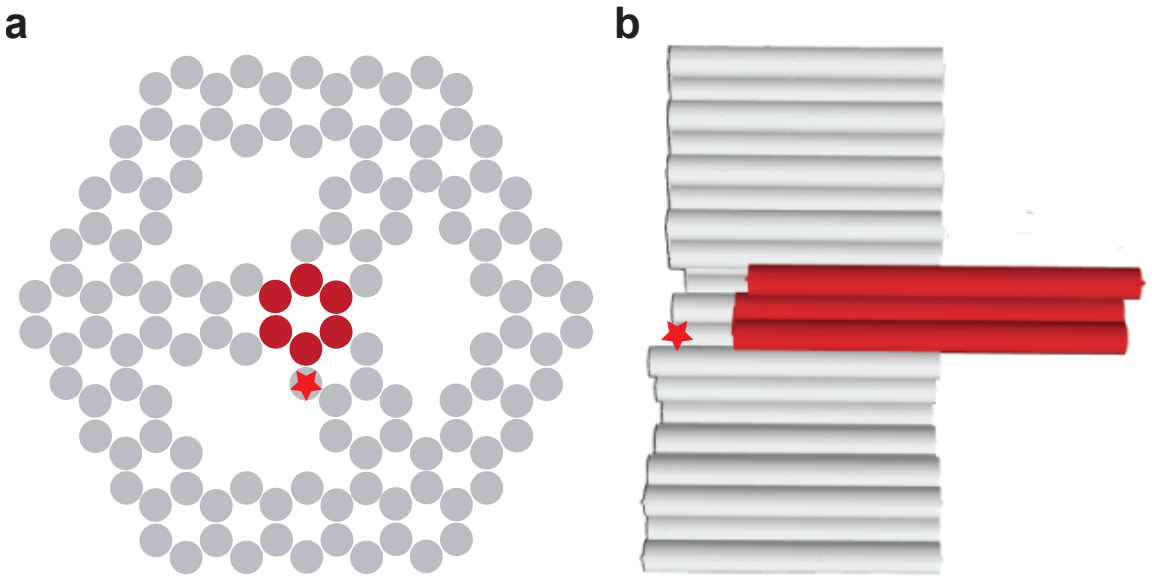

Figure 5.1: Schematic representation of a modified wheel pore. The step penetrating the lipid membrane is depicted in red, and the modification is a green star. a) Top view, b) Bottom view.

As for gating analysis of LB and T pores, HMM was performed on modified wheel pore. As observed from the example trace, the modified wheel pore has different event statistics than the LB and T pores (see Figure 5.2).

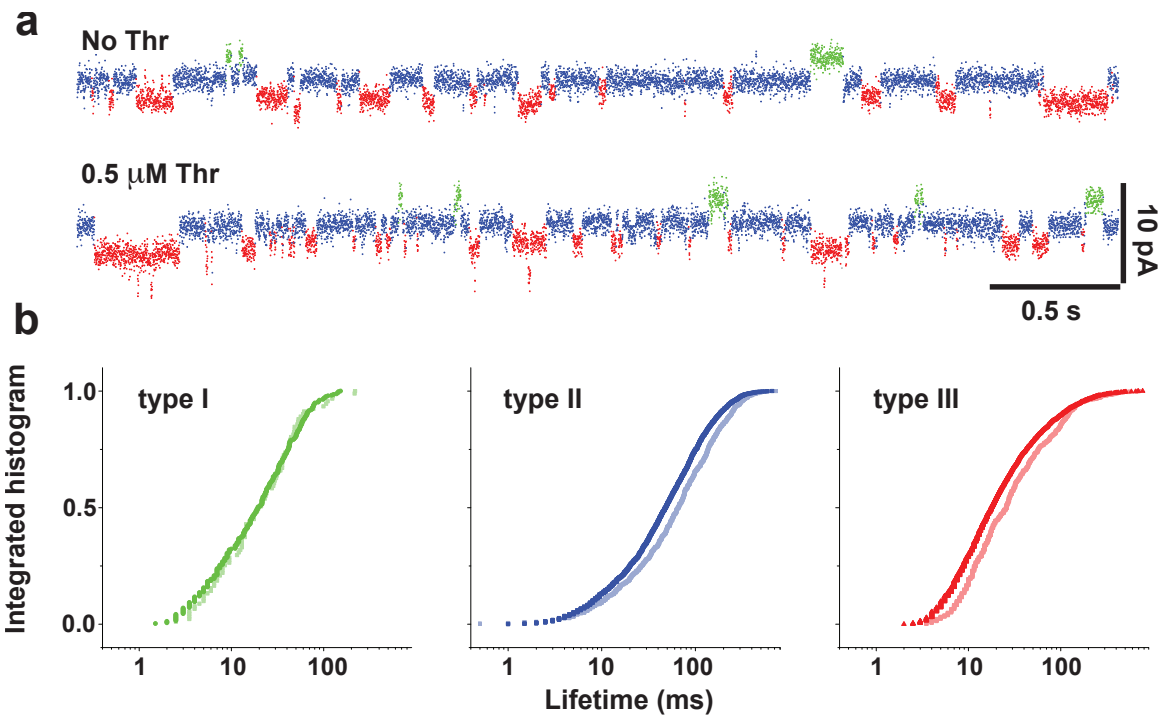

Figure 5.2: Wheel pore molecular biosensor, baseline sub-states. a) HMM analysed baseline sub-states for experiments performed in presence or absence of thrombin. b) analysis of the modified wheel pore. Experiment was performed at 50 mV.

Results are summarized in Table 4.3, event type I (green) has similar behavior as for previous analyzed channels, it occupies approx. 2.5% of the whole time and shows a lifetime of ≈26 ms. We hence conclude that the type I states are independent of a range of pore parameters: of the length of the stem, of the cross-sectional area of the channel and of the presence of an aptamer at the top or a bait inside the pore. The type III state increases its presence from ≈2 % of the total time for all the other pores to ≈30.6% for the modified wheel pore. The pore hence rests for a comparatively high percentage of time in type III state. It additionally implicates a shortening of the lifetime of type II events. The T pore, LB pores and LB mutants are ≈95% of the total time in type II state, whereas the modified wheel pore resides in baseline states (type II) for ≈66% of the time. The increased occurrence of the type III state reduces the lifetime of the type II state from ≈300 ms for the other pores to ≈95 ms for the G-quadruplex-modified wheel pore. In addition the occurring frequency of sub-conductance states (IV) is decreased.

Channel	Frequency (ev/s)				τ (ms)				$t_{states}/t_{total}(\%)$			
	I	II	III	IV	I	II	III	IV	I	II	III	IV
Wheel-Apt	0.8	6.7	5.9	0.45	25.8	95.4	33.6		2.5	66.3	30.6	0.54
Wheel-Apt+Thr	0.8	8.6	7.6	0.47	26.6	70	25.4		2.3	65.1	32.1	0.40

Table 5.1: Baseline sub-states (I, II, III) and sub-conductance (IV) statistics summary for the modified wheel pore.

We conclude that the G-quadruplex, residing 21 nm away from the bilayer, is capable of influencing the type III baseline sub-state. The LB pores with it's dangling loops on top, in a distance of 25 nm offers a very similar arrangement, however these loops cause less type III baseline sub-state. The scaffold loops located on the top of LB are in general single stranded when a Q-quadruplex has 2.5 nm diameter, and unfolding voltage of a quadruplex in 1 M KCl is higher than 200 mV (see force spectroscopy measurements on thrombin aptamer Section 3.1.3). The addition of thrombin changes the length of the lifetimes from 95.4 to 70.0 ms for type II, from 25.8 to 26.6 ms for the type I, from 33.6 to 25.4 ms for the type III states. The percentage of time spent in each state does not change much (66.3% vs 65.1%, 2.5% vs 2.3%, 30.6% vs 32.1%). The total distribution of states remains the same for type I events in contrast type II and type III events are more frequent and faster. The presence of the thrombin causes a slight shift of the overall time percentage from the type II states towards the type III states. A hypotheses is that the the aptamer-thrombin complex interacts not as strong with the channel as free G-quadruplex.

Interesting that the sub-conductances scatter plots presents two populations as described previous for the LB-M_1 (see Figure 4.26 i-v) and in some cases LB-M_2 (see Figure 4.26 i-v)

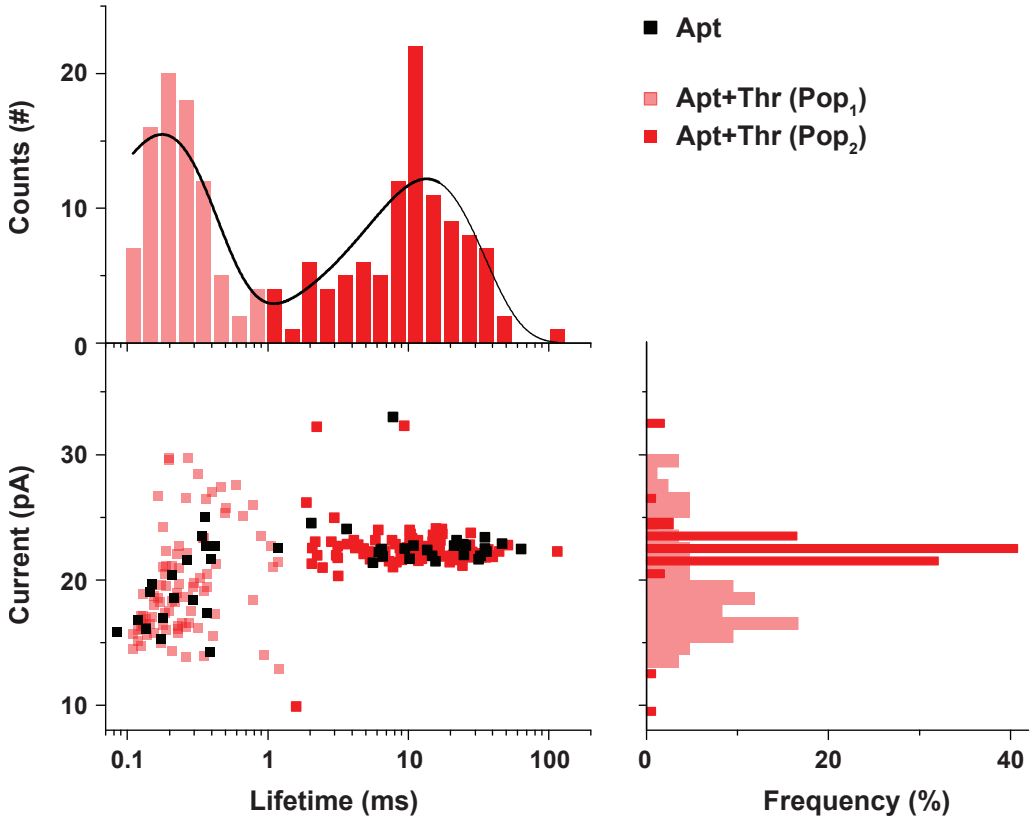

Figure 5.3: Wheel pore molecular biosensor, sub-conductance states analysis. Scatter plot for the sub-conductance states for aptamer modified wheel pore in the absence of thrombin (black) in the presence of thrombin (red) and at V=50 mV, and corresponding histograms. Each data point corresponds to a single sub-conductance event.

Small changes in lifetime of sub-conductance levels measured for the channel in the presence of thrombin, demonstrates that this sensing scheme could work in principle. Trials were

made by placing the aptamer at the entrance of the channel. In this case the channel was most of the time in the close state. Here, we have to find a balance between large current modulation and potential blockage of the channel. One alternative is to use low potassium concentration, in order to destabilize the aptamer structure.

5.2 Nanospot

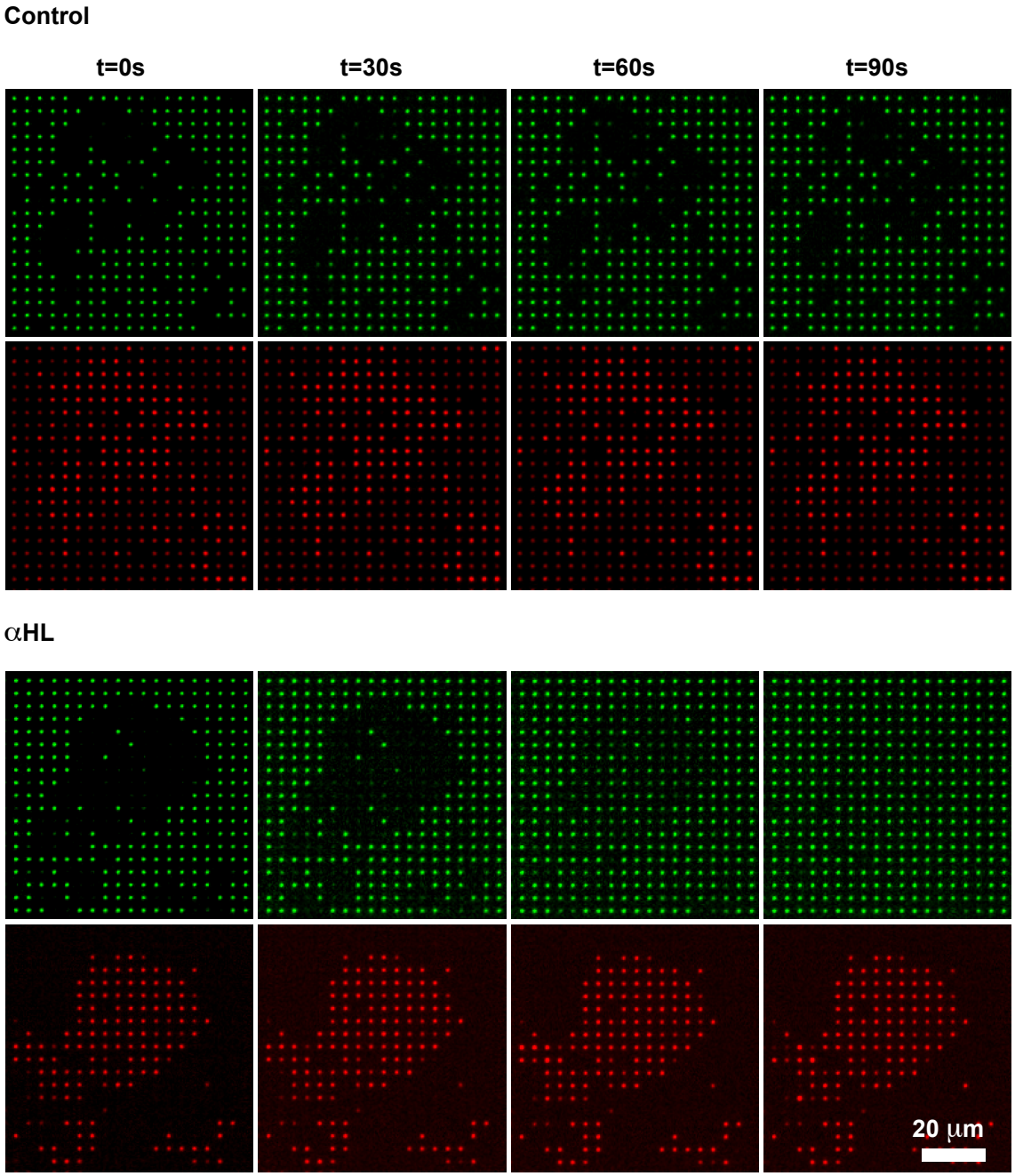

Figure 5.4: Dye influx through αHL on nanospot chip. Atto-488 (green) influx and membrane stability control experiments performed with Atto-595 (red) attached to a 10kDa Dextran molecule impermeable through a nanopore

Bibliography

[1] D. Afanasenkau and A. Offenhäusser. Positively charged supported lipid bilayers as a biomimetic platform for neuronal cell culture. *Langmuir*, 28(37):13387–94, 2012.

[2] M.-L. Ainalem, N. Kristen, K. J. Edler, F. Höök, E. Sparr, and T. Nylander. DNA binding to zwitterionic model membranes. *Langmuir*, 26(7):4965–76, 2010.

[3] A. Aksimentiev and K. Schulten. Imaging alpha-hemolysin with molecular dynamics: ionic conductance, osmotic permeability, and the electrostatic potential map. *Biophys J*, 88(6):3745–61, 2005.

[4] M. R. Ali, K. H. Cheng, and J. Huang. Assess the nature of cholesterol-lipid interactions through the chemical potential of cholesterol in phosphatidylcholine bilayers. *Proc Natl Acad Sci U S A*, 104(13):5372–7, 2007.

[5] M. I. Angelova and D. S. Dimitrov. Liposome electroformation. *Faraday discussions of the Chemical Society*, 81:303–311, 1986.

[6] P. C. Anthony, C. F. Perez, C. García-García, and S. M. Block. Folding energy landscape of the thiamine pyrophosphate riboswitch aptamer. *Proc Natl Acad Sci U S A*, 109(5):1485–9, 2012.

[7] V. Arnaut, M. Langecker, and F. C. Simmel. Nanopore force spectroscopy of aptamer-ligand complexes. *Biophys J*, 105(5):1199–207, 2013.

[8] M. Ayub, S. W. Hardwick, B. F. Luisi, and H. Bayley. Nanopore-based identification of individual nucleotides for direct rna sequencing. *Nano Lett*, 13(12):6144–50, 2013.

[9] G. Baaken, M. Sondermann, C. Schlemmer, J. Rühe, and J. C. Behrends. Planar microelectrode-cavity array for high-resolution and parallel electrical recording of membrane ionic currents. *Lab Chip*, 8(6):938–44, 2008.

[10] P. Baaske, C. J. Wienken, P. Reineck, S. Duhr, and D. Braun. Optical thermophoresis for quantifying the buffer dependence of aptamer binding. *Angew. Chem., Int. Ed.*, 49(12):2238–2241, 2010.

[11] J. R. Babendure, S. R. Adams, and R. Y. Tsien. Aptamers switch on fluorescence of triphenylmethane dyes. *J Am Chem Soc*, 125(48):14716–7, 2003.

[12] G. Bainbridge, I. Gokce, and J. H. Lakey. Voltage gating is a fundamental feature of porin and toxin beta-barrel membrane channels. *FEBS Lett*, 431(3):305–8, 1998.

[13] E. Baldrich, A. Restrepo, and C. K. O'Sullivan. Aptasensor development: elucidation of critical parameters for optimal aptamer performance. *Anal. Chem.*, 76(23):7053–7063, 2004.

[14] A. Baslé, R. Iyer, and A. H. Delcour. Subconductance states in OmpF gating. *Biochim Biophys Acta*, 1664(1):100–7, 2004.

[15] A. Baslé, R. Qutub, M. Mehrazin, J. Wibbenmeyer, and A. H. Delcour. Deletions of single extracellular loops affect pH sensitivity, but not voltage dependence, of the Escherichia coli porin OmpF. *Protein Eng Des Sel*, 17(9):665–72, 2004.

[16] C. Baugh, D. Grate, and C. Wilson. 2.8 A crystal structure of the malachite green aptamer. *J Mol Biol*, 301(1):117–28, 2000.

[17] H. Bayley and P. S. Cremer. Stochastic sensors inspired by biology. *Nature*, 413(6852):226–30, 2001.

[18] P. A. Beales and T. K. Vanderlick. Partitioning of membrane-anchored DNA between coexisting lipid phases. *J Phys Chem B*, 113(42):13678–86, 2009.

[19] I. Biró, S. Pezeshki, H. Weingart, M. Winterhalter, and U. Kleinekathöfer. Comparing the temperature-dependent conductance of the two structurally similar E. coli porins OmpC and OmpF. *Biophys J*, 98(9):1830–9, 2010.

[20] A. Blicher, K. Wodzinska, M. Fidorra, M. Winterhalter, and T. Heimburg. The temperature dependence of lipid membrane permeability, its quantized nature, and the influence of anesthetics. *Biophys J*, 96(11):4581–91, 2009.

[21] M. C. Blosser, B. G. Horst, and S. L. Keller. cDICE method produces giant lipid vesicles under physiological conditions of charged lipids and ionic solutions. *Soft Matter*, 12(35):7364–7371, 2016.

[22] L. C. Bock, L. C. Griffin, J. A. Latham, E. H. Vermaas, and J. J. Toole. Selection of single-stranded-DNA molecules that bind and inhibit human thrombin. *Nature*, 355(6360):564–566, 1992.

[23] O. Braha, L. Q. Gu, L. Zhou, X. Lu, S. Cheley, and H. Bayley. Simultaneous stochastic sensing of divalent metal ions. *Nat Biotechnol*, 18(9):1005–7, 2000.

[24] D. Branton, D. W. Deamer, A. Marziali, H. Bayley, S. A. Benner, T. Butler, M. Di Ventra, S. Garaj, A. Hibbs, X. Huang, S. B. Jovanovich, P. S. Krstic, S. Lindsay, X. S. Ling, C. H. Mastrangelo, A. Meller, J. S. Oliver, Y. V. Pershin, J. M. Ramsey, R. Riehn, G. V. Soni, V. Tabard-Cossa, M. Wanunu, M. Wiggin, and J. A. Schloss. The potential and challenges of nanopore sequencing. *Nat Biotechnol*, 26(10):1146–53, 2008.

[25] A. Bunge, M. Loew, P. Pescador, A. Arbuzova, N. Brodersen, J. Kang, L. Dähne, J. Liebscher, A. Herrmann, G. Stengel, and D. Huster. Lipid membranes carrying lipophilic cholesterol-based oligonucleotides–characterization and application on layer-by-layer coated particles. *J Phys Chem B*, 113(51):16425–34, 2009.

[26] S. Burge, G. N. Parkinson, P. Hazel, A. K. Todd, and S. Neidle. Quadruplex DNA: sequence, topology and structure. *Nucleic Acids Res*, 34(19):5402–15, 2006.

[27] J. R. Burns, N. Al-Juffali, S. M. Janes, and S. Howorka. Membrane-spanning DNA nanopores with cytotoxic effect. *Angew Chem Int Ed Engl*, 53(46):12466–70, Nov 2014.

[28] J. R. Burns, K. Göpfrich, J. W. Wood, V. V. Thacker, E. Stulz, U. F. Keyser, and S. Howorka. Lipid-bilayer-spanning DNA nanopores with a bifunctional porphyrin anchor. *Angew Chem Int Ed Engl*, 52(46):12069–72, 2013.

[29] J. R. Burns, A. Seifert, N. Fertig, and S. Howorka. A biomimetic DNA-based channel for the ligand-controlled transport of charged molecular cargo across a biological membrane. *Nature nanotechnology*, 2016.

[30] J. R. Burns, E. Stulz, and S. Howorka. Self-assembled DNA nanopores that span lipid bilayers. *Nano Lett*, 13(6):2351–6, 2013.

[31] T. Z. Butler, M. Pavlenok, I. M. Derrington, M. Niederweis, and J. H. Gundlach. Single-molecule DNA detection with an engineered MspA protein nanopore. *Proc Natl Acad Sci U S A*, 105(52):20647–52, 2008.

[32] S. Carson, J. Wilson, A. Aksimentiev, and M. Wanunu. Smooth DNA transport through a narrowed pore geometry. *Biophys J*, 107(10):2381–93, 2014.

[33] C. E. Castro, F. Kilchherr, D.-N. Kim, E. L. Shiao, T. Wauer, P. Wortmann, M. Bathe, and H. Dietz. A primer to scaffolded DNA origami. *Nat Methods*, 8(3):221–9, 2011.

[34] P. Cekan, E. O. Jonsson, and S. T. Sigurdsson. Folding of the cocaine aptamer studied by EPR and fluorescence spectroscopies using the bifunctional spectroscopic probe ç. *Nucleic Acids Res.*, 37(12):3990–3995, 2009.

[35] G. M. Cherf, K. R. Lieberman, H. Rashid, C. E. Lam, K. Karplus, and M. Akeson. Automated forward and reverse ratcheting of DNA in a nanopore at 5-A precision. *Nature biotechnology*, 30(4):344–348, 2012.

[36] M. Chiba, M. Miyazaki, and S. Ishiwata. Quantitative analysis of the lamellarity of giant liposomes prepared by the inverted emulsion method. *Biophys J*, 107(2):346–54, 2014.

[37] D. E. Clapham. TRP channels as cellular sensors. *Nature*, 426(6966):517–24, 2003.

[38] J. B. Da Costa and T. Dieckmann. Entropy and Mg 2+ control ligand affinity and specificity in the malachite green binding RNA aptamer. *Molecular BioSystems*, 7(7):2156–2163, 2011.

[39] C. Dekker. Solid-state nanopores. *Nat Nanotechnol*, 2(4):209–15, 2007.

[40] A. H. Delcour, B. Martinac, J. Adler, and C. Kung. Voltage-sensitive ion channel of Escherichia coli. *J Membr Biol*, 112(3):267–75, 1989.

[41] A. A. Deniz, S. Mukhopadhyay, and E. A. Lemke. Single-molecule biophysics: at the interface of biology, physics and chemistry. *J. R. Soc. Interface*, 5(18):15–45, 2008.

[42] S. M. Douglas, H. Dietz, T. Liedl, B. Högberg, F. Graf, and W. M. Shih. Self-assembly of DNA into nanoscale three-dimensional shapes. *Nature*, 459(7245):414–8, 2009.

[43] S. M. Douglas, A. H. Marblestone, S. Teerapittayanon, A. Vazquez, G. M. Church, and W. M. Shih. Rapid prototyping of 3D DNA-origami shapes with caDNAno. *Nucleic Acids Res*, 37(15):5001–6, 2009.

[44] O. K. Dudko, G. Hummer, and A. Szabo. Intrinsic rates and activation free energies from single-molecule pulling experiments. *Phys. Rev. Lett.*, 96(10):108101, 2006.

[45] O. K. Dudko, G. Hummer, and A. Szabo. Theory, analysis, and interpretation of single-molecule force spectroscopy experiments. *Proc. Natl. Acad. Sci. U. S. A.*, 105(41):15755–15760, 2008.

[46] O. K. Dudko, J. Mathé, A. Szabo, A. Meller, and G. Hummer. Extracting kinetics from single-molecule force spectroscopy: Nanopore unzipping of DNA hairpins. *Biophys. J.*, 92(12):4188–4195, 2007.

[47] A. D. Ellington and J. W. Szostak. In vitro selection of RNA molecules that bind specific ligands. *Nature*, 346(6287):818–822, 1990.

[48] M. Faller, M. Niederweis, and G. E. Schulz. The structure of a mycobacterial outer-membrane channel. *Science*, 303(5661):1189–92, 2004.

[49] P. L. Felgner, T. R. Gadek, M. Holm, R. Roman, H. W. Chan, M. Wenz, J. P. Northrop, G. M. Ringold, and M. Danielsen. Lipofection: a highly efficient, lipid-mediated DNA-transfection procedure. *Proc Natl Acad Sci U S A*, 84(21):7413–7, 1987.

[50] L. R. Fiegland, A. D. Garst, R. T. Batey, and D. J. Nesbitt. Single-molecule studies of the lysine riboswitch reveal effector-dependent conformational dynamics of the aptamer domain. *Biochemistry*, 51(45):9223–33, 2012.

[51] U. Förster, J. E. Weigand, P. Trojanowski, B. Suess, and J. Wachtveitl. Conformational dynamics of the tetracycline-binding aptamer. *Nucleic Acids Res.*, 40(4):1807–1817, 2012.

[52] O. Francescangeli, V. Stanic, L. Gobbi, P. Bruni, M. Iacussi, G. Tosi, and S. Bernstorff. Structure of self-assembled liposome-DNA-metal complexes. *Phys Rev E Stat Nonlin Soft Matter Phys*, 67(1 Pt 1):011904, 2003.

[53] J. Geng, K. Kim, J. Zhang, A. Escalada, R. Tunuguntla, L. R. Comolli, F. I. Allen, A. V. Shnyrova, K. R. Cho, D. Munoz, Y. M. Wang, C. P. Grigoropoulos, C. M. Ajo-Franklin, V. A. Frolov, and A. Noy. Stochastic transport through carbon nanotubes in lipid bilayers and live cell membranes. *Nature*, 514(7524):612–5, 2014.

[54] U. Gerland, R. Bundschuh, and T. Hwa. Force-induced denaturation of RNA. *Biophys J*, 81(3):1324–32, 2001.

[55] G. Gokulrangan, J. R. Unruh, D. F. Holub, B. Ingram, C. K. Johnson, and G. S. Wilson. DNA aptamer-based bioanalysis of IgE by fluorescence anisotropy. *Anal. Chem.*, 77(7):1963–70, 2005.

[56] K. Göpfrich, C.-Y. Li, M. Ricci, S. P. Bhamidimarri, J. Yoo, B. Gyenes, A. Ohmann, M. Winterhalter, A. Aksimentiev, and U. F. Keyser. Large-conductance transmembrane porin made from DNA origami. *ACS Nano*, 10(9):8207–14, 2016.

[57] W. J. Greenleaf, K. L. Frieda, D. A. N. Foster, M. T. Woodside, and S. M. Block. Direct observation of hierarchical folding in single riboswitch aptamers. *Science*, 319(5863):630–633, 2008.

[58] S. Gromelski and G. Brezesinski. DNA condensation and interaction with zwitterionic phospholipids mediated by divalent cations. *Langmuir*, 22(14):6293–301, 2006.

[59] L. Q. Gu, O. Braha, S. Conlan, S. Cheley, and H. Bayley. Stochastic sensing of organic analytes by a pore-forming protein containing a molecular adapter. *Nature*, 398(6729):686–90, 1999.

[60] M. Hadorn and P. Eggenberger Hotz. DNA-mediated self-assembly of artificial vesicles. *PLoS One*, 5(3):e9886, 2010.

[61] A. R. Hall, A. Scott, D. Rotem, K. K. Mehta, H. Bayley, and C. Dekker. Hybrid pore formation by directed insertion of alpha-haemolysin into solid-state nanopores. *Nat Nanotechnol*, 5(12):874–7, 2010.

[62] A. Haller, R. B. Altman, M. F. Soulière, S. C. Blanchard, and R. Micura. Folding and ligand recognition of the TPP riboswitch aptamer at single-molecule resolution. *Proc. Natl. Acad. Sci. U. S. A.*, 110(11):4188–93, 2013.

[63] F. Haque, J. Lunn, H. Fang, D. Smithrud, and P. Guo. Real-time sensing and discrimination of single chemicals using the channel of phi29 DNA packaging nanomotor. *ACS Nano*, 6(4):3251–61, 2012.

[64] B. He, A. Kukarin, D. Temiakov, S. T. Chin-Bow, D. L. Lyakhov, M. Rong, R. K. Durbin, and W. T. McAllister. Characterization of an unusual, sequence-specific termination signal for T7 RNA polymerase. *Journal of Biological Chemistry*, 273(30):18802–18811, 1998.

[65] T. Heimburg. *Thermal biophysics of membranes*. John Wiley & Sons, 2008.

[66] M. Hennig, M. Wolff, J. Neumann, A. Wixforth, M. F. Schneider, and J. O. Rädler. DNA concentration modulation on supported lipid bilayers switched by surface acoustic waves. *Langmuir*, 27(24):14721–5, 2011.

[67] H. D. Herce and A. E. Garcia. Molecular dynamics simulations suggest a mechanism for translocation of the HIV-1 TAT peptide across lipid membranes. *Proc Natl Acad Sci U S A*, 104(52):20805–10, 2007.

[68] T. Hianik, V. Ostatná, M. Sonlajtnerova, and I. Grman. Influence of ionic strength, pH and aptamer configuration for binding affinity to thrombin. *Bioelectrochemistry*, 70(1):127–133, 2007.

[69] B. Hille. Ionic channels: molecular pores of excitable membranes. *Harvey Lect*, 82:47–69, 1986.

[70] J. M. Holopainen, A. J. Metso, J.-P. Mattila, A. Jutila, and P. K. J. Kinnunen. Evidence for the lack of a specific interaction between cholesterol and sphingomyelin. *Biophys J*, 86(3):1510–20, 2004.

[71] B. Hornblower, A. Coombs, R. D. Whitaker, A. Kolomeisky, S. J. Picone, A. Meller, and M. Akeson. Single-molecule analysis of DNA-protein complexes using nanopores. *Nat. Methods*, 4(4):315–317, 2007.

[72] S. Howorka and Z. Siwy. Nanopore analytics: sensing of single molecules. *Chem Soc Rev*, 38(8):2360–84, 2009.

[73] J. Hu and C. J. Easley. A simple and rapid approach for measurement of dissociation constants of DNA aptamers against proteins and small molecules via automated microchip ele ... - analyst (rsc publishing) doi:10.1039/c0an00842g. *Analyst*, 2011.

[74] Y.-F. Huang, D. Shangguan, H. Liu, J. A. Phillips, X. Zhang, Y. Chen, and W. Tan. Molecular assembly of an aptamer-drug conjugate for targeted drug delivery to tumor cells. *Chembiochem*, 10(5):862–8, 2009.

[75] M. J. Hubley, B. R. Locke, and T. S. Moerland. The effects of temperature, pH, and magnesium on the diffusion coefficient of ATP in solutions of physiological ionic strength. *Biochim. Biophys. Acta*, 1291(2):115–21, 1996.

[76] J. Huff, M. Pavlenok, S. Sukumaran, and M. Niederweis. Functions of the periplasmic loop of the porin MspA from Mycobacterium smegmatis. *J Biol Chem*, 284(15):10223–31, 2009.

[77] D. E. Huizenga and J. W. Szostak. A DNA aptamer that binds adenosine and ATP. *Biochemistry*, 34(2):656–665, 1995.

[78] M. K. Jain and D. Zakim. The spontaneous incorporation of proteins into preformed bilayers. *Biochim Biophys Acta*, 906(1):33–68, 1987.

[79] S. D. Jhaveri, R. Kirby, R. Conrad, E. J. Maglott, M. Bowser, R. T. Kennedy, G. Glick, and A. D. Ellington. Designed signaling aptamers that transduce molecular recognition to changes in fluorescence intensity. *J. Am. Chem. Soc.*, 122(11):2469–2473, Mar. 2000.

[80] F. M. Jucker, R. M. Phillips, S. A. McCallum, and A. Pardi. Role of a heterogeneous free state in the formation of a specific RNA-theophylline complex. *Biochemistry*, 42(9):2560–2567, Mar. 2003.

[81] J. J. Kasianowicz, E. Brandin, D. Branton, and D. W. Deamer. Characterization of individual polynucleotide molecules using a membrane channel. *Proc Natl Acad Sci U S A*, 93(24):13770–3, 1996.

[82] A. Kato, A. Tsuji, M. Yanagisawa, D. Saeki, K. Juni, Y. Morimoto, and K. Yoshikawa. Phase separation on a phospholipid membrane inducing a characteristic localization of DNA accompanied by its structural transition. *The Journal of Physical Chemistry Letters*, 23(1):3391–3395, 2010.

[83] A. D. Keefe, S. Pai, and A. Ellington. Aptamers as therapeutics. *Nat. Rev. Drug Discovery*, 9(7):537–550, 2010.

[84] S. L. Keller, S. M. Bezrukov, S. M. Gruner, M. W. Tate, I. Vodyanoy, and V. A. Parsegian. Probability of alamethicin conductance states varies with nonlamellar tendency of bilayer phospholipids. *Biophys J*, 65(1):23–7, 1993.

[85] A. Kessel, N. Ben-Tal, and S. May. Interactions of cholesterol with lipid bilayers: the preferred configuration and fluctuations. *Biophys J*, 81(2):643–58, 2001.

[86] S. Khalid, P. J. Bond, J. Holyoake, R. W. Hawtin, and M. S. P. Sansom. DNA and lipid bilayers: self-assembly and insertion. *J R Soc Interface*, 5 Suppl 3:S241–50, 2008.

[87] D. Koirala, S. Dhakal, B. Ashbridge, Y. Sannohe, R. Rodriguez, H. Sugiyama, S. Balasubramanian, and H. Mao. A single-molecule platform for investigation of interactions between G-quadruplexes and small-molecule ligands. *Nat. Chem.*, 3(10):782–787, 2011.

[88] Y. E. Korchev, G. M. Alder, A. Bakhramov, C. L. Bashford, B. S. Joomun, E. V. Sviderskaya, P. N. Usherwood, and C. A. Pasternak. Staphylococcus aureus alpha-toxin-induced pores: channel-like behavior in lipid bilayers and patch clamped cells. *J Membr Biol*, 143(2):143–51, 1995.

[89] O. V. Krasilnikov, V. I. Ternovsky, P. G. Merzliak, L. T. Zachidova, and K. D. Hungerer. Effects of monoclonal antibodies on alpha-staphylotoxin action against erythrocytes and model phospholipid membranes. *Biochim Biophys Acta*, 1182(1):94–100, 1993.

[90] M. Kreir, C. Farre, M. Beckler, M. George, and N. Fertig. Rapid screening of membrane protein activity: electrophysiological analysis of OmpF reconstituted in proteoliposomes. *Lab Chip*, 8(4):587–95, 2008.

[91] S. Krishnan, D. Ziegler, V. Arnaut, T. G. Martin, K. Kapsner, K. Henneberg, A. R. Bausch, H. Dietz, and F. C. Simmel. Molecular transport through large-diameter DNA nanopores. *Nat Commun*, 7:12787, 2016.

[92] N. Kumar and S. Maiti. Quadruplex to Watson-Crick duplex transition of the thrombin binding aptamer: a fluorescence resonance energy transfer study. *Biochem. Biophys. Res. Commun.*, 319(3):759–67, 2004.

[93] A. Kurz, A. Bunge, A.-K. Windeck, M. Rost, W. Flasche, A. Arbuzova, D. Strohbach, S. Müller, J. Liebscher, D. Huster, and A. Herrmann. Lipid-anchored oligonucleotides for stable double-helix formation in distinct membrane domains. *Angew Chem Int Ed Engl*, 45(27):4440–4, 2006.

[94] M. Langecker, V. Arnaut, J. List, and F. C. Simmel. DNA nanostructures interacting with lipid bilayer membranes. *Acc Chem Res*, 47(6):1807–15, 2014.

[95] M. Langecker, V. Arnaut, T. G. Martin, J. List, S. Renner, M. Mayer, H. Dietz, and F. C. Simmel. Synthetic lipid membrane channels formed by designed DNA nanostructures. *Science*, 338(6109):932–6, 2012.

[96] H. A. Lester, M. I. Dibas, D. S. Dahan, J. F. Leite, and D. A. Dougherty. Cys-loop receptors: new twists and turns. *Trends Neurosci*, 27(6):329–36, 2004.

[97] C.-Y. Li, E. A. Hemmig, J. Kong, J. Yoo, S. Hernández-Ainsa, U. F. Keyser, and A. Aksimentiev. Ionic conductivity, structural deformation, and programmable anisotropy of dna origami in electric field. *ACS Nano*, 9(2):1420–33, Feb 2015.

[98] C. H. Lin and D. J. Patel. Structural basis of DNA folding and recognition in an AMP-DNA aptamer complex: distinct architectures but common recognition motifs for DNA and RNA aptamers complexed to AMP. *Chem. Biol.*, 4(11):817–832, 1997.

[99] M. Loew, R. Springer, S. Scolari, F. Altenbrunn, O. Seitz, J. Liebscher, D. Huster, A. Herrmann, and A. Arbuzova. Lipid domain specific recruitment of lipophilic nucleic acids: a key for switchable functionalization of membranes. *J Am Chem Soc*, 132(45):16066–72, 2010.

[100] D. Lu and D. G. Rhodes. Binding of phosphorothioate oligonucleotides to zwitterionic liposomes. *Biochim Biophys Acta*, 1563(1-2):45–52, 2002.

[101] S. Lynch, H. Baker, S. G. Byker, D. Zhou, and K. Sinniah. Single molecule force spectroscopy on G-quadruplex DNA. *Chemistry*, 15(33):8113–8116, 2009.

[102] S. Majd, E. C. Yusko, Y. N. Billeh, M. X. Macrae, J. Yang, and M. Mayer. Applications of biological pores in nanomedicine, sensing, and nanoelectronics. *Curr Opin Biotechnol*, 21(4):439–76, 2010.

[103] M. Malghani and J. Yang. Stable binding of DNA to zwitterionic lipid bilayers in aqueous solutions. *The Journal of Physical Chemistry B*, 102(44):8930–8933, 1998.

[104] E. A. Manrao, I. M. Derrington, A. H. Laszlo, K. W. Langford, M. K. Hopper, N. Gillgren, M. Pavlenok, M. Niederweis, and J. H. Gundlach. Reading DNA at single-nucleotide resolution with a mutant MspA nanopore and phi29 DNA polymerase. *Nat Biotechnol*, 30(4):349–53, 2012.

[105] S. J. Marrink, A. H. de Vries, and D. P. Tieleman. Lipids on the move: simulations of membrane pores, domains, stalks and curves. *Biochim Biophys Acta*, 1788(1):149–68, 2009.

[106] D. Marsh. Lateral pressure profile, spontaneous curvature frustration, and the incorporation and conformation of proteins in membranes. *Biophys J*, 93(11):3884–99, 2007.

[107] J. Mathé, H. Visram, V. Viasnoff, Y. Rabin, and A. Meller. Nanopore unzipping of individual DNA hairpin molecules. *Biophys. J.*, 87(5):3205–3212, 2004.

[108] T. J. McIntosh and S. A. Simon. Roles of bilayer material properties in function and distribution of membrane proteins. *Annu Rev Biophys Biomol Struct*, 35:177–98, 2006.

[109] J. J. McManus, J. O. Rädler, , and K. A. Dawson. Does calcium turn a zwitterionic lipid cationic? *J. Phys. Chem.*, 2003.

[110] A. Meller and D. Branton. Single molecule measurements of DNA transport through a nanopore. *Electrophoresis*, 23(16):2583–91, 2002.

[111] L. D. Mosgaard and T. Heimburg. Lipid ion channels and the role of proteins. *Acc Chem Res*, 46(12):2966–76, Dec 2013.

[112] L. Movileanu, S. Howorka, O. Braha, and H. Bayley. Detecting protein analytes that modulate transmembrane movement of a polymer chain within a single protein pore. *Nat Biotechnol*, 18(10):1091–5, 2000.

[113] J. Muzard, M. Martinho, J. Mathé, U. Bockelmann, and V. Viasnoff. DNA translocation and unzipping through a nanopore: some geometrical effects. *Biophys J*, 98(10):2170–8, 2010.

[114] I. Nakamura, A.-C. Shi, R. Nutiu, J. Yu, and Y. Li. Kinetics of signaling-DNA-aptamer-ATP binding. *Phys. Rev. E*, 79(3):031906, Mar. 2009.

[115] E. M. Nestorovich, T. K. Rostovtseva, and S. M. Bezrukov. Residue ionization and ion transport through OmpF channels. *Biophys J*, 85(6):3718–29, 2003.

[116] K. Neupane, H. Yu, D. A. N. Foster, F. Wang, and M. T. Woodside. Single-molecule force spectroscopy of the add adenine riboswitch relates folding to regulatory mechanism. *Nucleic Acids Res.*, 39(17):7677–87, 2011.

[117] J. Noeske, J. Buck, B. Fürtig, H. R. Nasiri, H. Schwalbe, and J. Wöhnert. Interplay of 'induced fit' and preorganization in the ligand induced folding of the aptamer domain of the guanine binding riboswitch. *Nucleic Acids Res.*, 35(2):572–583, 2007.

[118] S. Nonin-Lecomte, C. H. Lin, and D. J. Patel. Additional hydrogen bonds and base-pair kinetics in the symmetrical AMP-DNA aptamer complex. *Biophys. J.*, 81(6):3422–3431, 2001.

[119] R. Nutiu and Y. Li. Structure-switching signaling aptamers. *J. Am. Chem. Soc.*, 2003.

[120] R. Nutiu and Y. Li. Structure-switching signaling aptamers: transducing molecular recognition into fluorescence signaling. *Chemistry*, 10(8):1868–76, 2004.

[121] K. Padmanabhan and A. Tulinsky. An ambiguous structure of a DNA 15-mer thrombin complex. *Acta Crystallogr., Sect. D: Biol. Crystallogr.*, 52:272–282, 1996.

[122] D. Papahadjopoulos, K. Jacobson, S. Nir, and T. Isac. Phase transitions in phospholipid vesicles. fluorescence polarization and permeability measurements concerning the effect of temperature and cholesterol. *Biochim Biophys Acta*, 311(3):330–48, 1973.

[123] R. G. Parton and J. F. Hancock. Lipid rafts and plasma membrane microorganization: insights from Ras. *Trends Cell Biol*, 14(3):141–7, 2004.

[124] I. Pfeiffer and F. Höök. Bivalent cholesterol-based coupling of oligonucletides to lipid membrane assemblies. *J Am Chem Soc*, 126(33):10224–5, 2004.

[125] S. J. Plowman, C. Muncke, R. G. Parton, and J. F. Hancock. H-ras, K-ras, and inner plasma membrane raft proteins operate in nanoclusters with differential dependence on the actin cytoskeleton. *Proc Natl Acad Sci U S A*, 102(43):15500–5, 2005.

[126] E. Pozharski and R. C. MacDonald. Thermodynamics of cationic lipid-DNA complex formation as studied by isothermal titration calorimetry. *Biophys J*, 83(1):556–65, 2002.

[127] K. Pratt, W. Koch, Y. Wu, and P. Berezansky. Molality-based primary standards of electrolytic conductivity (iupac technical report). *Pure and applied chemistry*, 73(11):1783–1793, 2001.

[128] M. Raible, M. Evstigneev, P. Reimann, F. W. Bartels, and R. Ros. Theoretical analysis of dynamic force spectroscopy experiments on ligand-receptor complexes. *J. Biotechnol.*, 112(1-2):13–23, 2004.

[129] S. Renner, A. Bessonov, U. Gerland, and F. C. Simmel. Sequence-dependent unfolding kinetics of DNA hairpins studied by nanopore force spectroscopy. *J. Phys.: Condens. Matter*, 22(45):454119, Nov. 2010.

[130] S. Renner, A. Bessonov, and F. C. Simmel. Voltage-controlled insertion of single α-hemolysin and Mycobacterium smegmatis nanopores into lipid bilayer membranes. *Applied Physics Letters*, 98(8):083701, 2011.

[131] S. Renner, S. Geltinger, and F. C. Simmel. Nanopore translocation and force spectroscopy experiments in microemulsion droplets. *Small*, 6(2):190–194, 2010.

[132] M. D. Resh. Palmitoylation of ligands, receptors, and intracellular signaling molecules. *Sci STKE*, 2006(359):re14, 2006.

[133] D. Rotem, L. Jayasinghe, M. Salichou, and H. Bayley. Protein detection by nanopores equipped with aptamers. *J. Am. Chem. Soc.*, 134(5):2781–7, 2012.

[134] B. Sakmann. *Single-channel recording*. Springer Science & Business Media, 2013.

[135] A. F. Sauer-Budge, J. A. Nyamwanda, D. K. Lubensky, and D. Branton. Unzipping kinetics of double-stranded DNA in a nanopore. *Phys Rev Lett*, 90(23):238101, 2003.

[136] S. Schink, S. Renner, K. Alim, V. Arnaut, F. C. Simmel, and U. Gerland. Quantitative analysis of the nanopore translocation dynamics of simple structured polynucleotides. *Biophys J*, 102(1):85–95, 2012.

[137] E. K. Schmitt, M. Vrouenraets, and C. Steinem. Channel activity of OmpF monitored in nano-BLMs. *Biophys J*, 91(6):2163–71, 2006.

[138] A. Seifert, K. Göpfrich, J. R. Burns, N. Fertig, U. F. Keyser, and S. Howorka. Bilayer-spanning DNA nanopores with voltage-switching between open and closed state. *ACS Nano*, 9(2):1117–26, 2015.

[139] N. S. Selden, M. E. Todhunter, N. Y. Jee, J. S. Liu, K. E. Broaders, and Z. J. Gartner. Chemically programmed cell adhesion with membrane-anchored oligonucleotides. *J Am Chem Soc*, 134(2):765–8, 2012.

[140] J. W. Shim and L.-Q. Gu. Encapsulating a single G-quadruplex aptamer in a protein nanocavity. *J. Phys. Chem. B*, 112(28):8354–8360, 2008.

[141] H. Shogomori, A. T. Hammond, A. G. Ostermeyer-Fay, D. J. Barr, G. W. Feigenson, E. London, and D. A. Brown. Palmitoylation and intracellular domain interactions both contribute to raft targeting of linker for activation of T cells. *J Biol Chem*, 280(19):18931–42, 2005.

[142] R. M. M. Smeets, S. W. Kowalczyk, A. R. Hall, N. H. Dekker, and C. Dekker. Translocation of RecA-coated double-stranded DNA through solid-state nanopores. *Nano Lett.*, 9(9):3089–96, 2009.

[143] A. M. Smith, R. Abu-Shumays, M. Akeson, and D. L. Bernick. Capture, unfolding, and detection of individual tRNA molecules using a nanopore device. *Front Bioeng Biotechnol*, 3:91, 2015.

[144] S. Song, L. Wang, J. Li, C. Fan, and J. Zhao. Aptamer-based biosensors. *TrAC, Trends Anal. Chem.*, 27(2):108–117, Feb. 2008.

[145] S. Sukharev and A. Anishkin. Mechanosensitive channels: what can we learn from 'simple' model systems? *Trends Neurosci*, 27(6):345–51, 2004.

[146] V. Tabard-Cossa, M. Wiggin, D. Trivedi, N. N. Jetha, J. R. Dwyer, and A. Marziali. Single-molecule bonds characterized by solid-state nanopore force spectroscopy. *ACS Nano*, 3(10):3009–14, 2009.

[147] S. Tombelli, M. Minunni, E. Luzi, and M. Mascini. Aptamer-based biosensors for the detection of HIV-1 Tat protein. *Bioelectrochemistry*, 67(2):135–141, Oct. 2005.

[148] S. G. Trevino, N. Zhang, M. P. Elenko, A. Lupták, and J. W. Szostak. Evolution of functional nucleic acids in the presence of nonheritable backbone heterogeneity. *Proc. Natl. Acad. Sci. U. S. A.*, 108(33):13492–13497, Aug. 2011.

[149] B. J. Tucker and R. R. Breaker. Riboswitches as versatile gene control elements. *Curr. Opin. Struct. Biol.*, 15:342, 2005.

[150] C. Tuerk and L. Gold. Systematic evolution of ligands by exponential enrichment: RNA ligands to bacteriophage T4 DNA-polymerase. *Science*, 249:505, 1990.

[151] S. L. Veatch and S. L. Keller. Separation of liquid phases in giant vesicles of ternary mixtures of phospholipids and cholesterol. *Biophys J*, 85(5):3074–83, 2003.

[152] S. L. Veatch and S. L. Keller. Miscibility phase diagrams of giant vesicles containing sphingomyelin. *Phys Rev Lett*, 94(14):148101, 2005.

[153] W. Vercoutere, S. Winters-Hilt, H. Olsen, D. Deamer, D. Haussler, and M. Akeson. Rapid discrimination among individual DNA hairpin molecules at single-nucleotide resolution using an ion channel. *Nat Biotechnol*, 19(3):248–52, 2001.

[154] J. C. von der Maarel. *Introduction to biopolymer physics*. World Scientific, 2007.

[155] Y. Wang and B. Liu. ATP detection using a label-free DNA aptamer and a cationic tetrahedralfluorene. *Analyst*, 133(11):1593–1598, Nov. 2008.

[156] Y. Wang, Y. Wang, and B. Liu. Fluorescent detection of ATP based on signaling DNA aptamer attached silica nanoparticles. *Nanotechnology*, 19(41):415605, 2008.

[157] Y. Wang, D. Zheng, Q. Tan, M. X. Wang, and L.-Q. Gu. Nanopore-based detection of circulating microRNAs in lung cancer patients. *Nat Nanotechnol*, 6(10):668–74, 2011.

[158] Z. Wang, T. Wilkop, D. Xu, Y. Dong, G. Ma, and Q. Cheng. Surface plasmon resonance imaging for affinity analysis of aptamer-protein interactions with PDMS microfluidic chips. *Anal. Bioanal. Chem.*, 389(3):819–825, Oct. 2007.

[159] M. Wanunu, S. Bhattacharya, Y. Xie, Y. Tor, A. Aksimentiev, and M. Drndic. Nanopore analysis of individual RNA/antibiotic complexes. *ACS Nano*, 5(12):9345–53, 2011.

[160] M. Wanunu, J. Sutin, and A. Meller. DNA profiling using solid-state nanopores: detection of DNA-binding molecules. *Nano Lett.*, 9(10):3498–502, 2009.

[161] R. Wei, V. Gatterdam, R. Wieneke, R. Tampé, and U. Rant. Stochastic sensing of proteins with receptor-modified solid-state nanopores. *Nat Nanotechnol*, 7(4):257–63, 2012.

[162] R. Wei, T. G. Martin, U. Rant, and H. Dietz. DNA origami gatekeepers for solid-state nanopores. *Angew Chem Int Ed Engl*, 51(20):4864–7, 2012.

[163] D. Wendell, P. Jing, J. Geng, V. Subramaniam, T. J. Lee, C. Montemagno, and P. Guo. Translocation of double-stranded DNA through membrane-adapted phi29 motor protein nanopores. *Nat Nanotechnol*, 4(11):765–72, 2009.

[164] J. Wohlert, W. K. den Otter, O. Edholm, and W. J. Briels. Free energy of a transmembrane pore calculated from atomistic molecular dynamics simulations. *J Chem Phys*, 124(15):154905, 2006.

[165] S. Yesylevskyy, S.-J. Marrink, and A. E. Mark. Alternative mechanisms for the interaction of the cell-penetrating peptides penetratin and the TAT peptide with lipid bilayers. *Biophys J*, 97(1):40–9, 2009.

[166] Y.-L. Ying, H.-Y. Wang, T. C. Sutherland, and Y.-T. Long. Monitoring of an ATP -binding aptamer and its conformational changes using an alpha-hemolysin nanopore. *Small*, 7(1):87–94, 2011.

[167] J. Yoo and A. Aksimentiev. In situ structure and dynamics of dna origami determined through molecular dynamics simulations. *Proc Natl Acad Sci U S A*, 110(50):20099–104, Dec 2013.

[168] J. Yoo and A. Aksimentiev. Molecular dynamics of membrane-spanning dna channels: Conductance mechanism, electro-osmotic transport, and mechanical gating. *J Phys Chem Lett*, 6(23):4680–7, Dec 2015.

[169] E. C. Yusko, J. M. Johnson, S. Majd, P. Prangkio, R. C. Rollings, J. Li, J. Yang, and M. Mayer. Controlling protein translocation through nanopores with bio-inspired fluid walls. *Nat Nanotechnol*, 6(4):253–60, 2011.

[170] X.-Q. Zhao, J. Wu, J.-H. Liang, J.-W. Yan, Z. Zhu, C. J. Yang, and B.-W. Mao. Single-molecule force spectroscopic studies on intra- and intermolecular interactions of G-quadruplex aptamer with target Shp2 protein. *J. Phys. Chem. B*, 116(37):11397–11404, 2012.

[171] B. S. Zhorov and D. B. Tikhonov. Potassium, sodium, calcium and glutamate-gated channels: pore architecture and ligand action. *J Neurochem*, 88(4):782–99, 2004.

[172] M. Zuker. Mfold web server for nucleic acid folding and hybridization prediction. *Nucleic Acids Res.*, 31(13):3406–3415, 2003.

Acknowledgments

First of all, I want to thank Friedrich Simmel, my supervisor, for giving me the opportunity to do my PhD in his group. I am grateful for the freedom that you gave me to pursue various projects and for your support during these past years.
All E14 group members, specially Stephan Renner who helped me starting in the lab. Also I want to thank Swati Krishnan, Martin Langecker, Jonathan List and Daniela Ziegler for the great work together. Especially I want to acknowledge Swati Krishnan and Daniela Ziegler who helped me with a lot of things. Korbinian Kapsner for helping me with data analysis and Maximilian Weitz for his support in the RNA project.
Additionally I would like to thanks the Dietz group, especially Thomas Martin for the fruitful collaboration on the DNA origami channel project.
For all of their technical help, I want to thank Helene Budjarek and Andrea Mückl, Nanion and IonEra. Erika Bischofs and Susanne Kinzel for helping me with all the bureaucracy.
TUM GS, BMBF, SFB 863 and ERC for their financial support.
My husband for all his support in my PhD time, my daughter for here morning smile, the best alarm clock. When Daria heard the first time that I am going to be a doctor, she opened here month, thinking that I am a dentist Doctor (she was 2 years and 4 months). "Voi m-ati motivat sa merg mai departe, si numai datorita voua am ajuns aici".
I want to thank my family and my parents for support and belief in me. "Este extraordinar sa stii ca sunteti intotdeauna alaturi si oricand ma pot baza pe voi".